THE UNIVERSITY OF CALGARY

Micromechanically-Based Random Field Characterization of Structural Material Properties

by

Luc Huyse

A DISSERTATION
SUBMITTED TO THE FACULTY OF GRADUATE STUDIES
IN PARTIAL FULFILLMENT OF THE REQUIREMENTS FOR THE
DEGREE OF DOCTOR OF PHILOSOPHY

DEPARTMENT OF CIVIL ENGINEERING

CALGARY, ALBERTA

November, 1999

Abstract

In this dissertation, a framework is developed to obtain the random field characteristics of the elastic properties of materials, which are consistent with an assumed microstructure. A detailed overview of existing micromechanical models is given. The progressive failure of elastic-brittle materials, subject to axial stresses only, is studied using stochastic parallel-bar models.

A stochastic homogenization theory of linear elastic microstructures is developed. Based on existing research regarding deformation-based homogenization, a new technique, based on a strain energy equivalency and a constant stress assumption in the material, is introduced. An improved modeling of the geometric boundary conditions is suggested. Based on locally averaged random field theory, a novel approach to modeling the variability of linear elastic materials, which is consistent with the microstructure of the material, is developed. This results in micromechanically consistent values for correlation lengths in the constitutive random fields as well as for cross-correlations between the different material properties. This improved random field material modeling can readily be used in a stochastic FE analysis.

Applications illustrate the significance of the more consistent random field modeling for structural reliability applications. It is shown how isotropy of materials is achieved in a mean sense only. An accurate estimation of the correlation between the elastic properties has important ramifications on the variance of maximum stresses, strains and deformations. Several examples illustrate this. The homogenization framework is applied to a variety of microstructures and some guidelines regarding the selection of an appropriate micromodel are provided.

Acknowledgements

This research was supported by NSERC (operating grant to Dr. Marc A. Maes), the Department of Civil Engineering, the University of Calgary (Conference Travel Grant), and the Mobil Foundation. Their support is gratefully acknowledged.

I am particularly indebted to my supervisor, Dr. Marc A. Maes, for his continuous motivation and encouragement as well as constructive criticism throughout this study. I also thank the members of the jury for their careful review of this manuscript.

Last, I would like to take this opportunity to thank all my friends, both here and in Belgium, who have helped me to make the most out of my stay in Canada. Thank you for all your thoughts and discussions on all sorts of topics. We cannot learn if we do not challenge our boundaries. To all, thank you for expanding my horizons and enriching my life.

Table of Contents

Approval Page ii

Abstract iii

Acknowledgements iv

Table of Contents v

List of Tables ix

List of Figures x

List of Abbreviations xiv

List of Symbols xv

1 Introduction 1
- 1.1 Motivation . . . 1
- 1.2 Blending Discrete and Continuum Models . . . 3
- 1.3 General Approach and Objectives . . . 8
- 1.4 Notations and Definitions . . . 9
- 1.5 Outline . . . 12

2 Micro-Mechanical Modeling of Materials 14
- 2.1 Introduction . . . 14
- 2.2 Constitutive Modeling . . . 15
  - 2.2.1 Effects of the Microstructure . . . 15
  - 2.2.2 Classification of Constitutive Models . . . 18
- 2.3 One-Dimensional Models . . . 20
  - 2.3.1 Introduction . . . 20
  - 2.3.2 Micro-Constitutive Models . . . 20
  - 2.3.3 Damage Variable . . . 25
  - 2.3.4 Randomness . . . 25
  - 2.3.5 Load Sharing Rules . . . 29
  - 2.3.6 Strength Probability Distribution of a Single Bar . . . 30
  - 2.3.7 Conclusions . . . 32
- 2.4 Multi-Dimensional Models with Regular Geometry . . . 32
  - 2.4.1 Introduction . . . 32

2.4.2 Topological Characteristics 35
2.4.3 Anisotropy 38
2.4.4 Consistency of Discrete Models 39
2.4.5 Conclusions 41
2.5 Multi-Dimensional Models with Random Geometry 42
2.5.1 Introduction 42
2.5.2 Representation of the Contacts 42
2.5.3 Representation of the Solid Constituents 44
2.5.4 Detection and Revision of the Contacts 44
2.5.5 Crystal Topology 45
2.5.6 Granular and Other Topologies 51
2.5.7 Lattice Models with Random Geometry 54
2.6 Modified Continuum Models 59
2.6.1 Introduction 59
2.6.2 Material Heterogeneity 59
2.6.3 Response Variability 60
2.7 Summary 62

3 Parallel Bar Model for Linear Elastic-Brittle Materials Subject to Uniaxial Loads **65**
3.1 Introduction 65
3.2 Model Description 66
3.2.1 General 66
3.2.2 Damage Accumulation 67
3.3 Axial Loading 68
3.3.1 Relationship Between Micro and Macro Stiffness Properties . . 68
3.3.2 Load-Displacement Curve 69
3.3.3 Damage Accumulation 75
3.3.4 Tensile Strength of Parallel Bar System 76
3.3.5 Influence of Correlation between Failure Strains 79
3.4 Pure Bending 82
3.4.1 Deterministic Continuum Model 82
3.4.2 Discrete Spring Model 84
3.4.3 Relationship Between Micro and Macro Properties 86
3.4.4 Damage Accumulation 87
3.4.5 Bounds on Variability: Two Limiting Auto-Correlation Functions 89
3.5 Summary 93

4 Stochastic Homogenization **95**
4.1 Introduction . . . 95
4.2 Overview of Stochastic Homogenization . . . 96
4.3 Equivalence Between Continua and Discrete Models . . . 96
4.4 Microstructures with Regular Geometry . . . 101
4.4.1 Introduction . . . 101
4.4.2 Homogenization of Regular Lattice Structures . . . 101
4.4.3 Modeling of Link Stiffness . . . 106
4.4.4 Limitations of Regular Geometries . . . 107
4.5 Homogenization of Random Micro-Structures . . . 108
4.5.1 Introduction . . . 108
4.5.2 Displacement-Based Homogenization Techniques . . . 109
4.5.3 Force-Based Homogenization Techniques . . . 114
4.6 Estimation of the Equivalent Macro-Random Fields . . . 119
4.6.1 Introduction . . . 119
4.6.2 Locally Averaged Random Fields . . . 119
4.6.3 Application to Micromechanical Model . . . 124
4.7 Modeling Window Boundaries . . . 126
4.8 Summary . . . 137

5 Consistent Macro Random Fields in Structural Analysis **140**
5.1 Introduction . . . 140
5.2 Features of Consistent Macro Random Fields . . . 141
5.2.1 Uniform Poisson-Delaunay Microstructure . . . 141
5.2.2 Orthotropic Poisson-Delaunay Microstructure . . . 149
5.3 Significance for Structural Analysis . . . 154
5.3.1 Objective and Definitions . . . 154
5.3.2 Element Subject To Constant Strain . . . 155
5.3.3 SFEM Analysis of Square Disk With Hole . . . 157
5.4 Selection of Micro-Mechanical Model Parameters . . . 160
5.4.1 Introduction . . . 160
5.4.2 Micro-Link Stiffness . . . 161
5.4.3 Microgeometry . . . 163
5.5 Comparison of Homogenization Techniques . . . 169
5.6 Summary . . . 171

6 Conclusions and Recommendations **173**
6.1 Summary . . . 173
6.2 Recommendations for Future Research . . . 177

Bibliography **181**

List of Tables

1.1 Orders of magnitude of Representative Volume Elements (based on Lemaitre and Chaboche, 1985) 6
1.2 Hierarchy of structural scales defining the mechanical response of concrete [Krajcinovic and Fanella, 1986] 6

2.1 Correlation between energy and Young's modulus for various models [Breysse et al., 1994] 40
2.2 Some characteristics of the Voronoi-tessellation. λ is the density of the nodes $[m^{-2}]$ 48
2.3 Classification of lattice models 63
2.4 Classification of particle models 63

3.1 Impact of COV of failure strain on system strength, damage level and critical strain for a lognormal distribution of the failure strain ε_{max} $(n = 10)$ 80
3.2 Impact of COV of failure strain on system strength, damage level and critical strain for a Weibull distribution of the failure strain ε_{max} $(n = 10)$ 80

4.1 Estimated correlations between the number of nodes in boundary strip and the total reaction force along an edge (standard error less than 0.02) 134

5.1 Comparison of summary statistics of elastic moduli $(\lambda = 0.01, K = 10, A = 100 \times 100)$ 168

List of Figures

1.1 The principle of mesomechanics [Haritos et al., 1988] 6

2.1 General approach for modeling of the uncertainty of the macroscopic structural behavior of materials 17
2.2 Possible microstructure of an RVE at a point in a macroscopic continuum [Nemat-Masser and Hori, 1993] 17
2.3 Force-displacement diagrams for re-loading in the case of plasticity and damage. 21
2.4 Parallel bar model and elastic-brittle micro-constitutive relation . . . 21
2.5 Parallel system of Jenkins elements and micro-constitutive relation . . 24
2.6 Series-parallel system used by Fanella and Krajcinovic (1986) to describe fiber reinforced concrete 24
2.7 Chain-of-bundles, or series-parallel, system 26
2.8 Damage of a bar under uniaxial tension [Murakami, 1988] 26
2.9 Force-displacement curves for different values of the shape factor m in the Weibull strength distribution 34
2.10 Regular triangular lattice model and circular disk particle model, corresponding to a square lattice model 34
2.11 Crack states corresponding to increasing deformation levels in a lattice model simulation of a single edge notched (SEN) concrete specimen subject to uniaxial tension [Schlangen, 1993] 37
2.12 RVE window cut out from a triangular lattice model and subjected to a deformation [Ostoja-Starzewski and Wang, 1989] 37
2.13 Molecular structure in a carbon fiber [Christensen, 1994] and in ice [Petrenko and Whitworth, 1994] 40
2.14 Different phases of microscale damage in concrete [Mazars, 1986] . . . 48
2.15 Voronoi polygon structure. [Gibson and Ashby, 1988] 48
2.16 Johnson-Mehl structure for a slow (left) and fast growth rate (right) . 55
2.17 Typical random network and force-displacement curves 55
2.18 Variation of randomness in the lattice by restricting the position of the nodes to a sub-area of the original cells [Schlangen, 1993] 57
2.19 Projection of lattice on grain structure and definition of beam materials [Schlangen, 1993] 57
2.20 A window in the microstructure of a Voronoi tessellation and a matrix-inclusion composite [Ostoja-Starzewski, 1994] 63

3.1 (a) Continuous and (b) micro-mechanical beam model 70
3.2 Progressive failure of a parallel bar system for $n = 4$ springs 70

3.3 Mean force-displacement behavior of parallel bar model for different probability distributions of stiffness k ($n = 10$ springs) 72
3.4 Standard deviation of force-displacement behavior of parallel bar model for different probability distributions of stiffness k ($n = 10$ springs) . 72
3.5 Influence of the COV of lognormal micro-stiffness on the average macroscopic force-displacement curve ($n = 10$) 74
3.6 Influence of the COV of lognormal micro-strength on standard deviation of macroscopic force-deformation curve ($n = 10$) 74
3.7 Expected value of damage accumulation during tensile test for different choices of the PDF for $\varepsilon_{\max}$ ($n = 10$, COV($\varepsilon_{\max}$) = 20%) 77
3.8 Standard deviation of damage accumulation during tensile test for different choices of the PDF for $\varepsilon_{\max}$ ($n = 10$, COV($\varepsilon_{\max}$) = 20%) . . 77
3.9 Analysis of continuous beam model, subject to pure bending 85
3.10 Comparison of moment-curvature diagram for a discrete spring model ($n = 10$) and for a continuum model using a deterministic failure strain $\varepsilon_{\max}$ 85
3.11 Average damage accumulation in spring system subject to bending ($n = 10$ springs, COV($\varepsilon_{\max}$)= 20%) 88
3.12 Average damage accumulation in spring system subject to bending for different values of COV($\varepsilon_{\max}$) ($n = 10$ springs, lognormal distribution for $\varepsilon_{\max}$) 88
3.13 Standard deviation of D in spring system subject to bending ($n = 10$ springs, COV($\varepsilon_{\max}$) = 20%) 90
3.14 Standard deviation of D in spring system subject to bending for different values of the COV of the lognormal distribution for $\varepsilon_{\max}$ ($n = 100$ springs) 90
3.15 Impact of correlation length l_c on average moment-curvature diagram ($n = 100$ springs) 91
3.16 Impact of correlation length l_c on COV of moment-curvature diagram 91

4.1 Sample discrete microstructures and equivalent homogenized random continuum 98
4.2 Deformed microstructures 98
4.3 Examples of random periodic microstructures: periodic inclusion model [Ostoja-Starzewski et al., 1994] and periodic cell model [Okabe et al., 1992] 103
4.4 Square lattice microstructure and corresponding discrete particle model (circular disks assumed for particle model) 103
4.5 Triangular lattice microstructure and corresponding particle model (circular disks assumed for particle model) 110

4.6 Discrete microstructure in homogenization window 110
4.7 Computation of nodal forces, required for a force-based homogenization 121
4.8 Local averaging of random field 121
4.9 Definition of distances needed to evaluate the covariance function . . 128
4.10 Impact of the boundary modeling technique on the average values of the elastic material properties 128
4.11 Networks with stray links 130
4.12 Impact of boundary modeling on correlation structure 130
4.13 Boundary modeling using boundary strips, as suggested by Gasparini et al. (1996) 132
4.14 Micromechanical modeling of a material 132
4.15 Sample compression test used to assess the quality of the boundary modeling 134
4.16 Correlations between n_{strip} and F_y using boundary model by Gasparini et al. (1996) obtained from 4000 Monte Carlo simulations on square specimens 250×250 135
4.17 Correlations between n_{strip} and F_y using suggested improved boundary model obtained from 4000 Monte Carlo simulations on square specimens 250×250 135
4.18 PDF of the horizontal reaction force F_x, obtained using 4000 Monte Carlo simulations (specimen size: 100×100) 139

5.1 Dependence of $\mathbb{E}(C_{11})$ and $\mathrm{StDev}(C_{11})$ on the density of the nodes λ for constant stiffness K and window size 50×50 142
5.2 Normal probability plots for C_{ij} (window size 100×100, nodal density $\lambda = 0.01$) 142
5.3 Normal probability plots for C_{ij} (window size 10×10, nodal density $\lambda = 0.01$) 144
5.4 Expected value of the elastic moduli C_{ij} as a function of the homogenization window size. 144
5.5 Gumbel plot for C_{11}/K and C_{12}/K (10,000 simulations, density $\lambda = 0.01$) 150
5.6 VRF of $\mathrm{Var}(C_{11})$ and $\mathrm{Covar}(C_{11}, C_{12})$ for square homogenization windows (dots indicate simulation results) 150
5.7 Iso-correlation contours for locally averaged random fields 151
5.8 Directional dependence of VRF γ for C_{11} 153
5.9 Comparison of isotropic and orthotropic microstructure (approximately 400 nodes in each network) 153
5.10 FE mesh and deformed state of square disk with hole, subject to uniform displacement at right edge 158

5.11 Evaluation of the covariance of a locally averaged random field over triangular finite elements 158
5.12 Three-way comparison of response statistics of square disk 159
5.13 Contour plots for the average vertical displacement u_y and the standard deviation of u_y, obtained using Model 1 and 2. 159
5.14 Effect of uncertainty associated with K on the average elastic modulus C_{11} 162
5.15 Effect of uncertainty associated with K on $A\mathrm{Var}(C_{11})$ of the elastic modulus C_{11} 162
5.16 Sample microstructures obtained as Delaunay triangulations of three different node-generating point processes 165
5.17 Comparison of the PDF of the link lengths resulting from the use of three different spatial random processes (density $\lambda = 0.01$) 165
5.18 Comparison of the correlation length of C_{11} resulting from the use of three different spatial random processes (nodal density $\lambda = 0.01$) . . . 168
5.19 Comparison of mean value of C_{11}, obtained using different homogenization techniques 170
5.20 Comparison of $A\mathrm{Var}(C_{11}/K)$, obtained using different homogenization techniques 170

List of Abbreviations

CDF	Cumulative Distribution Function
COV	Coefficient Of Variation
ELS	Equal Load Sharing
FE	Finite Element
FOSM	First-Order Second-Moment
HSC	High-Strength Concrete
IID	Independent, Identically Distributed
LLS	Local Load Sharing
MCS	Monte Carlo Simulation
MLL	Maximum Likelihood
NSC	Normal-Strength Concrete
PDF	Probability Density Function
RF	Random Field
RNG	(Pseudo-)Random Number Generator
RV	Random Variable
RVE	Representative Volume Element
RVF	Response Variability Function
SFEM	Stochastic Finite Element Method
SH	Statistically Homogeneous
VRF	Variance Reduction Function

List of Symbols

Uppercase Roman Letters

A	area of homogenization window
B_Z	covariance function of random field Z
$\mathbf{B}$	transformation matrix used in strain-controlled homogenization
$\tilde{\mathbf{B}}$	transformation matrix used in uniform strain homogenization
$\mathbf{C}$	elasticity matrix
$\mathrm{COV}(\cdot)$	coefficient-of-variation operator
$\mathrm{Covar}(\cdot)$	co-variance operator
D	damage variable
E	Young's modulus
$\mathbb{E}(\cdot)$	expectation operator, when used in text and captions
$\mathrm{E}(\cdot)$	expectation operator, when used in graphs and figures
F	force
$F_{\mathbf{X}}(\mathbf{x})$	the cumulative distribution function of $\mathbf{X}$
F', F''	boundary forces required for stress-controlled homogenization
$\mathbf{H}$	transformation matrix used in stress-controlled homogenization
K	stiffness parameter of discrete micromodel
M	bending moment applied to parallel bar system
P	axial load applied to parallel bar system
$\Pr(\cdot)$	probability operator
R	auto-correlation function
R_A	auto-correlation function of locally averaged random field Z_A
S	stiffness coefficient in discrete micro-mechanical model
$U^{(c)}$	strain energy stored in continuum model
$U^{(d)}$	strain energy stored in discrete model
$\mathrm{Var}(\cdot)$	variance operator
X_A	random field X, locally averaged over area A
Y_B	random field Y, locally averaged over area B
Z	random field
Z_A	locally averaged random field

Lowercase Roman Letters

$\mathbf{f}$	flexibility matrix of the discrete microstructure
$f_{\mathbf{X}}(\mathbf{x})$	the probability density function of $\mathbf{X}$
h	hazard or instantaneous failure rate
l_c	correlation length
ℓ	length of member in lattice model
m	model parameter in VRF function
n	number of springs, model parameter in VRF function
n^*	number of failed springs
n_b	number of boundary nodes
n_i	number of internal nodes
$\mathbf{u}$	nodal displacement vector
w_c	elastic strain density in homogenized continuum
w_d	elastic strain density in discrete micromechanical model

Lowercase Greek letters

α	characteristic area
β	randomness parameter for mesh generation
γ	Variance Reduction Function
δ	scale of lattice network
ε	strain component
λ	density of network
ν	Poisson's ratio
θ_x	scale of fluctuation in x-direction
ρ	correlation coefficient
$\boldsymbol{\sigma}$	stress component vector
σ_X	standard deviation of X
$\boldsymbol{\tau}$	lag vector, averaging domain
υ	curvature of beam

Chapter 1

Introduction

1.1 Motivation

Due to recent advances in the development of the Stochastic Finite Element Method (SFEM) it has become possible to analyze the behavior of structures, in which the material properties are modeled as time- or space-variant random fields. This progress is reflected in the literature where a wide range of applications of the SFEM can be found: linear-elastic analysis of beams [Vanmarcke and Grigoriu, 1983], structures which include geometric [Liu and Der Kiureghian, 1991] or material nonlinearities [Zhang and Ellingwood, 1996] and structures with deteriorating material properties [Orisamolu, 1998].

Most random field models used to be restricted to primarily one- or multi-dimensional Gaussian fields [e.g. Shinozuka and Jan, 1972; Yamazaki and Shinozuka, 1990; Fenton and Vanmarcke, 1990; Shinozuka and Deodatis, 1991; Elishakoff et al., 1994; Shinozuka and Deodatis, 1996; Lin et al., 1997]. However, significant progress has also been made in the simulation of non-Gaussian random fields [Yamazaki and Shinozuka, 1988] and in applications of the SFEM with multiple non-Gaussian fields [Ghanem, 1999].

In most SFEM applications, the random field description of the material properties is assumed to be either known or given. The simplest option consists of a straightforward randomization of deterministic constitutive models. In the case of a

linear elastic analysis for instance, typically only Young's modulus is assumed to be random [Zhang and Ellingwood, 1995], but examples where Poisson's ratio is considered a random field are available [Shinozuka and Yamazaki, 1988]. Cross-correlated random fields of Young's modulus E and Poisson's ratio ν are considered in Graham and Deodatis (1996).

Deterministic constitutive models usually provide a description of the overalll, or "average" macroscopic behavior. This is due to the fact that constitutive behavior is generally based on a statistical regression between loading and response. Consequently, a straightforward "randomization" of a given deterministic material model for the purpose of stochastic structural analysis may not be justified. Moreover, the material properties are usually measured in standardized tests, either directly or indirectly on the basis of a deterministic model. Since typically only one material property is determined per test, it is impossible to gain information regarding the joint distribution of the material parameters from test results. There seems to be no theoretical basis to infer the stochastic characteristics of the various material properties on the basis of such experiments.

An estimation of the random field parameters, including the correlation lengths and variances of the various material properties and the correlations between them, directly from lab tests would probably require a prohibitively large amount of tests. Accordingly, incomplete information needs to be supplemented by certain model assumptions. For instance, experimental evidence can be fitted to an assumed isotropic elastic model to result in the random field description, required for SFEM.

The correlation lengths of the random fields describing material properties can be quite difficult to obtain from experiments. This is particularly the case when the

data are correlated over large distances, such as in soil characteristics [Fenton, 1999a]. Two approaches can be taken to address this issue.

In one possible approach, safe upper bounds on the variability, which are independent of the auto-correlation of a random field, are calculated. In an SFEM context this approach is developed in Deodatis and Shinozuka (1989) and Deodatis (1990). Applications of this method to 2D plane stress and plane strain problems are described in Wall and Deodatis (1994). The method has been extended by Graham and Deodatis (1998) to include plate bending elements. It should be mentioned that, in its current formulation, these upper bounds depend on the amount of correlation between the various random fields. An analysis of the dependence of the upper bounds of the response variability on the correlation between E and ν in a plate bending problem is performed in Deodatis and Graham (1998).

A second approach, which is taken in this dissertation, is to develop a more consistent framework where the random field characterization of elastic properties is based on simple micro-mechanical models for the material. Any available macroscopic test data can then be used to validate and/or calibrate the overall framework. It will be shown that the suggested approach results in improved and consistent models for correlation lengths in the constitutive random fields as well as for cross-correlations between the different material properties.

1.2 Blending Discrete and Continuum Models

Several civil engineering materials, such as concrete, soil, rock, wood and ice, are assemblies of discrete constituents. In the case of concrete these constituents are

the granulates, sand and cement paste. Even though such materials are intrinsically heterogeneous, they are quite often treated as continua for the purpose of structural analysis. This is justifiable since the scale of the microstructure is much smaller than the scale of the structure or the structural component. For instance, the granulates in concrete are about 1 cm in diameter, which is much smaller than the size of a bridge or a bridge girder. The assumption that a sufficiently large sample of randomly distributed and oriented constituents results in a homogeneous material, provides a justification for using a continuum theory [Lemaitre and Chaboche, 1985].

When the microscopic variation of the material is of no practical interest, the material can be homogenized as follows [Sab, 1992]: a sufficiently large volume of the material is submitted to a stress or strain state that would produce a uniform stress or strain in a homogeneous medium. The effective properties of the material, which relate the volume-averaged stresses to the volume-averaged strains of the material, are considered to be the same as for the homogeneous medium [Hill, 1963].

In the present context, the smallest volume element for which a material can be considered macroscopically homogeneous is defined as the representative volume element (RVE). The size of the RVE depends on the size of the inhomogeneities, which varies for different types of material as illustrated in Table 1.1.

Depending on the application, a material, which consists of discrete constituents, can be modeled using one of the following two approaches:

- the *continuum approach*: the material is treated as a homogeneous continuum, irrespective of the microstructure of the material.

- the *discrete approach*: the material is modeled explicitly as an assembly of

discrete constituents. The macroscale behavior of the material is obtained from the mechanical interaction between the constituent particles.

The main advantage of the continuum approach is that structural analysis is much faster than for the discrete approach, but it is easier to account for the heterogeneities in the material when a discrete model is used. Which approach is most convenient, depends on the application. The validity of the homogeneity assumption hinges on the relative magnitude of the heterogeneities in the material with respect to the structural scale. As long as the structural scale is larger than the RVE the material can be considered macroscopically homogeneous. The continuum approach lies at the basis of most structural analysis methods in civil engineering.

However, if the analysis requires a detailed study of local effects, a discrete or a mixed continuum-discrete model may turn out to be more appropriate. A mixed model combines the advantages of both approaches: the computational efficiency of the continuum model is used wherever possible, but the detail of the discrete modeling is implemented wherever necessary.

The inelastic behavior of materials is to a very large extent determined by micro-mechanics, such as the presence of micro-defects, the movement of dislocations, and the nucleation and growth of microcracks. The discrete nature of some of these effects indicates that a continuum theory can only provide an overalll description of the material behavior on the macroscale. An example can be found in the fracturing process in a material such as ice or concrete where strain localization plays an important role in the damage accumulation process.

Often benefit can be gained from the modeling of materials on a smaller geomet-

Material	Inhomogeneities	Representative Volume Element
Metals and alloys	Crystals $1\mu m - 0.1mm$	$0.5 \times 0.5 \times 0.5mm$
Polymers	Molecules $10\mu m - 0.05mm$	$1 \times 1 \times 1mm$
Soil	Particles $10\mu m - 1mm$	$5 \times 5 \times 5mm$
Wood	Fibers $0.1mm - 1mm$	$1 \times 1 \times 1cm$
Concrete	Granulates $\simeq 1cm$	$10 \times 10 \times 10cm$

Table 1.1: Orders of magnitude of Representative Volume Elements (based on Lemaitre and Chaboche, 1985)

Scale	Volume Element	Defect	Model
Micro	Hardened cement paste, xerogel, aggregate	Atomic voids, crystal defects	Material science models
Meso	unit cell containing statistically homogeneous sample of phases	Microcrack, large pores	Micromechanical models
Macro	Concrete specimen	Macrocrack	Continuum theories, fracture mechanics

Table 1.2: Hierarchy of structural scales defining the mechanical response of concrete [Krajcinovic and Fanella, 1986]

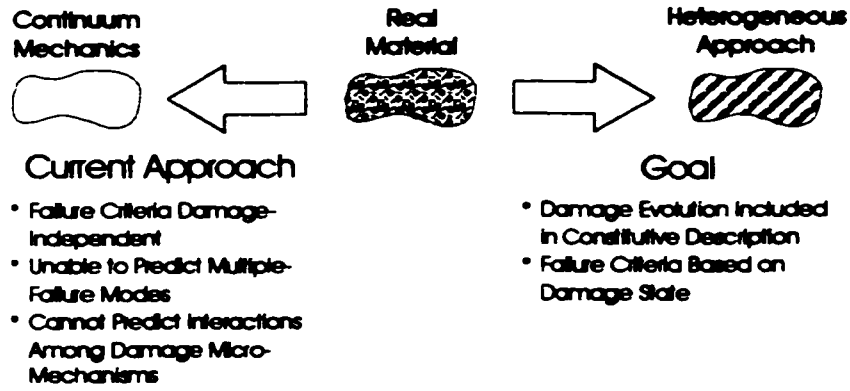

Figure 1.1: The principle of mesomechanics [Haritos et al., 1988]

rical scale since new knowledge and insight can be gained about the macro-behavior if the micro-behavior is properly understood [Cundall and Hart, 1992]. Table 1.2 gives an illustration of the different scales at which concrete can be modeled. The study of the interaction of the granulates and the growth of the microcracks leads to a better understanding of the macroscopic behavior of concrete. This field of research is known as mesomechanics [Haritos et al., 1988] and Figure 1.1 summarizes the main differences with the classical continuum approach.

Mesomechanics try to describe the macroscale behavior on the basis of the microstructure in the material. As such, the particle shape and orientation must be included in the mesomechanical model. A second challenge is to link the changes in this microstructure with the structural mechanics behavior on the macroscale. This is intrinsically different from continuum mechanics failure theories, which are based on a phenomenological description of local effects [Haritos et al., 1988].

Another factor is the apparent randomness of the structural behavior of materials at the macroscale. Material modeling is often characterized by several uncertainties such as: packing densities, distribution of initial defects in the material, inclusion of other phases or particles, and strength and stiffness of the constituents. Each of these factors may have important ramifications on the variability of the structural behavior which suggests the framework of a probabilistic model [Breysse et al., 1994]. The apparent randomness in the microstructure leads to variability in the failure loads and may even lead to different failure modes.

1.3 General Approach and Objectives

The general approach guiding this research rests on the following ideas:

- To model the microstructure and micromechanical interactions in a structural material. Both the geometrical and the mechanical characteristics of the discrete constituents on the microscale are described probabilistically.
- To derive the macro-mechanical properties of an equivalent macro-continuum model of the material from the mechanical interactions between the discrete constituents on the microscale.
- To investigate the relationship between the geometrical and mechanical probabilistic parameters on the microlevel and the stochastic properties of the random field description of the equivalent macroscale continuum.

The main conjecture of this work is the belief that the variability of the macroscopic material characteristics, such as the strength and stiffness of a structural component, results chiefly from the discrete character of the microstructure in the material [Ostoja-Starzewski et al., 1994].

The objective of this research is to develop a stochastic framework for the homogenization of materials for which the material properties of the equivalent continuum are consistent with the micro-structure. The modeling on the micro-scale is restricted to interactions of mechanical nature only; electrochemical or thermal processes are not considered. The random fields, developed for the equivalent continuum, can subsequently be used in a SFEM for structural analysis. With this homogenization-based procedure, a more consistent description of the variability of the macroscopic

structural behavior is achieved than when some or all of the material properties in a deterministic constitutive model are modeled as independent random fields.

The original contribution of this research is:

1. A new homogenization procedure, which is based on equivalence of strain energy under an assumed stress distribution along the boundary of homogenization window in the continuum and the discrete micro-mechanical model, is formulated. The method complements existing techniques for homogenization, which are based on assumed strain states in the material.

2. Shortcomings of existing boundary condition models currently used in the analysis of discrete micro-mechanical systems are identified and an improved boundary modeling technique is introduced. Theoretical considerations, as well as numerical examples, illustrate the superior performance of this modeling.

3. A new random field modeling of linear elastic materials is proposed. The model is consistent with the microstructure in the material and allows to estimate the auto- and cross-correlations of the elastic properties directly from the microstructure.

1.4 Notations and Definitions

Some time needs to be spent on consistent notations and definitions, particularly with respect to probabilistic concepts. In this work, we follow the definitions given in Vanmarcke (1983) and Papoulis (1991). To avoid all confusion about their precise meaning, the definitions and notations of some terms are listed in this section. Bold

notation is used for vectors. Random variables are indicated by uppercase notation, while lowercase notation is used for specific values of these random variables.

- **Random Variable (RV):** a random variable X is a rule for assigning a number to every outcome of an experiment.

- **Cumulative distribution function (CDF):** the CDF of the random variable X is the function $F_X(x) = \text{Prob}(X \leq x)$ and is defined for every $x \in (-\infty, \infty)$

- **Probability density function (PDF):** the PDF of a continuous RV is defined as the derivative

$$f_X(x) = \frac{dF_X(x)}{dx} \tag{1.1}$$

- **Expected value:** the expected value of the continuous RV X is defined by the integral:

$$\mathbb{E}(X) = \int_{-\infty}^{\infty} x f_X(x) dx \tag{1.2}$$

- **Covariance of two random variables X and Y:** the covariance of two RVs X and Y is by definition:

$$\begin{aligned} \text{Covar}\,[X, Y] &= \mathbb{E}\,[(X - \mathbb{E}(X))(Y - \mathbb{E}(Y))] \\ &= \mathbb{E}(X.Y) - \mathbb{E}(X)\mathbb{E}(Y) \end{aligned} \tag{1.3}$$

  The value Covar $[X, X]$ is equal to the variance $\text{Var}(X)$.

- **Correlation coefficient:** the correlation coefficient ρ, or ρ_{XY}, of the RVs X and Y is defined as the ratio:

$$\rho = \frac{\text{Covar}\,[X, Y]}{\sqrt{\text{Var}\,(X)\,\text{Var}\,(Y)}} \tag{1.4}$$

- **Random Field (RF):** a n-dimensional random field $Z(\mathbf{x})$ is a rule for assigning a function $z(\mathbf{x})$, $\mathbf{x} = (x, y)$, to every outcome of an experiment. In the two-dimensional case, a RF is a family, or ensemble, of functions depending on the field parameters x and y. The second-order properties of random variables can be extended to random fields using the following definitions:

- **Expected value:** the expected value, or mean, of the continuous two-dimensional RF $Z(x, y)$, defined over an area A, is defined as:

$$\mathbb{E}(Z(x,y)) = \frac{1}{A} \iint_A Z(x,y)dxdy \tag{1.5}$$

- **Autocovariance function:** the (auto)covariance function $B_Z(\mathbf{x}, \mathbf{x}')$ of the continuous RF Z is defined as the covariance of the RVs $Z(\mathbf{x})$ and $Z(\mathbf{x}')$ at two locations $\mathbf{x}$ and $\mathbf{x}'$:

$$B_Z(\mathbf{x}, \mathbf{x}') = \text{Covar}\left[Z(\mathbf{x}), Z(\mathbf{x}')\right] \tag{1.6}$$

  The value $B_Z(\mathbf{x}, \mathbf{x})$ is equal to the variance $\text{Var}(Z(\mathbf{x}))$. If the random field is statistically homogeneous, the covariance function depends only on the distance $\boldsymbol{\tau} = \mathbf{x} - \mathbf{x}'$: $B_Z(\mathbf{x}, \mathbf{x}') = B_Z(\boldsymbol{\tau})$. Only (statistically) homogeneous RFs are considered in this dissertation.

- **Crosscovariance function:** the crosscovariance function B_{XY} of two homogeneous random fields X and Y is defined as:

$$B_{XY}(\mathbf{x}, \mathbf{x}') = \text{Covar}\left[X(\mathbf{x}), Y(\mathbf{x}')\right] \tag{1.7}$$

- **Correlation function:** is here defined as the autocovariance of the normalized random field $Z(\mathbf{x})/\sqrt{\text{Var}\,(Z(\mathbf{x}))}$:

$$R(\mathbf{x}, \mathbf{x}') = \frac{\text{Covar}\,[Z(\mathbf{x}), Z(\mathbf{x}')]}{\sqrt{\text{Var}\,(Z(\mathbf{x}))\,\text{Var}\,(Z(\mathbf{x}'))}} \tag{1.8}$$

1.5 Outline

In Chapter 2, a general overview of micro-mechanical modeling is presented. The advantages, shortcomings and drawbacks are clearly indicated. Practical guidelines for the selection of appropriate micro-mechanical models are given.

A one-dimensional model for the progressive failure of materials, which are subject to normal stresses only, is presented in Chapter 3. The so-called parallel-bar model clearly shows how complex macroscopic behavior can easily be modeled on the basis of a simple micro-mechanical constitutive model. The additional insight into the structural behavior of a material that can be gained from a micro-mechanical analysis is demonstrated by means of examples. The micro-mechanical model results in a more accurate modeling of the uncertainty of the structural behavior of a material.

It is explained how many of the shortcomings of the parallel-bar model are related to the fact that the dimensions of the actual, physical microstructure are not represented in the model. For this reason, all micromodels, used in subsequent chapters, reflect the actual microstructure.

A stochastic homogenization theory for linear elastic microstructures, subject to 2D plane stress, is presented in Chapter 4. Based on existing research regarding deformation-based homogenization, a new homogenization technique, based on

a strain energy equivalency and a constant stress assumption in the FE analysis, is introduced. Also, an improved modeling of the geometric boundary conditions is suggested. Based on locally averaged random field theory, a novel approach to modeling variability of linear elastic materials, which is consistent with the micro-structure in the material, is developed. This improved random field material modeling can readily be used in a FE analysis.

The examples in Chapter 5 illustrate the significance of the more consistent random field modeling for structural reliability applications. It is shown how isotropy of materials is achieved in a mean sense only. This has some important ramifications on the variance of maximum stresses, strains and deformations. Several examples illustrate this. Conclusions and recommendations for further research are presented in Chapter 6.

Chapter 2

Micro-Mechanical Modeling of Materials

2.1 Introduction

In this chapter various micromechanical models are reviewed. Micromechanical models describe the material behavior at the mesoscale (Table 1.2) and form the cornerstone of the mesomechanics approach: the macroscopic material behavior description is obtained as the result of the deformations and interactions between the micromechanical constituents [Haritos et al., 1988]. From a structural analysis point of view, the modeling of the variability of material behavior on a scale smaller than the mesoscale (Table 1.2), holds no practical interest.

For these reasons, micromechanical models are the backbone of the uncertainty modeling approach in this research: macroscale uncertainty of material behavior is modeled as the result of the uncertainties associated with the micromechanical model (Figure 2.1).

Every element or unit cell in a micromechanical model is described using classical mechanical analogs, such as springs and dashpots. The behavior at the macroscale can be derived from the mechanical interaction between these unit cells.

The emphasis of this overview is on the topology of the models and the interaction mechanisms between the constitutive elements. Many of the discrete particle or network models were originally developed by material scientists for the study of metals and (fiber) composite materials [Christensen, 1994]. Even though the geometrical

scale may be quite different, the topology of many heterogeneous civil engineering materials can be described by one of these models.

The review starts with one-dimensional models. The study of the macroscopic structural behavior of one-dimensional discrete models, such as parallel bar and chain-of-bundles spring systems, is extremely useful from a theoretical point of view. Subsequently, the topological characteristics of multi-dimensional models with regular and random microgeometries are presented and their impact on the macroscale structural behavior is discussed. Some shortcomings of the homogeneous continuum approach are highlighted. Different modifications to the continuum theory which have been put forward in the literature are also discussed.

The analytical formulae, which describe the constitutive behavior of the one-dimensional models, form a link between the multi-dimensional discrete and continuum approaches using random fields and stochastic finite element models.

2.2 Constitutive Modeling

2.2.1 Effects of the Microstructure

In classical continuum mechanics the material is assumed to be homogeneous and continuous. Continuum mechanics models are known as local models: because of the homogeneity assumption, it makes sense to define stresses and strains at one point, where this point is considered as a limiting case of a small elementary area or volume. Because of the local approach a continuum theory can use differential calculus as its mathematical description tool.

As mentioned before, the homogeneity assumption is no longer valid for a volume

element smaller than the RVE. The inelastic behavior of the material may be hard to describe by a general continuum theory since the sources of inelasticity may stem from a variety of deformation and damage mechanisms on the microscale [Haritos et al., 1988]. The relation between the microstructure and the material characteristics is studied in the material sciences. However, the detail, required for many of these models, is beyond the scope of this research. For practical reasons, only mechanical interactions on the mesoscale (see Table 1.2) can be considered here.

The microstructure of a typical engineering material is not homogeneous but consists of discrete grains or particles, with discontinuities such as microcracks, voids, inclusions, dislocations, and grain boundaries (Figure 2.2). During elastic deformation no new microcracks nucleate and all existing defects follow the displacements of the surrounding material without growing [Krajcinovic and Mastilovic, 1995].

Plasticity is characterized by an irreversible flow of material through the elastic lattice via dislocations. Plastic deformation does not affect the material stiffness, since the lattice structure remains elastic. In a descriptive theory, this means that the stress-strain curve remains parallel to the initial elastic segment during unloading or upon reloading (Figure 2.3a).

Damage on the other hand, is associated with the activation of the existing cracks and the nucleation of new microcracks. It is caused by important local deformations due to decohesion [Lemaitre and Chaboche, 1985]. The material does not flow during the damage accumulation process. Consequently, damage is also characterized by the absence of irreversible macroscopic strains; upon unloading the material returns to a zero strain state. However, since the material structure is damaged, its stiffness is reduced (Figure 2.3b).

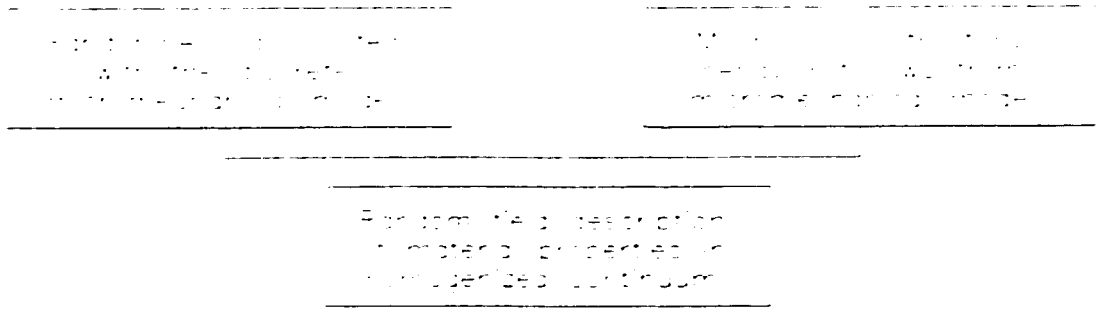

Figure 2.1: General approach for modeling of the uncertainty of the macroscopic structural behavior of materials

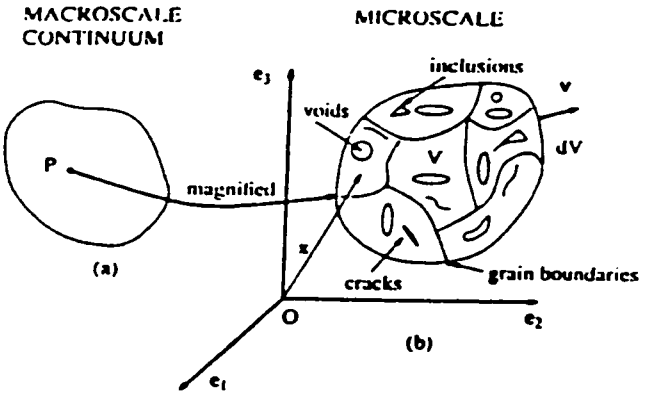

Figure 2.2: Possible microstructure of an RVE at a point in a macroscopic continuum [Nemat-Masser and Hori, 1993]

In a pioneering paper dated 1958. Kachanov introduces two sets of internal variables. each describing one of the two mechanisms:

- *Plasticity* is associated with the propagation of dislocations. The plastic strain, or a function thereof. is an appropriate choice for the internal variable.
- *Damage* characterizes the evolution of micro-defects. The stiffness, or a function thereof, is an appropriate choice for the internal variable.

It has already been mentioned that the continuum approximation is no longer correct at the meso or micro scale. As a consequence, it is preferable to talk about forces and displacements for heterogeneous materials. rather than stresses and strains.

2.2.2 Classification of Constitutive Models

Constitutive models can be classified in 3 groups [Krajcinovic and Silva, 1982]:

- "Macroscale models" which describe the macrostructural behavior from a purely phenomenological point of view. These models are characterized by the use of explicit stability-instability criteria, separate from the stress-strain response [Bažant and Cedolin, 1991]. For every failure mode, a separate criterion is required.
- Generalized "materials science models" seek to construct a general theory which explains the macroscopic structural behavior based on a profound understanding of the atomic or molecular structure of the material [Christensen, 1994].

- "Statistical models" try to explain the randomness or the variability in the material behavior as a result of the discrete nature of the mesostructure [Ostoja-Starzewski and Wang, 1989]. Inelastic behavior is modeled at the mesoscale, damage is assumed to take place at the grain-boundaries only [Ostoja-Starzewski, 1989].

The materials science models try to explain the macroscale behavior based on an atomic or molecular model. So far, their application has been successful in a few special cases only [Christensen, 1994]. In addition, the computational cost of these models is considered too high to be practically workable for structural applications.

Statistical models may therefore prove to be a valuable alternative to the classical macrostructural methods, since they can inherently account for the material variability. These models are still based on descriptive theories, but since they include the mesostructure of the material, they form a compromise between the classical structural mechanics methods and the material science models. Since damage evolution is included in the constitutive description of the material, there is no longer a need for separate macroscale instability criteria.

In the following review the emphasis will be on a statistical description of the material variability. The variability is a consequence of:

- variability in the microstructural geometry
- variability in the microscale strength and stiffness

2.3 One-Dimensional Models

2.3.1 Introduction

In this section, three one-dimensional models are discussed:

- the parallel bar or Daniels system
- the parallel-series model
- the chain-of-bundles or series-parallel model

Daniels (1945) originally formulated his parallel bar model to study the strength of textiles. The parallel-series model was used by Iwan (1967) to study the hysteresis of elasto-plastic members in cyclic loading. 2D and 3D models are the subject of the next section.

2.3.2 Micro-Constitutive Models

Parallel Bar Model

The parallel bar model [Gasparini et al., 1995] is the simplest constitutive model for uniaxial loading of materials with stochastically distributed material parameters (Figure 2.4a). The model was first known as the Daniels (1945) system. In one form or another, this model has been applied to uniaxial tension of plain [e.g. Gasparini et al., 1996; Kandarpa et al., 1996; Krajcinovic and Silva, 1982] and fiber reinforced concrete [Fanella and Krajcinovic, 1985], as well as bending of plain concrete [Krajcinovic, 1979].

In its simplest form, every bar is perfectly elastic-brittle and is characterized by a spring stiffness k and ultimate displacement δ_u, corresponding to a ultimate

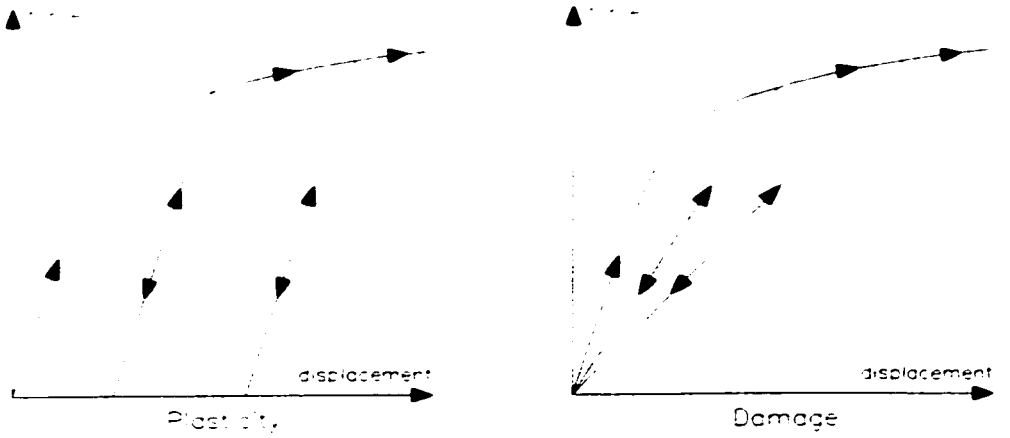

Figure 2.3: **Force-displacement diagrams for re-loading in the case of plasticity and damage.**

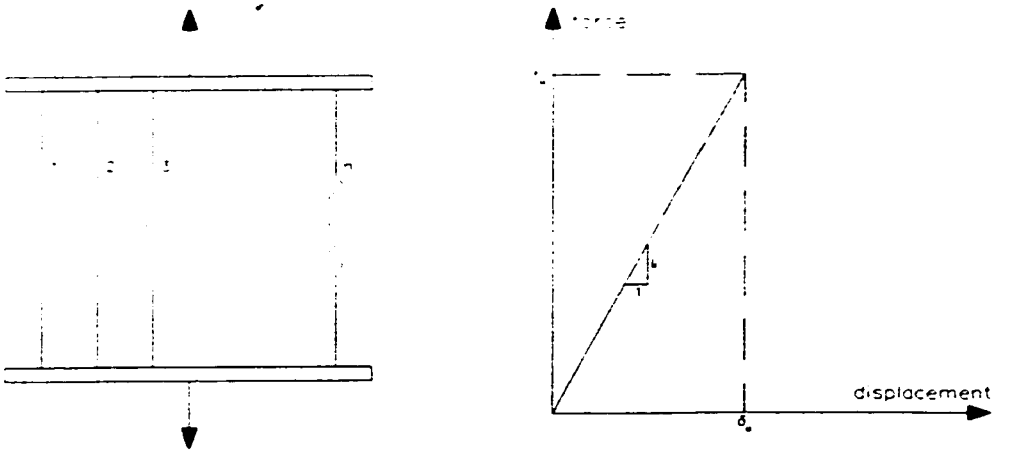

Figure 2.4: **Parallel bar model and elastic-brittle micro-constitutive relation**

force f_u (Figure 2.4b). Some, or all, of these parameters (k, δ_u, and f_u) are now considered random variables. Consequently, not all bars will fail simultaneously. The macroscopic behavior of the specimen is obtained from the mechanical interaction between the different bar elements. Depending on the form of the probability density function (PDF) of the material parameters, various shapes of the uniaxial force-displacement curve can be obtained for the parallel bar system.

The mechanical interaction between the different bars is defined by the load sharing rule. For the time being it is assumed that upon failure of one bar element its load is redistributed evenly among all surviving bar elements. The effect of this assumption on the system behavior will be discussed later.

Most "brittle" materials are not perfectly brittle but exhibit some level of ductility. This can easily be seen in a simple uniaxial test. In the case of a perfectly brittle material, all deformation vanishes upon complete unloading (Figure 2.3b). If the material is somewhat ductile, there will be a residual deformation after unloading (Figure 2.3a).

Ductility can be included in the model by replacing the spring elements with Jenkins elements, as shown in Figure 2.5 [Krajcinovic and Silva, 1982]. Each element is attributed a random value of the yield force f_y and the ultimate force f_u. If no hardening is considered, the element will either yield ($f_y < f_u$) or fracture ($f_y > f_u$). The brittleness index is defined as the fraction of brittle elements, and represents a measure for the degree of brittleness (or lack of ductility).

The material now has three load stages. The first one is linear elastic since no bar element has failed or yielded. Depending on whether the first bar fractures or yields, the intermediate stage, where only one type of failure has occurred, will be

elastic-brittle or ductile. In the last load stage, where both types of failure have occurred, the material exhibits a mixed behavior. There is damage accumulation due to the failure of some bar elements, and the system does not return to a zero strain state upon unloading because of the yielding of some bars.

Parallel-Series Model

Fanella and Krajcinovic (1985) modified the original parallel bar model to describe the uniaxial tensile behavior of fiber reinforced concrete (FRC). Each of the bars now consists of a parallel system itself. This secondary system represents the material matrix and the fibers (Figure 2.6). All constituents are linear elastic-brittle, but have random strength. The matrix fails in tension only. The fibers have two failure modes: tensile failure of the fibers and failure by pull-out, i.e. the fibers separate from the matrix. The macroscopic behavior is qualitatively similar as for the original parallel bar model.

Chain-of-Bundles Model

The chain-of-bundles or series-parallel system has attracted some research interest as well. Here only a series of linear elastic-brittle parallel bar systems is considered (Figure 2.7), but other constitutive behavior has been studied [Iwan, 1967]. As such it is yet another ordered system used to simulate uniaxial material behavior. It will be shown that its macroscale behavior is totally different from the above parallel bar model.

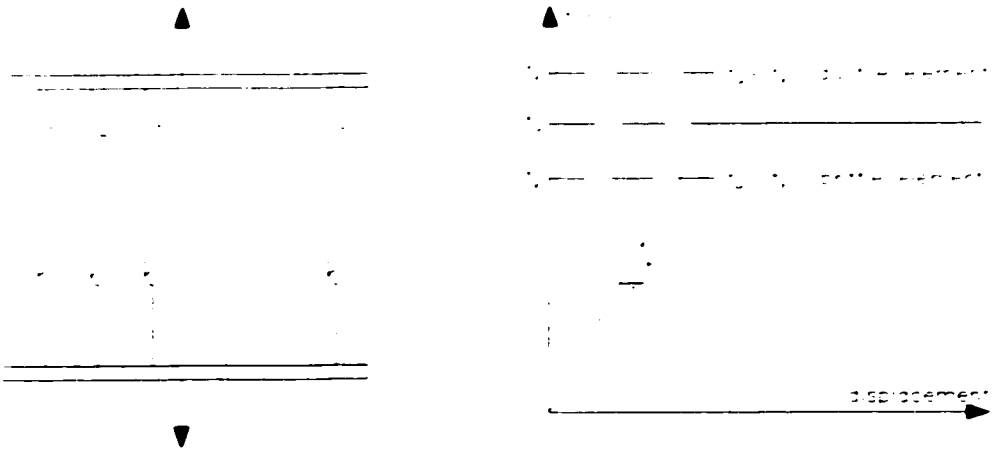

Figure 2.5: **Parallel system of Jenkins elements and micro-constitutive relation**

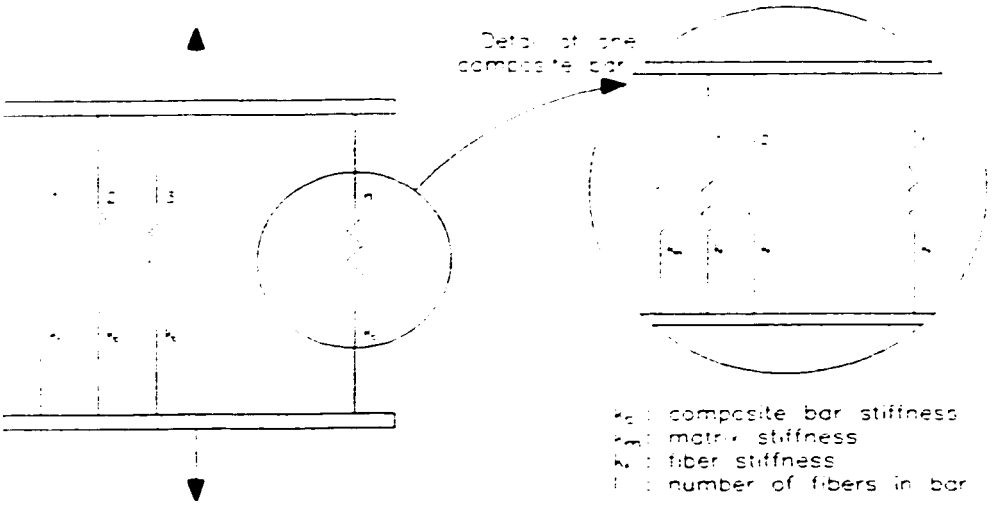

Figure 2.6: **Series-parallel system used by Fanella and Krajcinovic (1986) to describe fiber reinforced concrete**

2.3.3 Damage Variable

Consider the tensile bar in Figure 2.8a. In Kachanov's original one-dimensional formulation, the damage variable D is defined as the ratio of the area of the cracks and voids in the material to the total cross-sectional area A_0. As such, the damage variable represents the surface density of the discontinuities in the plane normal to the loading axis.

A fictitious, undamaged tensile bar of the same material would behave macroscopically identically to the actual damaged specimen if it had a cross section equal to the effective area $(1 - D)A_0$ of the damaged specimen. Because of its smaller cross section, the fictitious bar in Figure 2.8c will be less stiff than the undamaged specimen in Figure 2.8a. As such, the damage measure D is related to the effective stiffness. This reinforces the previously-stated belief that a proper choice for the damage variable should be related to the stiffness of the material [Krajcinovic and Mastilovic, 1995].

For the discrete parallel bar model (Figures 2.4 and 2.5), a damage variable can be defined as the fraction of ruptured bar elements. Since the global stiffness of the system is given as the sum of the individual element stiffnesses, the damage variable is again related to the effective stiffness of the assembly.

2.3.4 Randomness

Parallel Bar Model

In the discrete model, the probability distribution of the material parameters influences the macro-scale structural behavior of the specimen. Krajcinovic and Silva (1982) assume an identical stiffness k for all bar elements (Figure 2.4). The strengths

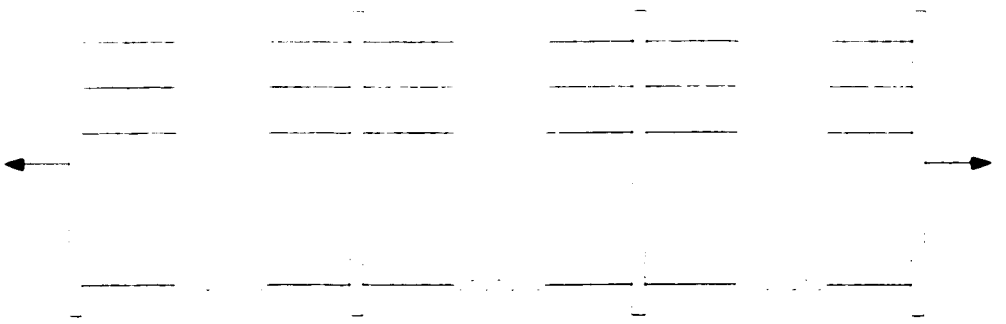

Figure 2.7: Chain-of-bundles, or series-parallel, system

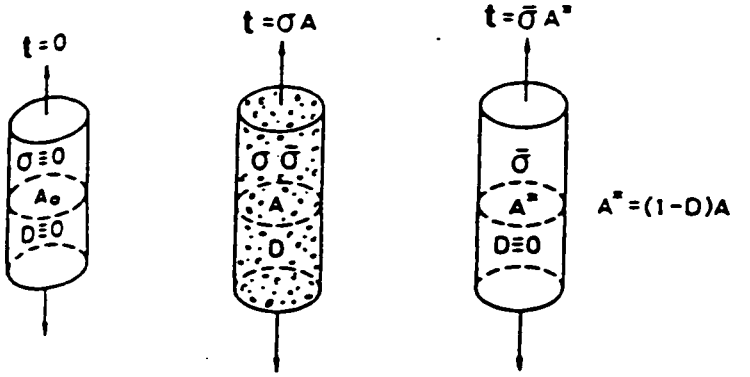

Figure 2.8: Damage of a bar under uniaxial tension [Murakami, 1988]

f_u of the individual bars are assumed to be independent, identically distributed (IID) random variables. This implies that the random field of bar strengths is homogeneous since the probability density function of the bar strengths is independent of the location of the bar in the system [Adler, 1981].

Since not all bars will fail at the same load value, the damage variable, which is defined as the fraction of ruptured bar elements, is probabilistic in nature and given by a binomial distribution. For a very large number of bars, the system can be regarded as a continuum. Depending on the probability distribution (PDF) and the parameter values in the particular PDF adopted for the individual bar strength, different damage evolution laws are obtained and different macroscale behavior is observed. This is illustrated in Figure 2.9 where the macroscopic damage evolution is compared for 3 different values of the shape parameter m in the Weibull distribution of the inidvidual bar strength.

Because the random field of the bar strength is homogeneous, the expected value of the damage function corresponding to an elongation δ is equal to the failure probability of one single bar for the same elongation δ. However, since all bars are assumed independent, it follows that the variance of the system strength decreases with the number of bars n. In the limit for $n \rightarrow \infty$, the variance of the system strength goes to zero and the system damage becomes deterministic. Since the variance of the system is affected by the number of bars in the system, this represents an important limitation of Krajcinovic and Silva's (1982) model.

Even though the model may represent the average behavior accurately, it is incapable of representing the variability in the response. Kandarpa et al. (1996) overcome this limitation by modeling the spring strengths as a homogeneous random

field with non-zero correlation. This modified model can account for the variability of the force-displacement behavior at the macroscale of brittle materials.

Kandarpa et al. (1996) derive analytical expressions for the mean and standard deviation of the force as a function of the imposed displacement. Using a lognormal distribution and an exponential correlation function for the failure strength of an individual bar, they obtain good comparison for the mean and variance of the force-displacement curves with experimental evidence for normal and lightweight concrete. They also prove that their model leads to the same deterministic result as obtained by Krajcinovic and Silva (1982) for the damage accumulation law in the continuum approximation if the individual bar strengths are uncorrelated.

Another approach is taken by Gasparini et al. (1996). Here, the failure of the Daniels system is described as a Markov chain process [Papoulis, 1991]. The continuum approximation for a large number of bar elements then establishes a link with the stochastic macroscopic models for damage accumulation, discussed by Bogdanoff and Kozin (1985). If the element strengths are independent and identically distributed (IID), the system strength of the continuum parallel bar model becomes deterministic, in accordance with the results obtained by Krajcinovic and Silva (1982) and Kandarpa et al. (1996).

Chain-of-Bundles Model

The strength of the chain of bundles system is that of its weakest bundle. A numerical study of the behavior of random chain-of-bundles networks is presented in Gasparini et al. (1996). All bars have the same deterministic stiffness k, and a Weibull distribution is assumed for the bar strength f_u. The simulations clearly

demonstrate the very brittle failure of these systems. This is easily explained. Upon failure of one bar, the bundle stiffness decreases and this causes larger deformations in the bundle. This leads to an increased probability of subsequent failures in the same bundle, resulting in a sudden collapse. In some of the simulations no individual bar failures are observed for loads up to 95% of the ultimate load.

2.3.5 Load Sharing Rules

In all the aforementioned models, it is assumed that after failure of one of the bars, the load is redistributed evenly among the remaining bars. This is true only for very stiff end plates and equal bar stiffnesses, which may not necessarily be a realistic assumption. Alternative load sharing rules are studied by Hohenbichler and Rackwitz (1983) and Phoenix and Smith (1983).

Hohenbichler and Rackwitz (1983) impose uniform strain on all bar elements. Since in their study the stiffnesses are not equal for all bars but randomly distributed, the load sharing is not even but it is proportional to the relative stiffness of the surviving bar elements.

Phoenix and Smith (1983) assume that upon failure of a bar element, half of its load is transferred to each of the adjacent surviving neighbors. They assume all bar strengths to be IID Weibull or power distributed random variables. Under these assumptions they establish an asymptotic expression for the PDF of the bundle strength. This work is an extension of a previous study [Smith and Phoenix, 1981] where they determined the bundle strength under equal load sharing conditions.

Mahesh et al. (1999) analyzed the strength of unidirectional fiber composites for different load sharing rules where all fiber strengths are assumed IID Weibull. A local

load sharing (LLS) model, which is a realistic load transfer model in a composite embedded in a matrix, is compared with the equal load sharing model (ELS), which is an accurate representation of a loose bundle of fibres. While in the local load sharing model a large part of the load carried by a breaking fiber is distributed amongst its nearest neighbors, broken fibers transfer their load equally amongst all surviving fibers in the ELS model. They obeserve that the stress-concentration driven failure of the LLS model and the strength-driven failure of the ELS form apparent upper and lower bounds on the bundle strength. Their Monte Carlo simulations indicate that the shape parameter of the Weibull distribution determines where the true failure load lies with respect to these upper and lower bounds.

2.3.6 Strength Probability Distribution of a Single Bar

Several choices have been adopted for the strength of a single bar: a normal [e.g. Burt and Dougill, 1977; Hohenbichler and Rackwitz, 1983; Rossi and Richer, 1987; Schlangen and Van Mier, 1992; Schlangen, 1993; Van Mier et al., 1996; Vervuurt et al., 1996], a lognormal [e.g. Jirásek and Bažant, 1994; Kandarpa et al., 1996], and a Weibull distribution [e.g. Smith and Phoenix, 1981; Krajcinovic and Silva, 1982; Phoenix and Smith, 1983; Rossi and Richer, 1987; Gasparini et al., 1996; Kandarpa et al., 1996; Breysse, 1990] are some popular choices. But power law distributions [e.g. Smith and Phoenix, 1981; Phoenix and Smith, 1983] and uniform distributions [e.g. Krajcinovic, 1979; Krajcinovic and Silva, 1982; Fanella and Krajcinovic, 1985] have also been used.

It seems that the selection of a strength distribution is somehow arbitrary, and that it is usually made strictly on empirical grounds. The Weibull distribution is

based on fitting of empirical data, and the theoretical appeal of the normal and lognormal distributions is given by the central limit theorem: both the normal and the lognormal distributions appear as a limiting distribution for the sum and product respectively of an infinite series of independent and identically distributed (IID) random variables.

Other attempts have been made to justify the choice of the PDF for the strength. For most materials a monotonically increasing failure rate is observed at sufficiently high load levels. The failure rate of a material subject to a load s is defined as the conditional failure probability at this load s, given that failure has not occurred at load levels less than s [Martz and Waller, 1982].

If the individual bar strengths in a weakest-link system are assumed independent, Bizup and Singpurwalla (1996) show that the PDF of the individual bar strengths is equal to the failure rate of the macroscale strength. Their result implies that the system failure rate cannot be monotonically increasing if a unimodal PDF is chosen for the individual bar strength. Since most commonly used PDFs, such as the normal, the lognormal, or the Weibull distribution, are unimodal, the system failure rate cannot be monotonically increasing if the individual bar strengths are independent random variables.

In short, both unimodal individual bar strengths and monotonically increasing system failure rates are supported by experimental evidence. It must then be concluded that the independence assumption of individual bar strengths leads to an incoherence.

2.3.7 Conclusions

The following conclusions can be drawn from the review of one-dimensional systems:

- The choice of mesostructure for a given material has important consequences for the macroscale structural behavior of the material. As an example, the chain-of-bundles system is much more brittle than the parallel bar model.
- The local load sharing rules also affect the macro strength of the material.
- The form of the PDF for the strength of one bar element has a major influence on the macroscopic behavior and it must be selected carefully.
- When the correlation between the strengths of the different elements in the micromodel is not accounted for, a deterministic constitutive behavior is obtained for continua.

2.4 Multi-Dimensional Models with Regular Geometry

2.4.1 Introduction

Two classes of multi-dimensional systems are reviewed:

- network or lattice model
- discrete particle model

A lattice model (Figure 2.10a) consists of straight elements, or links, which are connected to each other at the nodes. When all elements are pin-jointed at the nodes, a truss system is obtained and the elements (trusses) are subject to axial loading

only [Gasparini et al., 1995]. Frame networks have been studied as well and in that case the links are modeled as beam elements [Schlangen, 1993].

In a discrete particle model (Figure 2.10b), both displacements and rotations of the particles are allowed, as well as contact making and detachment of the individual particles [Cundall and Hart, 1992]. The particles are also referred to as bodies or elements. Although these models can be extended to three dimensions without major difficulty, they are usually restricted to 2D applications for practical reasons such as proper visualization of the results.

For lattice models the global deformation is applied incrementally and in every load step the broken links are removed from the model and excluded from the subsequent analysis steps [see Herrmann and Roux, 1990; Ostoja-Starzewski and Lee, 1996]. An example of intermediate crack states in a lattice model is shown in Figure 2.11. The damage is defined as the ratio of broken elements per volume unit. In every analysis step the stiffness matrix must be recalculated [Schlangen and Van Mier, 1992]. The removal of the failed elements has important consequences for non-proportional loading histories or stress reversals: "crack closure" cannot be modeled. Consequently, this model is essentially limited to applications with monotonically increasing loads.

This limitation is overcome when a particle model (Figure 2.10b) is used. Similarly to the analysis of a lattice model, the stiffness matrix of the discrete particle assembly is recomputed in every load step. The main difference with the network models is that the contacts between all particles must be checked prior to the stiffness matrix computation in every load step [Cundall and Strack, 1979]. Force transfer between two particles can happen only if they make contact. Consequently, crack

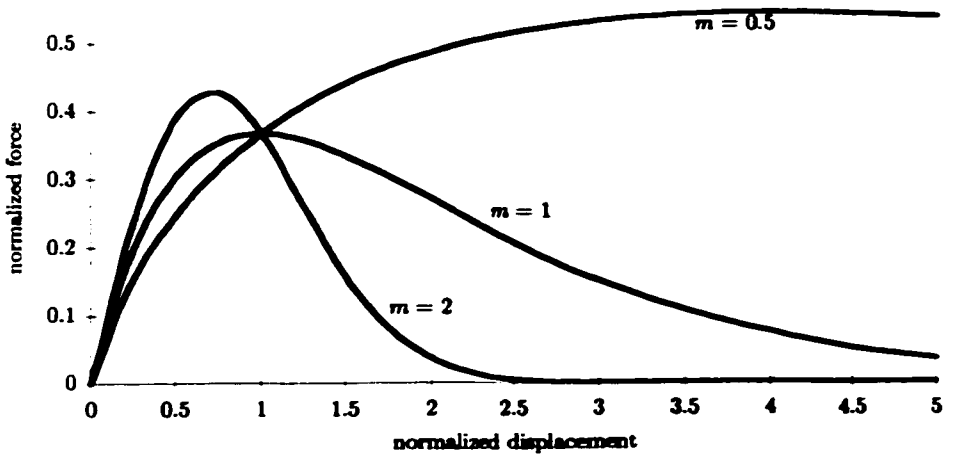

Figure 2.9: Force-displacement curves for different values of the shape factor m in the Weibull strength distribution

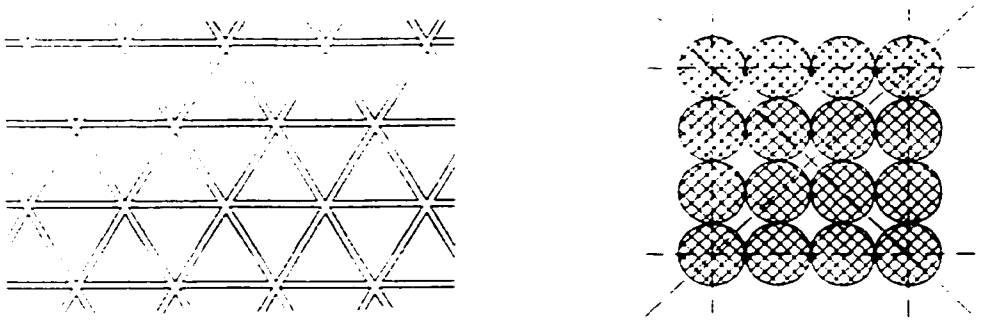

Figure 2.10: Regular triangular lattice model and circular disk particle model, corresponding to a square lattice model

closure can be simulated easily. This advantage comes at the expense of a longer computation time.

2.4.2 Topological Characteristics

A topology defines which types of mechanical interactions are possible between the different elements in the microstructure. A spring network has a different topology than a frame network. The former accounts for axial deformations only, while the latter can also take shear, bending and twisting effects into account.

The topology of a microstructure also describes the scale– and geometry-independent characteristics of the particle shape with respect to the mechanical behavior. A rounder particle tends to roll easier than a particle with just a few sides, for which friction with other particles becomes a more important interaction mechanism than rolling. For a triangular particle, for instance, friction will be more important than for a octagonal particle, which will roll easier than the triangular one.

A discrete system can never be perfectly isotropic or homogeneous. However, since a system whose size is larger than the RVE of the material can be assumed homogeneous, consistency between the deformation characteristics of a discrete system and its continuum equivalent is required.

To be consistent with the homogeneity assumption, Jirásek and Bažant (1995) state that the elastic strain energy in the deformed lattice should equal the strain energy stored in a continuum of the same size and shape. Hrennikoff (1941) was the first to prove that this equality condition can be satisfied only for certain values of the Poisson's ratio of the continuum. Macroscopically isotropic planar truss models have a "Poisson's ratio" of 1/3, for 3D truss models this value is equal to 1/4. The

value 1/3 is approximately correct for ice and metals, but is too high for concrete, which usually has a Poisson's ratio between 0.13 and 0.18. It can be shown that the Poisson effect cannot be simulated properly because only axial deformation of the elements is taken into account in this model.

The above is a fairly general result independent of the lattice geometry [Hrennikoff, 1941]. When only axial deformation of the elements is taken into account, all regular mesh types (triangular, square, hexagonal) will result in the same Poisson's ratio. Consequently, lattice and discrete particle models can correctly model the Poisson effect for other values only if the shear interaction and rotation of the constituent bodies is accounted for. For the lattice models, the "apparent" Poisson's ratio can be adjusted if the links are modeled as beams with variable height (2D) or tubes with variable thickness (3D) [Vervuurt et al., 1996].

A thorough study of the random nature of the elastic properties of triangular networks is done by Ostoja-Starzewski and Wang (1989). They show that the spatial randomness in the microstructure, i.e. deviations from the regular periodic geometry, has more impact on the macroscale properties than the variability of the micro-level strength and stiffness parameters has. The RVE of the continuum approximation may be considered a square cell, cut out of the total microstructure (Figure 2.12). The size of this cell must be large enough to allow for a homogenization, i.e. larger than the RVE. The mechanical properties of the continuum approximation are then local averages over this moving window and can as such be represented by a random field. Because the correlation structure of regular networks is substantially different from the one in random lattices, Ostoja-Starzewski and Wang (1989) suggest that regular networks may have only a limited applicability in the characterization of

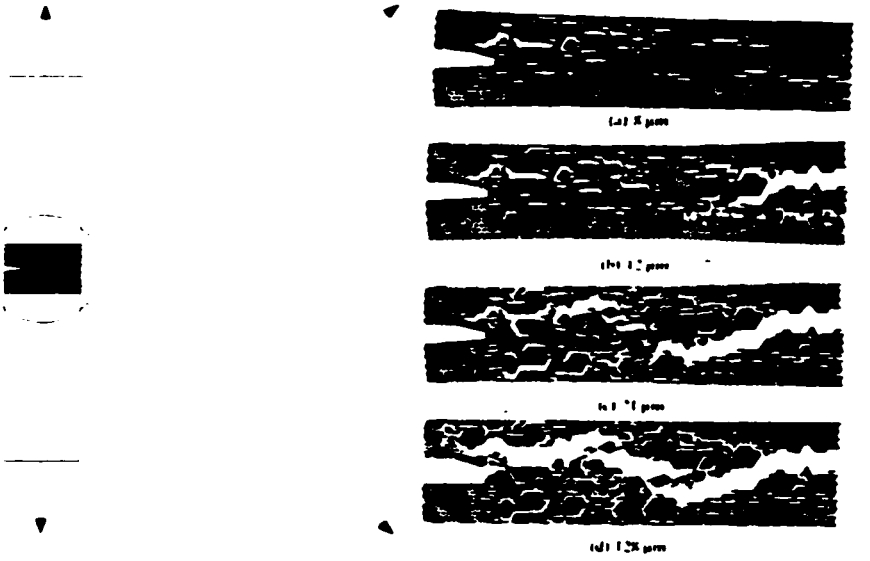

Figure 2.11: Crack states corresponding to increasing deformation levels in a lattice model simulation of a single edge notched (SEN) concrete specimen subject to uniaxial tension [Schlangen, 1993]

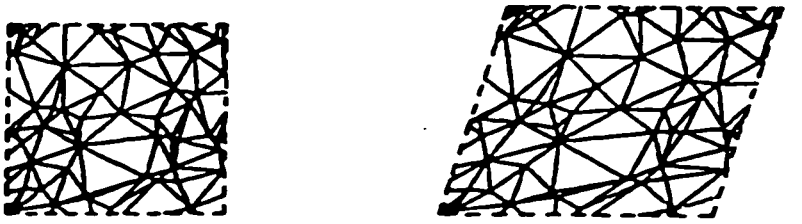

Figure 2.12: RVE window cut out from a triangular lattice model and subjected to a deformation [Ostoja-Starzewski and Wang, 1989]

actual materials.

In addition, Schlangen (1993) reports that the macroscale structural behavior of concrete specimens subject to uniaxial tension or bending obtained by simulation is too brittle compared with experimental evidence when regular triangular meshes are used. He uses a linear elastic-brittle constitutive law with random link strength. This could be one of the reasons why Jirásek and Bažant (1995) include softening behavior in the microscale constitutive law.

2.4.3 Anisotropy

Anisotropy in a macroscopically homogeneous material is caused by the microstructure. In the case of carbon fibers this is explained in Figure 2.13a. The molecular structure is planar hexagonal. The van der Waals forces, acting between the planes, are much weaker than the covalent carbon bonds acting in the plane. The forces may differ by several orders of magnitude and are the source of extreme anisotropy in graphitic fibers [Christensen, 1994].

Ideal ordinary ice (I_h) also has a hexagonal structure (Figure 2.13b), and this leads to the existence of preferred failure planes in the material across the hydrogen bonds. However, because of the presence of numerous point (inclusions) and line (dislocations) defects, this pattern is disturbed and a sufficiently large sample of randomly oriented ice crystals may become macroscopically isotropic [Eranti and Lee, 1986].

On the other hand, a lattice model with a regular geometry is "defect-free" and strong mesh-induced directional bias seems to be inevitable. In their study of the collision of a circular ice floe with a circular obstacle, Jirásek and Bažant (1995)

observed strong asymmetry in the failure patterns depending on the approach angle, i.e. the angle between the principal lattice axis and the impact direction. Moreover, the bias persists even if the strength of the links is randomized. They used square meshes in their analysis and suggest that the mesh-induced bias may be even higher when triangular meshes are used.

Several authors report another problem associated with the existence of preferred directions in models with regular geometry. Rossi and Richer (1987), Schlangen (1993), and Rossi et al. (1996) report that the crack pattern of concrete specimens tends to follow the principal axes of the mesh. As a result, this crack pattern will mainly consist of straight lines when a regular mesh geometry is used. Consequently, lattice or particle models with regular geometry may not be the most appropriate for macroscopically isotropic materials with anisotropic microstructure.

2.4.4 Consistency of Discrete Models

Breysse et al. (1994) studied the effect of the micro-failure criterion on the macroscopic failure of networks with regular geometry and random Young's modulus. The micro-constitutive law was elastic-brittle and three micro-failure criteria were studied. The first one was stress based: a microstructural element fails if its stress exceeds a specified level. The second and third failure criterion are strain-based and energy-based.

Since the element stiffness is considered random in this study, a different element will fail first for each of these three micro-failure criteria. In the case of a stress-based microfailure criterion, the stiffer elements will fail first, which is different for a strain based criterion. It follows that the non-linear response of the network is intrinsically

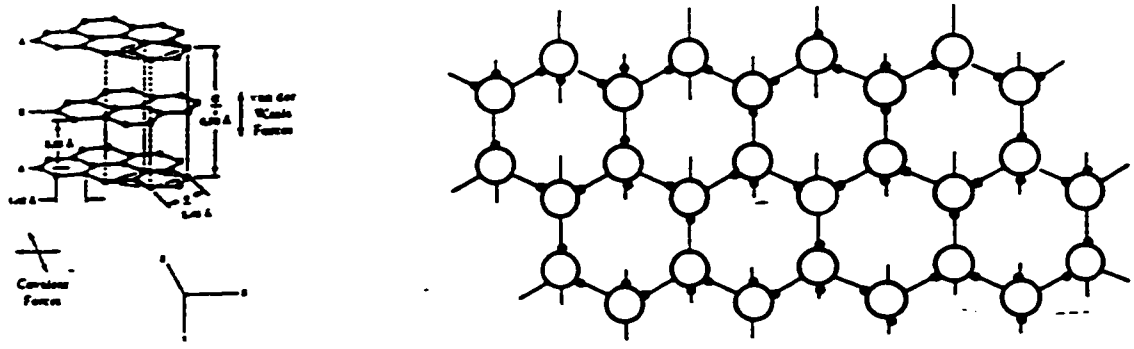

Figure 2.13: Molecular structure in a carbon fiber [Christensen, 1994] and in ice [Petrenko and Whitworth, 1994]

Model Type	*Slope*
Parallel Bar	1/3
Series System	-1/3
Triangular	1/3
Hexagonal	-1/3
Square	0
Cubic (3D)	1/2

Table 2.1: Correlation between energy and Young's modulus for various models [Breysse et al., 1994]

related to the failure criterion.

Breysse et al. (1994) also looked at the correlation between the deformation energy and the average Young's modulus in the lattice model. They plotted the elastic energy stored in a link as a function of its Young's modulus and observed an almost linear relationship. The slope of this line depends on the lattice geometry and it is given in Table 2.1. This relation becomes important when an energy-based failure criterion is used. In a parallel bar model the stiffer elements will fail first, while in the series system the more compliant elements will fail first. Most models discussed so far use a stress or strain-based failure criterion, but an energy based criterion was developed for concrete in Yip (1996).

2.4.5 Conclusions

This review of discrete models with regular geometry highlights some important characteristics:

- Multiaxial loading conditions cannot be described adequately when only the axial deformation of the elements is accounted for.
- Defects in the microstructure introduce randomness in the macroscopic behavior which cannot be accounted for using regular geometry.
- When the material inhomogeneities are accounted for, stress and strain based microlevel failure criteria are no longer equivalent.

2.5 Multi-Dimensional Models with Random Geometry

2.5.1 Introduction

Discrete element models can be used to describe the material as an assembly of microscale constituents. Such models can be applied to soil or concrete, which are often treated as continuous even though they consist of discrete grains at a microscopic level.

The bodies in a discrete element model (Figure 2.10b) are allowed to move and rotate, as well as to make or break contact with each other. Cundall and Strack (1979) initially modeled granular soil as a two-dimensional assembly of circular elements. Since then, the discrete element methods have come a long way. Here, only a brief overview is given, based on the three most important aspects of discrete elements: representation of contacts, representation of solid constituents and the scheme used to detect and revise the set of contacts [Cundall and Hart, 1992].

Subsequently, two different topological families will be presented. The first family mainly applies to crystal aggregates while the second one provides a better description for granular materials. In the last section, lattice models with random geometry are discussed.

2.5.2 Representation of the Contacts

In a discrete model the contacts between the constituents can open, close and slide. They can be modeled as either soft or hard [Cundall and Hart, 1992]:

- Soft contacts model the surface deformation when two bodies make contact. The axial stiffness may be assumed constant or dependent on the relative dis-

placements of the particles in contact [e.g. Zubelewicz and Bažant, 1987; Bažant et al., 1990; Dobry and Ng, 1992]. It is assumed that there is no actual physical penetration of the particles: their relative displacement can be imagined as the deformation of interface layers around the rigid particles, which themselves are considered indeformable.

- When hard contacts are used no deformation of the particles is possible at all. They are mostly used in studies of sparse populations of bodies [Loset, 1994a], usually moving around at fairly high speeds. Their collisions are very brief and modeled by exchange of momentum.

As a general rule, physics should guide the choice of contact assumption. The assumption of hard contacts may seem the only reasonable one at first, but an interface layer may be physically present in a lot of materials. This is for instance the case in normal strength concrete (NSC) where the rigid granulates are imbedded in a softer matrix. Soft contact conditions also apply when crushing occurs in the formation of ice rubble. The crushing of an ice floe broken by a boom is described in Loset (1994b).

To model progressive failure adequately, sliding of contacts should be incorporated as well. Damage accumulation can occur under a variety of stress and strain conditions and is not restricted to tensile conditions only. Damage growth in concrete for instance is a combination of tensile and shearing failure modes (Figure 2.14). Inclusion of shear interactions also leads to a more realistic description of the Poisson effect and thus a wider range of possible Poisson's ratio values [Zubelewicz and Bažant, 1987].

2.5.3 Representation of the Solid Constituents

The discrete particles in the microstructure may be assumed rigid or deformable. The assumption of deformable contacts and rigid particles is appropriate if most of the deformation is accounted for by movement of discontinuities. This is the case for NSC, and unconfined assemblies of rock or soil at low stress levels.

When the deformation of the constituent particles cannot be neglected, this deformability can be introduced directly by dividing every discrete particle into finite or boundary elements [De Schutter and Taerwe, 1993]. Another method which may be convenient for complex particle shapes is the expansion of their deformation in terms of orthogonal deformation modes [Cundall and Hart, 1992]. These deformation modes are then combined using the superposition principle. This implies that this method can only be used iteratively when material non-linearity is involved.

2.5.4 Detection and Revision of the Contacts

The straightforward approach is to check every particle against every other one to determine whether contact has occurred or diappeared. This brute force approach is unacceptable for a large number of particles (n), since the computation time is proportional to n^2 [Cundall and Hart, 1992]. The cost can be reduced considerably by efficient bookkeeping techniques. At the start one exhaustive n^2-type search is done, and for every particle a list of its "neighbors" and "friends" is set up. A "neighbor" makes contact with the particle, and a "friend" is a particle in its nearby vicinity. During the subsequent time or iteration steps, only the neighbors have to be checked for contact-breaking, and the friends for possible contact-making. This effectively reduces the order of computational complexity to n [van Baars, 1996].

2.5.5 Crystal Topology

General

The topology of crystalline microstructures depends on the conditions occurring during the formation of the material. Consider, for instance, the formation of ice. Crystals start to form at discrete points, referred to as nucleation sites, and then grow in time. Depending on the nucleation conditions and growth rates, different microstructures will emerge. Similarly, the topology of rock formations, metals and minerals also depends on the nucleation and growth conditions.

In 2D applications, the formation process of solid materials can be described mathematically using so-called area-generating processes. In these processes, the crystals (areas in 2D) grow starting from discrete points. These discrete points are referred to as nucleation sites and they must be generated first. The most widely used type of point-process for the generation of the nucleation sites is a Poisson process or a modification thereof [Getis and Boots, 1978].

Only space-exhaustive area-generating models are discussed here. In these models voids cannot occur; every point in the area or volume considered belongs to a sub-area or sub-volume, respectively. Spatial processes have applications in various fields such as mineralogy, biological sciences and metallurgy. They can also be used to describe the influence area of service facilities, such as Light Rail Transit stations or shopping malls, in urban centres [Getis and Boots, 1978].

First, the nucleation conditions are discussed and two limiting two-dimensional crystallization models are presented. Subsequently, modifications of these models and some of the differences between 2D and 3D modeling are discussed.

Nucleation of New Crystals

Nucleation may occur homogeneously or heterogeneously. Under homogeneous conditions, nucleation occurs at uniformly distributed random locations. Heterogenous conditions apply when nucleation is restricted to some preferred locations only. These preferred locations can be either point or line defects, such as inclusions, vacancies, micro-cracks, or dislocations. Even though heterogeneous nucleation conditions will usually prevail, the assumption of homogeneous nucleation may be a good approximation because the inclusions, vacancies or other defects themselves may be approximately uniformly distributed. Here, only homogeneous conditions will be discussed.

The Poisson process is the basic process for the development of most point pattern models and is characterized by the following assumptions [Getis and Boots, 1978]:

- points are placed in a region where every point location is equally likely to be chosen
- the points are located independently of each other

Mathematically, the Poisson process is characterized by a single parameter: the density λ. The average number of points in an area A is then λA (see Table 2.2).

Cell Model

Upon nucleation, the crystals start to grow in the material. In this model, the areas, which represent the crystals, are assumed to grow at the same rate in all directions, and the growth rate is also assumed constant in time. It is furthermore assumed that all nucleation occurs instantaneously before any of the crystals starts growing, no new crystals appear once the growth process has started. Consequently, the areas

will have a spherical shape as long as they do not make contact with any other area. Under these assumptions, a so-called "Voronoi polygon" structure results after saturation of the area (Figure 2.15). Under these assumptions the size of the polygons depends only on the nucleation density λ. The nucleation locations are referred to as the nodes of the "Voronoi polygons". The cell structure covering the area without gaps or overlaps by congruent plane figures is also referred to as a "tessellation" [Frost and Thompson, 1987].

Voronoi cells, also named Thiessen polygons, Wignes-Seitz cells, or Dirichlet regions, have the following characteristics [Getis and Boots, 1978]:

- all edges are straight lines
- all cells are convex
- they have at least three edges
- very point in a Voronoi cell is closer to its own node than to any other node in the area.

Some other characteristics are summarized in Table 2.2. Examples of this structure are found in the crystal structure of bronze and some stainless steels.

Johnson-Mehl Model

This is a generalization of the previous model which was originally developed in relation to the growth of crystal aggregates [Johnson and Mehl, 1939]. The nucleation is still homogeneous, but occurs no longer simultaneously at every node. It is also assumed that nucleation cannot occur within the already formed crystals, i.e. within

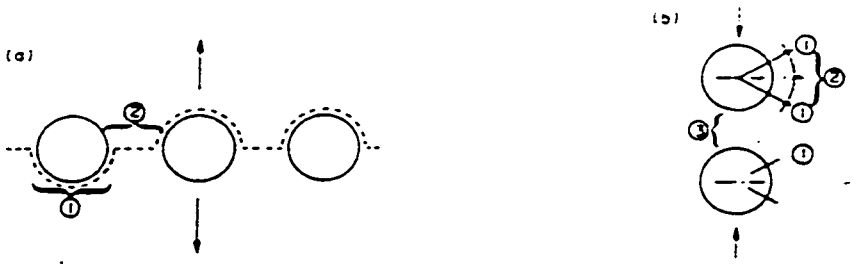

Fig. 1. Different phases of microscale damage in concrete. (a) ① Beginning of damage: microcracks grow around the grains in a mixed mode (I + II). ② Instability and rupture: microcracks grow inside the matrix in mode I and lead to the creation of macrocracks perpendicular to the direction of the load. (b) ① Beginning of damage: microcracks appear in mode II. ② Stable increase of damage: microcracks grow around the grain in mode I. ③ Instability and rupture: microcracks grow inside the matrix in a mixed mode (I + II) and lead to the creation of macrocracks parallel to the direction of the load.

Figure 2.14: Different phases of microscale damage in concrete [Mazars, 1986]

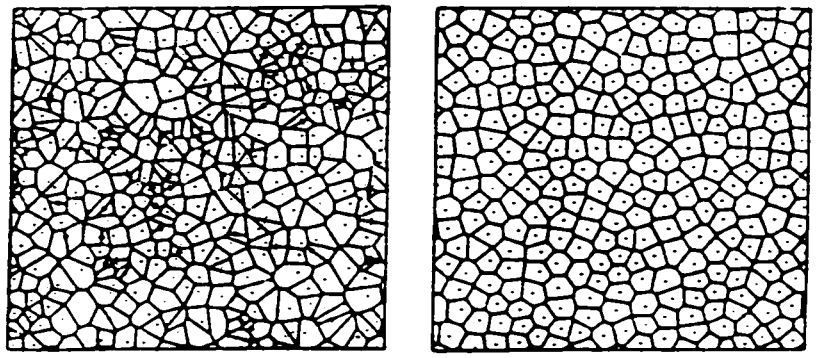

Figure 2.15: Voronoi polygon structure. [Gibson and Ashby, 1988]

Random Variable	*Expected Value*	*Variance*
Number of nodes in area A	λA	λA
Area of one cell	λ^{-1}	λ^{-2}
Number of sides per Voronoi cell	6	$\simeq 1.76$
Length of any edge	$\frac{2}{3\sqrt{\lambda}}$	$\simeq 0.126/\lambda$
Distance of node to nearest neighbor	$\left(2\sqrt{\lambda}\right)^{-1}$	$\simeq 0.075/\lambda$

Table 2.2: Some characteristics of the Voronoi-tessellation. λ is the density of the nodes $[m^{-2}]$

pre-existing areas. The nucleation rate may vary with time as well. As a result, the contact line separating two crystals, which nucleated at different times, is no longer straight. It can be proven [Frost and Thompson, 1987] that the contact line is now a hyperbola, with its focus on the side of the last nucleated crystal (Figure 2.16). This structure has been used to describe fractures in cooling rock [Smalley, 1966] and can also be found in ice [Sinha, 1991]. The major characteristics of the topology are [Getis and Boots, 1978]:

- both curvilinear and straight edges are possible
- cells not necessarily convex any more
- minimum number of edges is only two, which must be curved in that case

Comparison of the Cell and Johnson-Mehl Model

Depending on the values for the growth rate of the existing crystals and the nucleation rate of new crystals, the generated microstructures may be quite different. Frost and Thompson (1987) obtained the probability density functions (PDF) for some important topological characteristics by simulation. A comparison of these PDFs indicates some important differences between the cell and Johnson-Mehl models:

- Almost no triangles are obtained in the Voronoi tessellation, but quite a few grains with only three edges exist in the Johnson-Mehl model.
- The Johnson-Mehl model produces far more grains with small area than the cell model. The PDF for the grain area in the Johnson-Mehl model with a

constant nucleation rate is similar to an exponential distribution. For the cell model, a lognormal-like distribution is obtained.

- The average segment length in the Johnson-Mehl model is lower than for the Voronoi polygons. This is mainly due to the wider distribution for the number of sides per grain in the Johnson-Mehl model.

Extensions

For some materials no nucleation is possible close to an existing crystal. This nucleation-exclusion zone is called the depletion layer and surrounds the growing grains. Since the location of new nucleation sites, in this extended model, is no longer independent of the existing locations, the Poisson point process must be modified in the simulation model. Depending on the width of this depletion layer and the growth rate of the crystals, totally different micro-structures may be obtained. The microstructure, resulting from this modified Johnson-Mehl model, resembles more and more the structure of a cell model as the width of the depletion layer increases [Frost and Thompson, 1987].

Mahin et al. (1980) performed 3D-simulations of the Johnson-Mehl process with a constant nucleation rate. The area distribution for a planar section through the 3D model is similar to the 2D simulation result. For the cell model, however, a distinctly different area distribution is obtained for the 2D model and the planar section through a 3D model. In the 3D model, the area distribution has a sharp peak near zero [Mahin et al., 1980] which is absent in the planar model [Frost and Thompson, 1987].

2.5.6 Granular and Other Topologies

Particle Shape

For some materials, such as soil or concrete, a granular model is a physically more appropriate topology. For computational convenience, the circular disk or sphere is the most common particle shape. A shortcoming of the circular particle shape is that spherical grains tend to roll easier than grains of a more irregular shape. A compromise between modeling accuracy and computational cost may be found in ellipsoidal particle shapes. Studies have shown that elliptical grains fail at higher loads than circular grains [Rothenburg and Bathurst, 1992]. The effects of restricting the rotation of circular particles are studied in Ting et al. (1988).

Clay, along with some other cohesive soils, does not consist of circular or spherical particles. Clay particles resemble small plates and the bending and sliding of these platy elements represents an important deformation mechanism in the soil. This bending could be simulated by an assembly of beam elements. However, the complex, higher-order deformation pattern of beams leads to geometrical intractability. Anandarajah and Lu (1991) developed a model where every "beam" particle is actually a chain of 4 truss elements. The rotations at the hinges between the different truss elements then simulate the bending while the discrete elements themselves (the trusses) remain straight. This approximation greatly simplifies the calculations. The model has been applied to uniaxial compression of cohesive soil specimens where both mechanical and physico-chemical forces are taken into account [Anandarajah, 1995].

Meshing

For mesh generation different techniques can be used. It is important to understand that a 2D-section of a 3D-structure will contain more small particles in the cross-section than expected from the sieving grade curve of the material [Walraven, 1980]. This means that the stiffness will be overestimated because more "hard material" is present in the 2D model. Possible "meshing" strategies include:

- Take and Place Method [Bažant et al., 1990]

  Starting with the largest grains in the distribution, generate a random position (from a uniform distribution) for every particle and put it in place if it does not intersect with specimen boundaries or other particles. Otherwise the particle is rejected and a new random trial position is generated. The smaller particles are put in place only once all the large particles have been placed. The method is computationally workable only for simple particle geometries, such as circles or ellipses. Since this rejection algorithm becomes increasingly more inefficient as more particles are put in place, modifications to this basic algorithm must be implemented. Two approaches are quite common:

  - using a search algorithm, the particle is moved around until an open spot is found
  - the uniform distribution is modified as a function of the positions already occupied

- Divide and Fill Method [De Schutter and Taerwe, 1993]

  First, a set of points is distributed over the area following a Poisson point

process and a Delaunay triangulation is used to divide the specimen into n volumes (n is the number of particles in the model). The Delaunay triangulation is the dual graph of the Voronoi tessellation and connects the nodes of adjacent Voronoi cells. In a second step, each of these volumes is replaced by a particle, which must fit entirely within the cell boundaries. This particle could be the inscribed sphere, but smaller particles are allowed to obtain a better agreement with the sieving grade curve. Non-spherical particles can be used as well.

A restriction of this method is that it cannot simulate high packing densities. Since the inscribed circle covers about half the area of a triangle, packing densities of near or over 50% cannot be achieved [De Schutter and Taerwe, 1993].

In all of these methods most particles are not in contact with each other, but separated by an interface zone. This makes it possible to model interaction between particles that are not in direct physical contact. All particles (radius r) are assumed to be surrounded by an influence zone with radius βr. When the influence zones of two particles overlap, the particles are assumed to interact. Originally, a value $\beta = 1.2$ [Zubelewicz and Bažant, 1987] has been suggested, but this was later revised upwards to $\beta = 1.65$ [Bažant et al., 1990] and even $\beta = 2$ [Jirásek and Bažant, 1995]. The method was applied to both concrete and ice.

Different algorithms can be used when denser packings, in which most of the particles are making contact, have to be obtained (see Dobry and Ng (1992) for further references).

2.5.7 Lattice Models with Random Geometry

For monotonic loading conditions, where (micro)crack closure is far less important than for cyclic loading, a lattice model with random geometry may be very well suited to analyze the progressive cracking in a structure. The use of random networks to simulate the progressive failure of heterogeneous materials was first studied by Burt and Dougill (1977).

In this model the material is modeled as a planar truss system (Figure 2.17) in which n nodes are uniformly randomly distributed over the area. Out of the $n(n-1)$ possible truss members a random selection is made which satisfies requirements on the maximum length of a member and the overall member density. The micro-constitutive law is uniaxial elastic-brittle and, since the model is used to simulate tension softening, compressive failure of the trusses is not considered. In the model, both the member stiffnesses and strengths are IID variables, drawn from a normal distribution truncated at zero. It is essential to understand that this model does not attempt to represent the actual structure in the material, it is only a phenomenological description of the macroscopically observed behavior.

A typical stress-strain curve resulting from this model is given in Figure 2.17. The scatter on these results is indicated as well. Repeated simulations indicate only a very small difference between models with random and deterministic material properties for the initial load stages, even though a slight increase in initial stiffness is observed when all links have identical stiffnesses. It can also be concluded from Burt and Dougill's (1977) simulations that decreasing the heterogeneity of the material mainly increases the peak stress and leads to a steeper descending branch of the

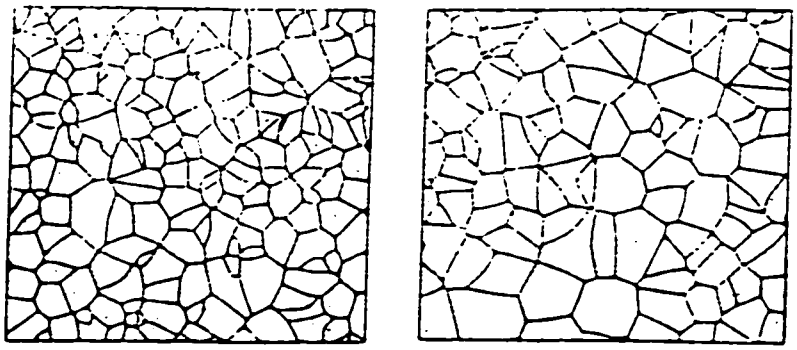

Figure 2.16: Johnson-Mehl structure for a slow (left) and fast growth rate (right)

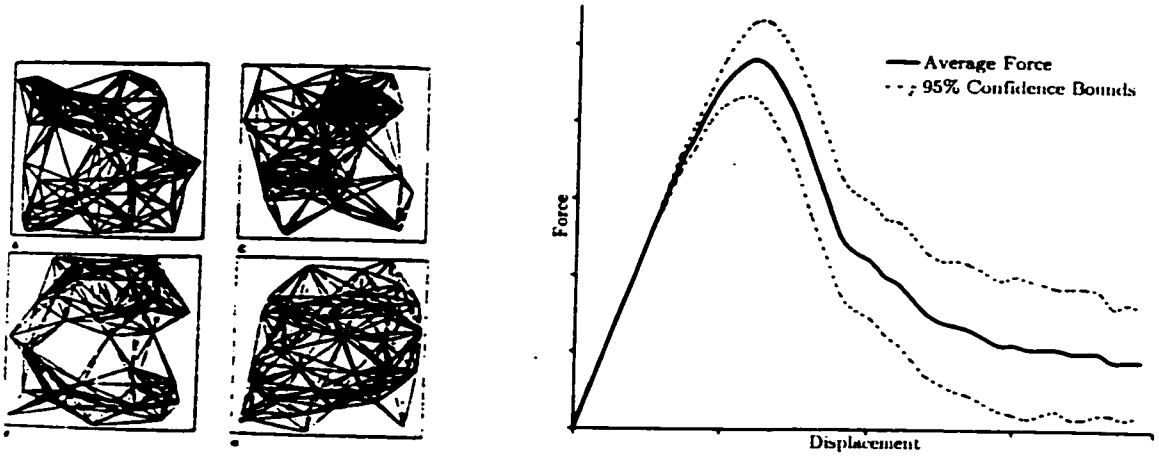

Figure 2.17: Typical random network and force-displacement curves

force-displacement curve. The scatter is considerably higher in the post-peak region. This seems logical: the more members that fail, the higher the scatter becomes.

In this model members seem to fail in local groupings. As such, strain localization is simulated adequately. Because the heterogeneity of the material is modeled, size effects are obtained automatically: smaller samples have a higher mean peak stress and a higher standard deviation than larger samples.

The meshing technique used in this model seems rather *ad hoc* and actually causes two major shortcomings in the model:

- the crossing of the truss members (Figure 2.17) makes visualization of the fracturing process extremely difficult
- the model is anisotropic unless prohibitively large amounts of nodes and members are generated

These drawbacks can be overcome when adequate meshing techniques are used. One possibility is to make use of the so-called "Delaunay triangulation" [Gasparini et al., 1996], which is the dual graph of the Voronoi tessellation [Ostoja-Starzewski and Wang, 1989]. Its generation is very similar to the generation of a Voronoi cell pattern. First, a field of nodes must be generated. Similarly to the Voronoi cell pattern, a homogeneous Poisson point process is the most popular choice for this. Subsequently, every node is connected with its three nearest neighbors.

An alternative simulation scheme, which does not start from a homogeneous Poisson point process, is suggested by Moukarzel and Herrmann (1992) and is implemented in Schlangen (1993), Van Mier et al. (1996), and Vervuurt et al. (1996). It is conceptually similar to the depletion layer used in the cell model, discussed in

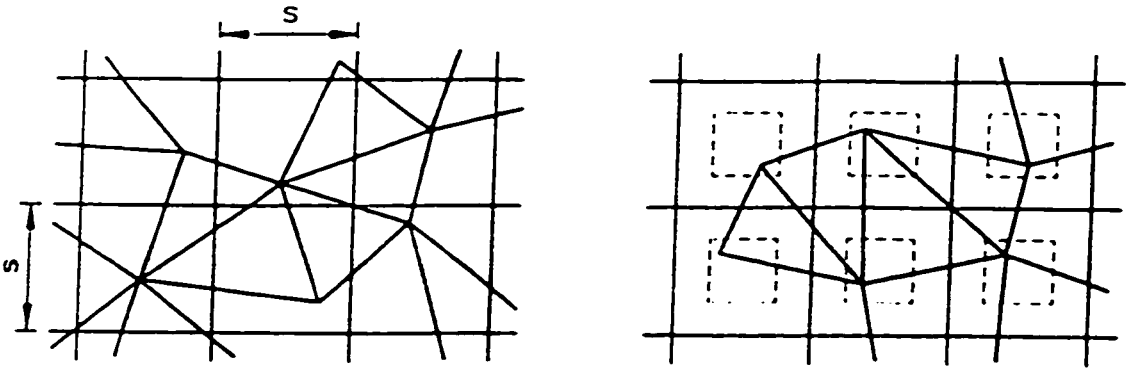

Figure 2.18: Variation of randomness in the lattice by restricting the position of the nodes to a sub-area of the original cells [Schlangen, 1993]

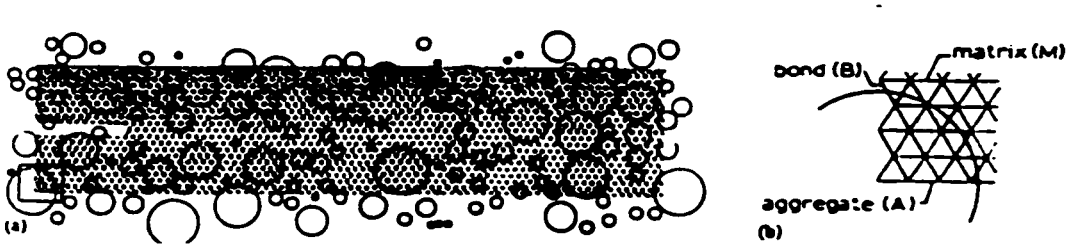

Figure 2.19: Projection of lattice on grain structure and definition of beam materials [Schlangen, 1993]

Section 2.5.5, in the sense that the nodes cannot be located in some areas. First, a square mesh is defined in the material. In a second step one point is selected randomly in every mesh cell and a triangulation is constructed by connecting the three points which are closest to each other. The degree of randomness in this lattice can be controlled in the second step by restricting the random selection of a node to a sub-area of the cell rather than the entire cell area (see Figure 2.18). The ratio of the size of this sub-area and the entire cell is a measure for the degree of randomness. In the limit case of zero randomness, a regular, square lattice will be obtained [Schlangen, 1993].

Unlike the previous lattices, this model tries to represent the actual material structure. For this purpose, the maximum member length must be at least three times smaller than the smallest grain size [see Schlangen and Van Mier, 1992; Vervuurt et al., 1996]. The triangular lattice is now projected on top of the generated grain structure (Figure 2.19) and different strengths and stiffnesses are assigned to the respective elements. This is illustrated for concrete in Figure 2.19 where three material zones are used. Details of an application to sandstone are reported in Vervuurt et al. (1996). If randomized, the strength of the members is assumed to be normally IID in this model.

One of the reasons for the high detail of the model is that it is used to simulate crack face bridging. It is known that this is associated with rotation of the material [Bascoul, 1996]. Since this rotation cannot be described accurately using axial deformations only, beam elements are used instead of trusses.

2.6 Modified Continuum Models

2.6.1 Introduction

In the introductory chapter, it was stated that a material can be modeled as either a continuum or as a discrete system. Classical continuum mechanics methods fall short whenever the heterogeneities in the material seriously affect the stress distribution in the material. However, some classical methods can be modified successfully to account for the effects of material heterogeneity and the resulting variability in the structural response of the material. This is explained in the following.

2.6.2 Material Heterogeneity

A descriptive, macroscale continuum theory assumes the material to be homogeneous. If the structural scale is not "infinitely" larger than the size of the RVE, but of comparable size, the stresses and strains resulting from a classical continuum approach can still be interpreted as "average" values but they may be physically meaningless because of the heterogeneity in the material. In other words, the influence the internal disorder in the material has on the stress gradients could be of at least the same order as the influence of the external loading [Breysse et al., 1994].

So-called non-local methods, where the continuum stress in a point no longer depends solely on the strain in that point, but on a strain distribution in the local neighborhood, have proven a successful modification of the classical continuum methods for the analysis of structures exhibiting strain softening behavior. In those cases, the use of non-local techniques eliminates the mesh dependency of the results. Various local averaging schemes that have been proposed [Pijaudier-Cabot

and Bažant, 1987].

Another possible solution may be to calculate the macro stiffness directly from the actual micro-structure. An example of this approach in a finite element context for linear elastic analysis is given in Liao and Chang (1992). The element stiffness matrix is calculated from the virtual work due to rotation at the contacts and displacement of the circular particles within the element domain. The method significantly reduces the number of degrees of freedom, but can only be used in the small strain range. Damage growth can not be accounted for.

Breysse (1990) suggested a micro-macro probabilistic analysis method, which can account for damage accumulation. The constitutive model for the elements, which are used in the finite element mesh is given by the macroscopic response of a parallel bar system. The micro-constitutive law is linear elastic-brittle and the damage is obtained as the ratio of broken bars. The strengths of the individual bars are assumed independent and identically Weibull distributed. As such the model can be considered a finite element method where every finite element is in itself a probabilistic parallel bar model.

2.6.3 Response Variability

Material parameter variation is not necessarily a white-noise process, which means that the value of a material parameter at one point is not totally independent from its values in the neighborhood. The spatial correlation structure of material characteristics must be accounted for properly in a random field description. This is clear from a comparison of the results obtained in the parallel bar models by Krajcinovic and Silva (1982) and Kandarpa et al. (1996). Assuming statistical independence

of the bar strength leads to a deterministic result for the damage evolution in the continuum approximation, while accounting for the correlation maintains (random) variability in the model response.

In the stochastic finite element method, these random fields are discretized into random variables. An optimal discretization affects the meshing [Zhang, 1994]. If not done properly, the meshing may introduce substantial error in the finite element calculations. Recently, a lot of progress has been made in the field of discretization [Schuëller, 1997], but the selection of the underlying random field remains to a large extent arbitrary. Quite often a Gaussian field is chosen simply because of its computational convenience.

Another aspect associated with the arbitrariness in the selection of random fields and the implications this choice has on the results obtained from stochastic finite element models, is discussed by Ditlevsen and Tarp-Johansen (1996). In particular, Ditlevsen and Tarp-Johansen (1996) discuss whether it is better to use a stiffness field or its reciprocal field, the flexibility field, as the input of a stochastic finite element model. This seems to be important, especially for non-Gaussian random fields, because of the additional model error introduced by the discretization of the random field.

A possible method to determine the characteristics of random fields is presented in Ostoja-Starzewski and Wang (1989), Ostoja-Starzewski and Wang (1990), Mirfendereski and Der Kiureghian (1994), Ostoja-Starzewski (1994a) and Ostoja-Starzewski (1994b), and was already discussed in Section 2.4.2 in the case of a lattice model. The method can also be applied to cellular microstructures and matrix-inclusion models, where inert phases are embedded in a homogeneous matrix (see Figure 2.20).

Matrix-inclusion models are quite commonly used in the field of composite materials, as a technique to account for the effects of material heterogeneity [Nemat-Nasser and Hori, 1993]. In Ostoja-Starzewski's (1994b) approach, the derivation of the random field characteristics is based directly on the microstructure. An important conclusion is that the random field characteristics may depend on the finite element mesh size. However, the method is still under development.

2.7 Summary

In this chapter, some of the difficulties associated with constitutive modeling, accounting for the material heterogeneities, are discussed. Both discrete and continuum methods are reviewed. Tables 2.3 and 2.4 form the basis for a classification of every discrete model. Important criteria for the design of a discrete model are:

- The choice of microstructure for a given material has important consequences for the macroscale structural behavior of the material. As an example, the chain-of-bundles system is much more brittle than the parallel bar model.
- The local load sharing rules affect the macro strength of the material.
- The form of the PDF for the strength of one bar element has a major influence on the macroscopic behavior and it must be selected carefully.
- When the correlation between the strengths of the different elements in the micromodel is not accounted for, a deterministic constitutive behavior is obtained for continua.

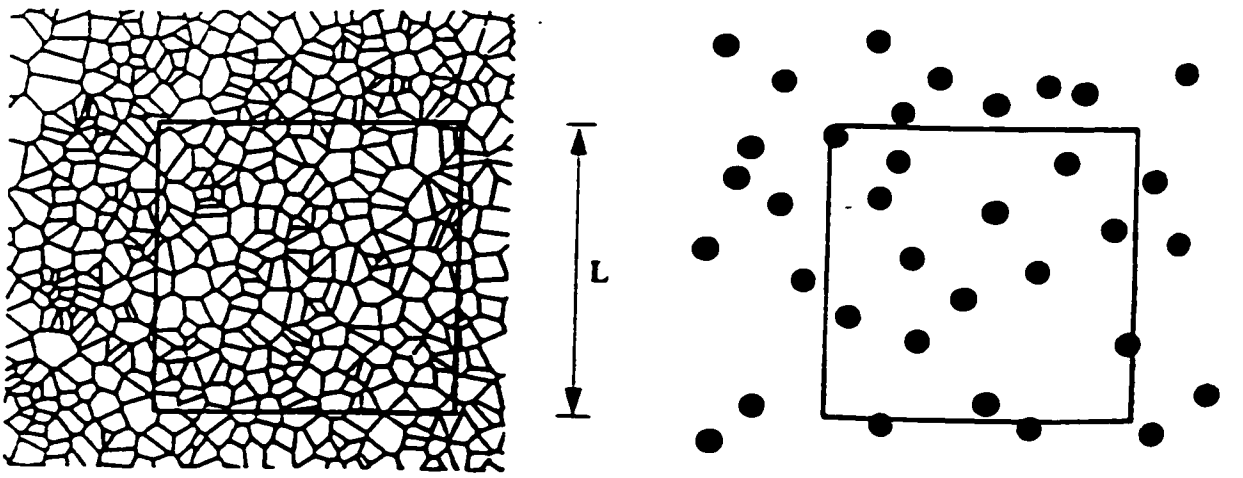

Figure 2.20: A window in the microstructure of a Voronoi tessellation and a matrix-inclusion composite [Ostoja-Starzewski, 1994]

Criterion	*Sub-categories*		
Dimensions	2D	3D	
Lattice Shape	regular	random	
Member Type	uniaxial	axial+shear	axial+bending
Constitutive Law	elastic-brittle	softening included	
Problem Type	uniaxial tension	shear	bending

Table 2.3: Classification of lattice models

Criterion	*Sub-categories*	
Dimensions	2D	3D
Contact Law	Soft	Hard
Solid Material	Deformable	Indeformable
Topology	Crystalline	Granular

Table 2.4: Classification of particle models

- Multiaxial loading conditions cannot be described adequately when only the axial deformation of the elements is accounted for.
- Defects in the microstructure introduce randomness in the macroscopic behavior which cannot be accounted for using regular geometry.
- When the material inhomogeneities are accounted for, stress and strain based microlevel failure criteria are no longer equivalent.
- The topological characteristics, such as the roundness of elements, of crystalline topologies largely depend on the nucleation conditions.
- Idealized modeling of granular material using circular or spherical elements leads to an overestimation of the grain rotation.
- The topology of a planar system may differ considerably from the topology in a 2D section of a 3D microstructure.

Chapter 3

Parallel Bar Model for Linear Elastic-Brittle Materials Subject to Uniaxial Loads

3.1 Introduction

In the previous chapter, the merits and shortcomings of models with regular geometry were outlined. It was explained that, because of the existence of preferred directions in a regular microstructure, models with regular geometry may not accurately reflect the variability in the structural behavior of real materials. Nonetheless, a detailed study of micro-mechanical models with simple geometries may provide additional insight about the interactions between the constituents at the micro-level and the impact they have on the macroscopic structural behavior.

In this chapter the progressive failure of parallel bar systems, which are subject to axial deformations only, will be studied. The parallel bar model has been used by other authors [e.g. Daniels, 1945; Burt and Dougill, 1977; Krajcinovic and Silva, 1982; Gasparini et al., 1995; Kandarpa et al., 1996] to analyze the force-displacement behavior of brittle materials under compressive or tensile loading. In this dissertation, the model is also extended to include the study of the moment-curvature relationship of linear elastic brittle beams.

The goal of this chapter is to demonstrate how the macroscopic structural behavior follows from the interactions between the constituents at the micro-level. The

analysis will demonstrate the capabilities and limitations of 1D micro-mechanical models.

3.2 Model Description

3.2.1 General

Uniaxial stress states can be modeled using a parallel bar model [Daniels, 1945]. The individual bars or springs (see Figure 2.4) are considered to be representative of the micro-properties of the material while the system as a whole describes the macroscopic behavior. By assuming simple force-displacement behavior for the individual springs, complex macroscopic behavior can be described.

Consider the continuum model of the homogeneous beam of length ℓ with rectangular cross-section A in Figure 3.1a. The beam is subject to normal stresses only, which are perpendicular to the cross-sectional plane and are caused either by an axial load P or by a pure bending moment M. No shear stresses are acting on the beam. The beam is divided into n equal horizontal layers. Since only axial forces act upon each of these layers, they can be modeled as springs as shown in Figure 3.1b.

The following micro-mechanical constitutive law is adopted. A linear elastic-brittle force displacement behavior is assumed for each of the springs. All spring stiffnesses are assumed to have the same, deterministic stiffness k. Compressive failure is excluded from the model. A spring i will fail in tension when the strain in the spring ε_i exceeds the failure strain $\varepsilon_{i,max}$, which is considered a random variable. This failure strain $\varepsilon_{i,max}$ is generally not identical for all springs. The failure strains can be modeled as either independent, identically distributed (IID) random variables

or as a random field. The ensemble of failure strains $\varepsilon_{i,max}, i = 1 \ldots n$, defines a one-dimensional discrete random field. In the limit for $n \rightarrow \infty$ this discrete process becomes a continuous 1D random field when h remains constant, i.e. the spring become infinitesimally close to each other.

The objective of the analysis is to identify the sensitivity of the macroscopic response to different assumptions for the material model at the microscale. Various types of probability distributions and correlation functions will be considered for $\varepsilon_{i,max}$.

3.2.2 Damage Accumulation

In this model any micro-spring fails when the strain ε_i in this spring i exceeds the failure strain $\varepsilon_{i,max}$ of this spring, which is considered random. The force F_i in spring i of the micro-mechanical model is:

$$F_i = \begin{cases} k\ell\varepsilon_i & \text{if } \varepsilon_i \leq \varepsilon_{i,max} \\ 0 & \text{if } \varepsilon_i > \varepsilon_{i,max} \end{cases} \tag{3.1}$$

where ε_i and $\varepsilon_{i,max}$ are the actual strain and the failure strain in spring i, respectively. The damage D in the spring system is defined as the ratio of the number of failed springs n^* and the total number of springs n, which depends on the axial strain ε:

$$D(\varepsilon) = \frac{n^*(\varepsilon)}{n} \tag{3.2}$$

In a strain controlled experiment the damage accumulation can be monitored. Two load cases will be analyzed and the quality of the spring model will be discussed.

3.3 Axial Loading

3.3.1 Relationship Between Micro and Macro Stiffness Properties

Experimental observation of the structural material behavior, such as the force-displacement relationship of concrete subject to uniaxial compression for instance, is generally limited to the macro scale. It is therefore necessary to establish the relationship between the material properties used in a continuum mechanics model and the material characteristics of the individual springs, i.e. the micro-scale. Since only uniaxial stress states are considered and the transverse displacements are not considered, only Young's modulus E needs to be related to the individual spring stiffnesses.

The elastic deformation of a homogeneous continuous member with length ℓ, subject to an axial load P is:

$$\delta_c = \frac{P\ell}{EA} \tag{3.3}$$

where E denotes Young's modulus and A is the cross-sectional area of the member. The deformation of the spring system, consisting of n identical springs in parallel, each with stiffness k is:

$$\delta_d = \frac{P}{kn} \tag{3.4}$$

In one-dimensional applications, a continuum is considered equivalent to a discrete parallel-bar system if the deformations of the continuum (3.3) and the discrete model (3.4) are identical. This relates the Young's modulus E of the equivalent continuum to the spring stiffness k:

$$E = \frac{kn\ell}{A} \tag{3.5}$$

3.3.2 Load-Displacement Curve

Consider the parallel bar model in Figure 2.4. All n springs have an equal stiffness k, but a random failure strain $\varepsilon_{i,max}$. The spring model is subject to a monotonically increasing axial deformation and the force-displacement behavior is observed. This represents a numerical simulation of a displacement-controlled tensile test.

If all springs have identical failure strain, sudden failure occurs when $\varepsilon = \varepsilon_{i,max}$ (solid line in Figure 3.2 for the case $n = 4$). When the failure strains are different for each spring, the system failure occurs more gradually as each of the springs fails under a different load (dashed line in Figure 3.2 for the case $n = 4$). In this model, when a spring fails, the total load is redistributed evenly among all remaining springs. Note that the material behavior remains elastic as no permanent deformation is introduced; only the total stiffness of the spring system is affected by the damage accumulation. Using (3.1), the total axial force P carried by the spring system can be written as:

$$\begin{aligned} P(\varepsilon) &= \sum_{i=1}^{n} F_i \\ &= k\ell\varepsilon\,[n - n^*(\varepsilon)] \\ &= kn\ell\varepsilon\,[1 - D(\varepsilon)] \\ &= EA\varepsilon\,[1 - D(\varepsilon)] \end{aligned} \tag{3.6}$$

where ℓ is the length of the springs in the parallel bar model.

As the number of springs increases, the descending branch of the force displacement curve becomes less jagged. The shape of the resulting force-displacement diagram depends on the distribution of the failure strain $\varepsilon_{i,max}$. For illustration purposes, the force-displacement diagram is simulated for systems with $n = 10$ springs,

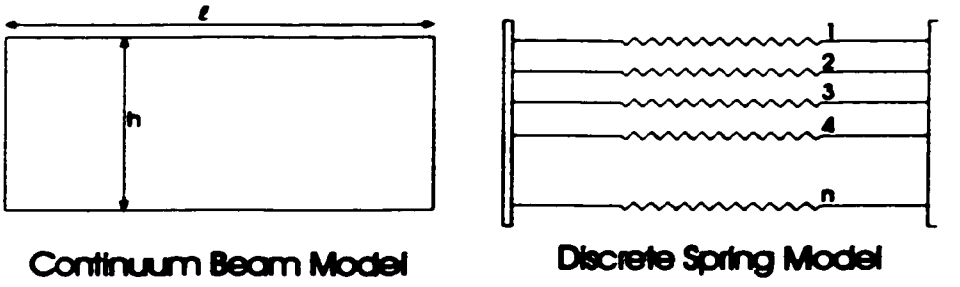

Figure 3.1: (a) Continuous and (b) micro-mechanical beam model

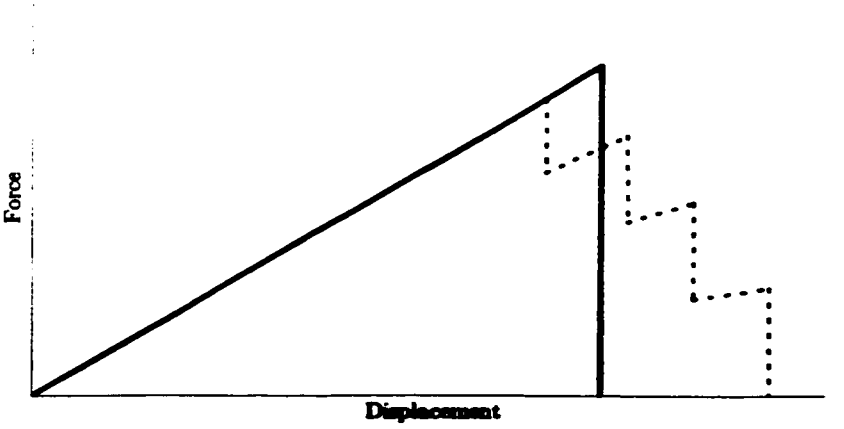

Figure 3.2: Progressive failure of a parallel bar system for $n = 4$ springs

where all failure strains $\varepsilon_{i,max}$, $i = 1 \ldots 10$ are IID random variables. When the $\varepsilon_{i,max}$, $i = 1 \ldots n$ are IID distributed, the damage D is a binomial random variable. Analytical expressions for the mean and variance are derived in the next section.

The mean and standard deviation of the force-displacement diagram obtained from 1000 Monte Carlo simulations are given in Figures 3.3 and 3.4, respectively, for four different types of probability distributions for the micro-level failure strain $\varepsilon_{i,max}$: a normal, a lognormal, a Weibull and a uniform PDF are assumed for $\varepsilon_{i,max}$. In the Figures 3.3 and 3.4, the mean is identical for all PDFs and the coefficient of variation (COV) is assumed equal to 20% for all probability distributions. It can be concluded that from the simulations that:

1. The average force-displacement behavior is not very sensitive to the assumed PDF for the micro-strain $\varepsilon_{i,max}$ (see Figure 3.3). All PDFs are assumed to have the same mean and standard deviation. The probability distribution type has little impact on the strength of the system since the maximal force is virtually identical for all assumed PDFs of the spring failure strain $\varepsilon_{i,max}$. Additional simulations have shown that only for much larger COV's of $\varepsilon_{i,max}$, there is a notable difference between the average force-displacement behavior for different micro-strain distribution types, particularly in the softening part of the diagram.

2. The variability of the force-displacement spring system is somewhat dependent on the probability distribution chosen for the micro-strength, especially in the softening part of the diagram (see Figure 3.4). However, the variability of the total system strength, i.e. the maximum load, is independent of the assumed

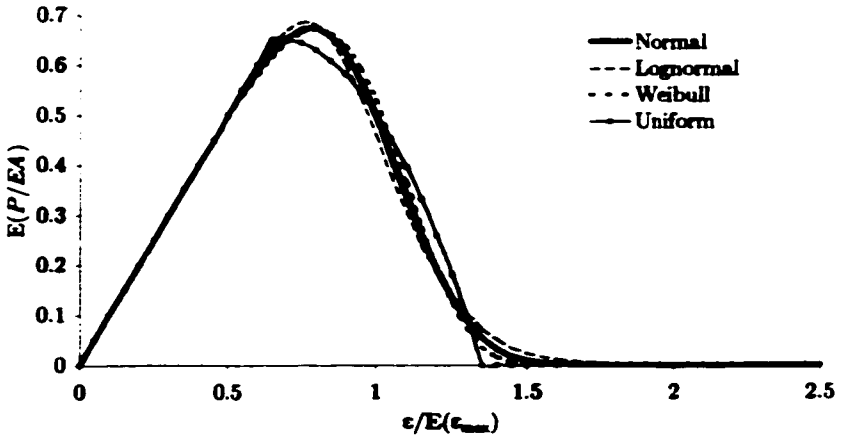

Figure 3.3: Mean force-displacement behavior of parallel bar model for different probability distributions of stiffness k ($n = 10$ springs)

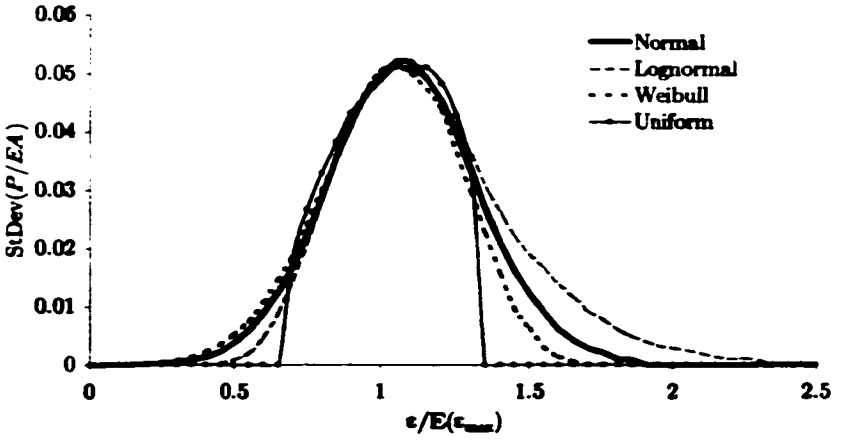

Figure 3.4: Standard deviation of force-displacement behavior of parallel bar model for different probability distributions of stiffness k ($n = 10$ springs)

PDF type for $\varepsilon_{i,max}$. This suggests that the uncertainty of the system strength is accurately predicted by second-moment information of the failure strain alone.

3. The system strength decreases with increasing COV($\varepsilon_{i,max}$). The expected value curve flattens as the variability of $\varepsilon_{i,max}$ increases as shown in Figure 3.5 when $\varepsilon_{i,max}$ is modeled by lognormal IID variables. Gasparini et al. (1996) assume a Weibull distribution for the failure strain and observe a similar trend. The tail of the average force-displacement curve increases with the COV of the failure strain $\varepsilon_{i,max}$. It is interesting that, due to the positive skewness of the lognormal distribution, the total average deformation energy stored in the spring system increases with the COV. Figure 3.6 shows that the standard deviation of the softening branch of the force-displacement diagram is heavily dependent on the COV of the assumed PDF for the microlevel failure strain.

4. Simulations for different numbers of springs in the network indicate that the COV of the force-displacement diagram decreases with increasing number of springs n. It can be shown [e.g. Daniels, 1945; Gasparini et al., 1996; Kandarpa et al., 1996] that COV($P(\varepsilon)$) $\propto n^{-1/2}$ so that a deterministic force-displacement is obtained for the parallel-bar system in the limit for $n \rightarrow \infty$, if the failure strains $\varepsilon_{i,max}$ are modeled as IID random variables.

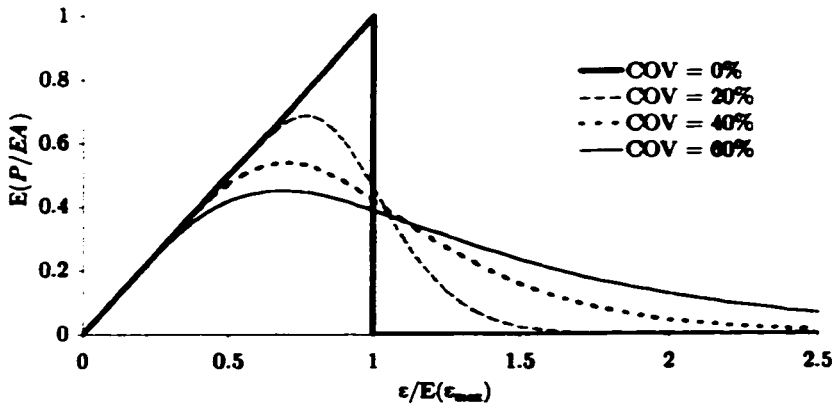

Figure 3.5: **Influence of the COV of lognormal micro-stiffness on the average macroscopic force-displacement curve ($n = 10$)**

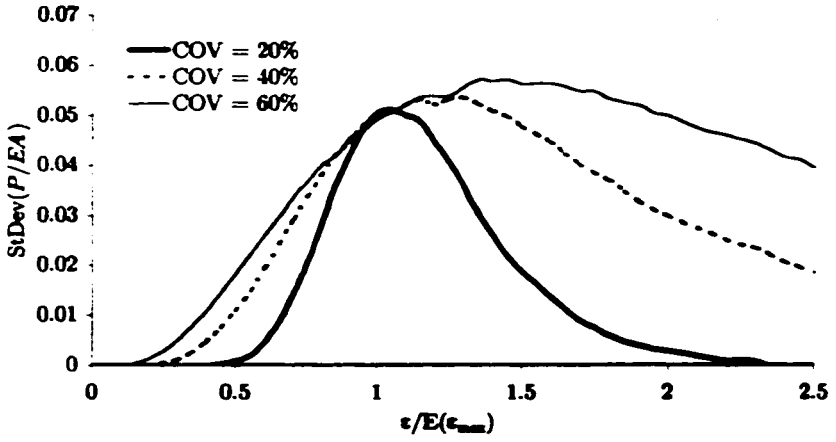

Figure 3.6: **Influence of the COV of lognormal micro-strength on standard deviation of macroscopic force-deformation curve ($n = 10$)**

3.3.3 Damage Accumulation

As the strain ε in the spring system increases, more and more springs fail and the damage D increases. In a discrete system the damage accumulation is given by:

$$D(\varepsilon) = \frac{n^*(\varepsilon)}{n} = \frac{1}{n}\sum_{i=1}^{n} \mathrm{H}(\varepsilon - \varepsilon_{i,\max}) \tag{3.7}$$

where H is the Heaviside or step function: $\mathrm{H} = 1$ if $\varepsilon \geq \varepsilon_{i,\max}$, $\mathrm{H} = 0$ otherwise. When the failure strains $\varepsilon_{i,\max}$ are IID variables, the damage variable D is equal to the probability of exactly n^* failures out of n, where each individual spring has an equal failure probability, and is thus a binomial random variable.

If it is assumed that the failure strains $\varepsilon_{i,\max}$ are either IID random variables or form a discrete, homogeneous, random field, the probability distributions of the failure strain $\varepsilon_{i,\max}$ are independent of i. In that case the marginal densities for the failure strains are identical for all springs i. If $f_{\varepsilon_{\max}}(\varepsilon)$ and $F_{\varepsilon_{\max}}(\varepsilon)$ denote the PDF and CDF of the failure strain $\varepsilon_{\max}$ respectively, the mean damage $\mathbf{E}(D(\varepsilon))$ for a given strain ε can be expressed in terms of the applied strain ε as follows:

$$\begin{aligned}
\mathbf{E}(D(\varepsilon)) &= \frac{1}{n}\sum_{i=1}^{n} \mathbf{E}(\mathrm{H}(\varepsilon - \varepsilon_{i,\max})) \\
&= \frac{1}{n}\sum_{i=1}^{n} \int_0^{\infty} f_{\varepsilon_{\max}}(\varepsilon_{i,\max}) \mathrm{H}(\varepsilon - \varepsilon_{i,\max})\, d\varepsilon_{i,\max} \\
&= \frac{1}{n}\sum_{i=1}^{n} \int_0^{\varepsilon} f_{\varepsilon_{\max}}(\varepsilon_{i,\max}) d\varepsilon_{i,\max} \\
&= F_{\varepsilon_{\max}}(\varepsilon)
\end{aligned} \tag{3.8}$$

This result can also be obtained by making use of the binomial property of the damage variable. Gasparini et al. (1996) and Kandarpa et al. (1996) derive expressions for the expected value and standard deviation of the load P and damage D as a function of the applied strain ε.

From a microscopic point of view, damage accumulation occurs when new cracks are induced by large strains. According to Lemaitre and Chaboche (1985) this damage grows linearly with strain under monotonic loading. They suggest using the following linear law, which is well in accord with experimental results for many metallic materials:

$$D = D_c \frac{\varepsilon - \varepsilon_{vD}}{\varepsilon_{vR} - \varepsilon_{vD}} \tag{3.9}$$

where ε_{vD} is the effective strain at the damage threshold, below which no significant damage exists and ε_{vR} is the effective strain at fracture at which point the damage D reaches its critical value D_c. Based on the micro-mechanical analysis, only the assumption of a uniform strength distribution in (3.8) leads to a linear damage accumulation law, such as (3.9). However, Figure 3.7 indicates that (3.9) may prove a reasonable approximation for other distributions of the failure strain as well, as long as the COV of the failure strain remains relatively small in as much as a bi-linear ramp function approximates the lower part of the typical S-curve of a CDF.

3.3.4 Tensile Strength of Parallel Bar System

The expected value of the force-displacement curve is given by:

$$\mathbf{E}\left(P(\varepsilon)\right) = EA\varepsilon\left[1 - \mathbf{E}\left(D(\varepsilon)\right)\right] \tag{3.10}$$

The strength $P_{\max}$ of the parallel-bar system is obtained by setting $dP/d\varepsilon = 0$ and solving for P. When the ultimate strain of each spring $\varepsilon_{i,\max}$ is modeled by an IID random variable, the resulting force-displacement behavior is deterministic in the limit for $n \to \infty$ [e.g. Daniels, 1945; Gasparini et al., 1996; Kandarpa et al., 1996].

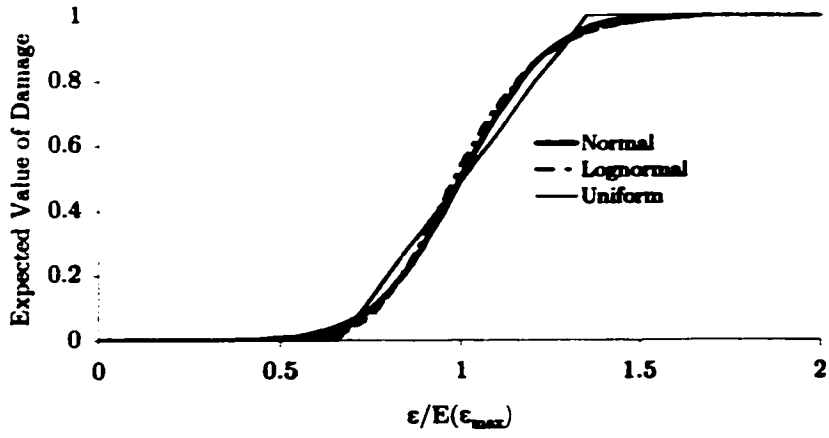

Figure 3.7: Expected value of damage accumulation during tensile test for different choices of the PDF for $\varepsilon_{\max}$ ($n = 10$, COV($\varepsilon_{\max}$) = 20%)

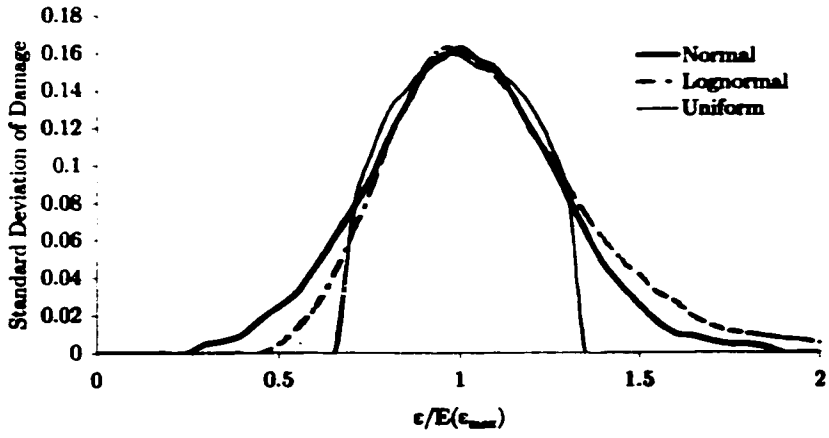

Figure 3.8: Standard deviation of damage accumulation during tensile test for different choices of the PDF for $\varepsilon_{\max}$ ($n = 10$, COV($\varepsilon_{\max}$) = 20%)

This means that in this case:

$$\frac{dP}{d\varepsilon} = \frac{d(\mathbf{E}(P(\varepsilon)))}{d\varepsilon}$$

It should be noted that, when $n \neq \infty$, the strain at which the strength P_{max} is reached is random itself. The distribution of the critical strain ε_{crit} where the system strength P_{max} is achieved can then only be obtained through simulation. Analytical expressions can only be obtained for the case of $n \rightarrow \infty$ and IID conditions and the discussion is restricted to this particular case.

Substitution of the damage equation (3.8) into the expression for the expected load (3.10), gives, when the system strength P_{max} is reached, the strain in the spring system ε is given as the solution of:

$$\varepsilon_{crit} = \frac{1 - F_{\varepsilon_{max}}(\varepsilon)}{f_{\varepsilon_{max}}(\varepsilon)} = \frac{1}{h(\varepsilon)} \tag{3.11}$$

where $h(\varepsilon)$ is the so-called hazard rate. The hazard rate $h(\varepsilon)$ is defined as the instantaneous failure rate of a spring, subject to a strain ε, given that failure has not yet occurred for smaller strains [Martz and Waller, 1982].

Substitution of the solution ε_{crit} of (3.11) into (3.6) and (3.8) allows us to establish the impact of the PDF assumed for the failure strain ε_{max} on the system strength P_{max} and the damage level at this failure load. The analysis is performed for two types of non-negative PDFs for the failure strain ε_{max} in Tables 3.1 and 3.2. It can be concluded the damage level $D(\varepsilon_{crit})$ at this critical strain is a monotonically increasing function of the COV, and does not depend much on the PDF-type chosen for ε_{max}. The system strength P_{max} decreases with increasing COV (see also Figure 3.5). The critical strain level ε_{crit}, at which the system strength is achieved, at

first decreases with the COV, but then increases again for the selected PDFs. This may seem somewhat counter-intuitive, but it should be kept in mind that the force deflection curve is very flat for these very large COV's: the load P does not change much for strain-values in a fairly large neighborhood of ε_{crit}. Also, this result was obtained for a lognormal distribution of ε_{max} and may not hold true for other PDF types.

3.3.5 Influence of Correlation between Failure Strains

When $n \to \infty$, a deterministic expression is obtained for the force-displacement and the damage accumulation curve if the springs are assumed independent [Gasparini et al., 1996]. Since this conflicts with experimental evidence it can be concluded that, when a continuum model rather than a discrete spring system is used to model the observed variability of actual test specimens, the failure strains of the springs should not be assumed to be independent. A continuous random field model of ε_{max} should be used instead.

The amount of correlation between the failure strains of neighboring springs is given by the autocorrelation function R of the random field ε_{max}, defined in Section 1.4. For a homogeneous RF, this autocorrelation function R only depends on the distance between the springs.

Kandarpa et al. (1996) use a RF model for the failure strain ε_{max} and derive expressions for the mean and variance of the accumulated damage and the force-displacement curve. The expressions for the expected value of the damage $D(\varepsilon)$ (3.8) and the force $P(\varepsilon)$ (3.10) for a given applied strain ε, obtained using IID ε_{max}, are still valid when a random field model is used for ε_{max}. The variance, however,

$\mathrm{COV}(\varepsilon_{max})$ [%]	$\mathbf{E}(D(\varepsilon_{crit}))$ [%]	$\varepsilon_{crit}/\mathbf{E}(\varepsilon_{max})$	$P_{max}/(EA\mathbf{E}(\varepsilon_{max}))$
0	0	1.00	1.00
5	2	0.90	0.88
10	5	0.85	0.80
20	14	0.79	0.68
40	31	0.76	0.53
60	44	0.79	0.44
80	53	0.83	0.39
100	60	0.87	0.35

Table 3.1: Impact of COV of failure strain on system strength, damage level and critical strain for a lognormal distribution of the failure strain ε_{max} ($n = 10$)

$\mathrm{COV}(\varepsilon_{max})$ [%]	$\mathbf{E}(D(\varepsilon_{crit}))$ [%]	$\varepsilon_{crit}/\mathbf{E}(\varepsilon_{max})$	$P_{max}/(EA\mathbf{E}(\varepsilon_{max}))$
0	0	1.00	1.00
5	4	0.90	0.86
10	8	0.85	0.78
20	16	0.80	0.67
40	31	0.78	0.54
60	44	0.82	0.46
80	55	0.90	0.40
100	63	1.00	0.37

Table 3.2: Impact of COV of failure strain on system strength, damage level and critical strain for a Weibull distribution of the failure strain ε_{max} ($n = 10$)

depends on the correlation function R.

They use the parallel bar model to simulate the force-displacement behavior of normal and lightweight concrete test specimens subject to axial tension. They assume a homogeneous, lognormal random field for the ultimate strain ε_{max} with an exponential auto–correlation function. The random field is then characterized by 3 parameters: mean μ and standard deviation σ of ε_{max}, and the correlation length l_c in the autocovariance function $B_{\varepsilon_{max}}$ of the random field ε_{max} (see definition in Section 1.4):

$$B_{\varepsilon_{max}}(\tau) = \sigma^2 \exp(-\tau/l_c)$$

where τ is the positive distance between the two points. The corresponding auto-correlation function (see definition in Section 1.4)

$$R_{\varepsilon_{max}}(\tau) = \exp(-\tau/l_c) \tag{3.12}$$

is an important characteristic of the random field. The amount of correlation between neighboring springs determines the relationship between the variance of the total spring system compared with the variance of the individual spring behavior.

In Kandarpa et al.'s (1996) study, the mean and standard deviation of the ultimate strain field ε_{max} are obtained from a least squares fit of the expected value of the force-displacement curve to the experimental data. They estimate the correlation parameter l_c through a least squares fit of the theoretical variance of the force-displacement curve to the experimental evidence. They find that the correlation length l_c is about 5 times smaller for lightweight concrete than for normal concrete. They conclude that there is less variance in the force-displacement curve for lightweight than for normal weight concrete.

It should be noted that even though a good agreement is achieved between the model and the experiments for the mean and mean square force-displacement behavior, the variance of the softening branch is far less accurately predicted by the spring model (see Kandarpa et al. (1996)).

3.4 Pure Bending

3.4.1 Deterministic Continuum Model

When a brittle beam, such as a plain concrete beam, is subject to pure bending, the neutral axis of the cross section will shift due to the progressive cracking of the beam [Ghali and Favre, 1994]. The moment-curvature relationship for a continuum model of a beam section is given by:

$$M = E\left(I - \frac{B^2}{A}\right)\psi \tag{3.13}$$

where M is bending moment, ψ is the curvature, and I and B are the moment of inertia and the first moment of the cross-section of area A with respect to an arbitrarily chosen reference axis, respectively. Here, this reference axis is chosen at the top of the cross section. For an uncracked, homogeneous and rectangular cross-section of width b and depth h, equation (3.13) becomes:

$$M(\psi) = E\frac{bh^3}{12}\psi \tag{3.14}$$

When the curvature increases, the beam cracks as soon as the tensile strain ϵ exceeds the ultimate strain ϵ_{max}. Compressive failure is not considered in this model. In the cracked state (Figure 3.9), the bending moment is absorbed by the shaded part of the cross-section only. Because, the cross-section is assumed to remain plane

after deformation, the horizontal strain ε varies linearly along the y-axis, defined in Figure 3.9:

$$\varepsilon = \varepsilon_0 + y\psi \tag{3.15}$$

with ε_0 is the strain at the reference axis at the top of the cross section, and y is the distance measured downwards from the top of the beam. At the fiber y_u, the strain ε is equal to the failure strain ε_{max}:

$$\varepsilon_{max} = \varepsilon_0 + y_u\psi \tag{3.16}$$

Since the beam is homogeneous, the neutral axis is located at the middle of the shaded section. Since the strain ε is zero at $y = y_u/2$, the following result is obtained for ε_0:

$$\varepsilon_0 = -\tfrac{1}{2}y_u\psi \tag{3.17}$$

which leads to the following relationship between the failure strain ε_{max} and the effective, uncracked depth of the beam y_u:

$$\varepsilon_{max} = \tfrac{1}{2}y_u\psi \tag{3.18}$$

Substitution of (3.18) into (3.13), combined with the uncracked state equation (3.14), gives the following result for the moment-curvature relationship:

$$M(\psi) = \begin{cases} E\frac{bh^3}{12}\psi & \text{if } \psi \le \frac{2\varepsilon_{max}}{h} \\ \frac{2}{3}Eb\epsilon_{max}^3\psi^{-2} & \text{if } \psi > \frac{2\varepsilon_{max}}{h} \end{cases} \tag{3.19}$$

When the failure strain ε_{max} is considered a random variable, a first-order second-moment (FOSM) expansion of the deterministic result (3.19) indicates that when $\psi > \frac{2\varepsilon_{max}}{h}$:

$$\mathrm{Var}(M) \cong \left(2Eb\mathbf{E}(\varepsilon_{max})^2\psi^{-2}\right)^2 \mathrm{Var}(\varepsilon_{max}) \tag{3.20}$$

or, after dividing the square root of (3.20) by the first-order approximation of the expected value of the bending moment M in (3.19):

$$\mathrm{COV}(M) \cong 3\mathrm{COV}(\varepsilon_{\max}) \tag{3.21}$$

3.4.2 Discrete Spring Model

The parallel bar model is used to analyze the progressive failure of a beam section subject to bending. As the curvature of the beam increases, the springs gradually start to fail. Even when a deterministic failure strain $\varepsilon_{\max}$ is used, the moment-curvature diagram of the parallel bar model has a gradually descending branch because of the strain gradient over the different springs. Figure 3.10 compares the moment-curvature diagram of a parallel bar model with 10 evenly spaced springs and the continuum model, given by (3.19).

Based on the linear-elastic brittle force-displacement model (3.1), the moment-curvature relationship is given by the following expression:

$$M(\psi) = \psi k \ell \left[\sum_{i=n^*(\psi)+1}^{n} y_i^2 - \frac{\sum_{i=n^*(\psi)+1}^{n} y_i \sum_{j=n^*(\psi)+1}^{n} y_j}{n - n^*(\psi)} \right] \tag{3.22}$$

where the sums include only those springs, $n - n^*$ in total, which did not fail. Failure of springs is determined by comparison of the failure strain $\varepsilon_{i,\max}$ with the actual strain ε_i in spring i:

$$\varepsilon_i(\psi) = \psi \left(y_i - \frac{\sum_{j=n^*(\psi)+1}^{n} y_j}{n - n^*(\psi)} \right) \tag{3.23}$$

In the next section it will be shown that, using the equivalence relation (3.5), (3.22) is identical to (3.13) in the limit for $n \to \infty$.

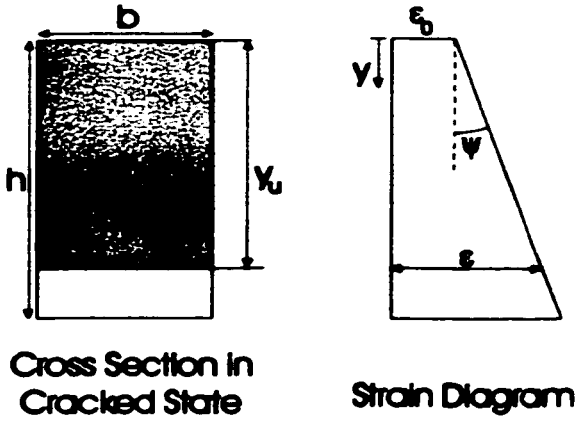

Figure 3.9: Analysis of continuous beam model, subject to pure bending

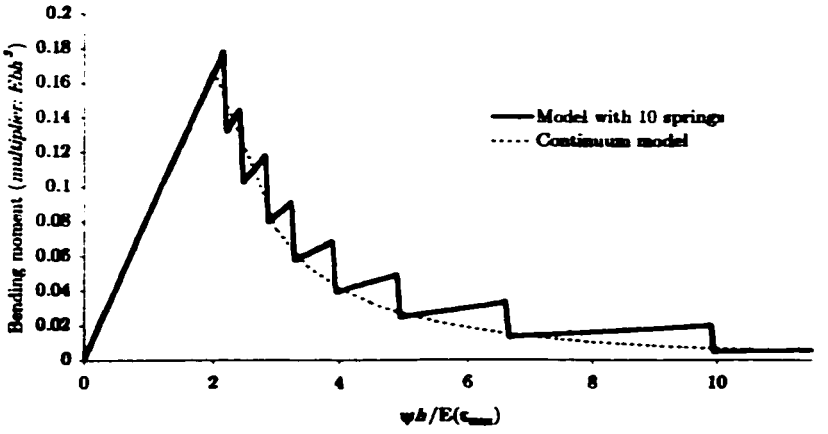

Figure 3.10: Comparison of moment-curvature diagram for a discrete spring model ($n = 10$) and for a continuum model using a deterministic failure strain ε_{max}

When the failure strain $\varepsilon_{i,max}$ is modeled as a discrete random process, closed form solutions for the average moment-curvature relationship become mathematically intractable because the individual springs are subject to different strains. Monte Carlo simulations of spring systems, where all failure strains $\varepsilon_{i,max}$ are modeled as IID random variables, show that the type of PDF assumed for $\varepsilon_{i,max}$ has almost no influence on the average moment-curvature diagram.

3.4.3 Relationship Between Micro and Macro Properties

Substitution of the relationship between the micro and the macro stiffness (3.5), derived for uniform deformations, the moment-curvature relationship (3.22) becomes:

$$M(\psi) = \psi \frac{EA}{n} \left[\sum_{i=n^*(\psi)+1}^{n} y_i^2 - \frac{\sum_{i=n^*(\psi)+1}^{n} y_i \sum_{j=n^*(\psi)+1}^{n} y_j}{n - n^*(\psi)} \right] \tag{3.24}$$

Since the ratio A/n is equal to the area A_i of layer i, we can write:

$$M(\psi) = \psi E \left[\sum_{i=n^*(\psi)+1}^{n} y_i^2 A_i - \frac{\sum_{i=n^*(\psi)+1}^{n} y_i \sum_{j=n^*(\psi)+1}^{n} y_j A_i}{n - n^*(\psi)} \right] \tag{3.25}$$

or

$$M(\psi) = \psi E \left[\sum_{i=n^*(\psi)+1}^{n} y_i^2 A_i - \frac{\sum_{i=n^*(\psi)+1}^{n} y_i \sum_{j=n^*(\psi)+1}^{n} y_j}{A_i \left[n - n^*(\psi) \right]} \right] \tag{3.26}$$

In the limit for $n \rightarrow \infty$, $\sum_{i=n^*(\psi)+1}^{n} y_i \sum_{j=n^*(\psi)+1}^{n} y_j A_i$, $\sum_{i=n^*(\psi)+1}^{n} y_i A_i$, $A_i \left[n - n^*(\psi) \right]$ are equal to the moment of inertia I, the first moment B and the area A of the cracked cross-section in Figure 3.9, respectively, and equation for the micromechanical (3.26) becomes identical to (3.13). It can be concluded that the same relationship between the micro and macro stiffness properties holds for both the pure bending and the axial deformation load case.

3.4.4 Damage Accumulation

The insensitivity of the macroscopic system response to the probability distribution type selected to model the uncertainty at the micro-level is also reflected in the average damage accumulation. The damage accumulation (3.2) is calculated from (3.7), which becomes:

$$D(\psi) = \frac{1}{n}\sum_{i=1}^{n} \mathrm{H}\left(y_i\psi - \frac{\sum_{j=n^*(\psi)+1}^{n} y_j\psi}{n - n^*(\psi)} - \varepsilon_{i,\max}\right) \tag{3.27}$$

Simulations indicate that the average damage accumulation $\mathbf{E}(D(\psi))$ is virtually independent of the assumed PDF type for the failure strain $\varepsilon_{i,\max}$ of the discrete springs. The average damage accumulation diagram, obtained from 1000 Monte Carlo simulations, is shown in Figure 3.11. The same three PDF types and COV value (20%) are used as in Figure 3.7, which allows a direct comparison of the Figures 3.7 and 3.11. It can be concluded that the structural response mode governs the damage accumulation, and that the assumed type of the PDF for the failure strain has virtually no impact.

The impact of the COV on the average damage accumulation is shown in Figure 3.12, in the case of a lognormal PDF for the failure strain $\varepsilon_{\max}$. It can be concluded that the COV of the failure strain affects the damage accumulation in the parallel bar system only at the onset of the progressive failure of the springs. The COV($\varepsilon_{\max}$) has no impact on the damage accumulation for $D \geq 35\%$. This implies that the tail of the moment-curvature diagram (Figure 3.10) is not affected by COV($\varepsilon_{\max}$).

Figure 3.13 shows that the variability of the damage accumulation is independent of the selected PDF for the micro-level failure strain as well. The standard deviation

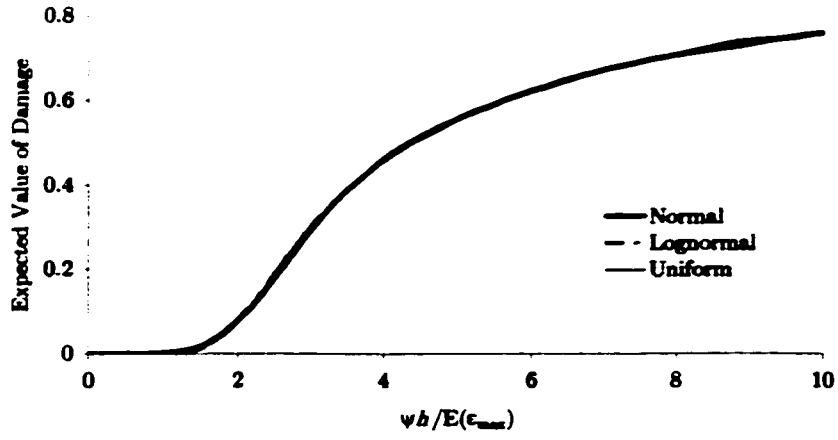

Figure 3.11: Average damage accumulation in spring system subject to bending ($n = 10$ springs, COV($\varepsilon_{\max}$)= 20%)

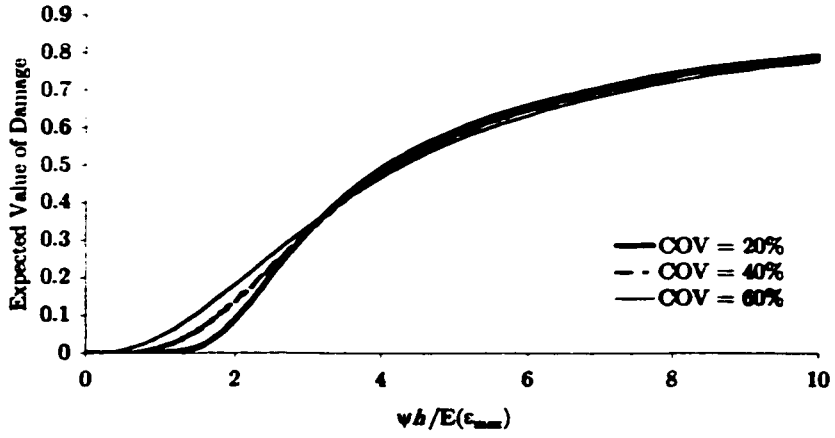

Figure 3.12: Average damage accumulation in spring system subject to bending for different values of COV($\varepsilon_{\max}$) ($n = 10$ springs, lognormal distribution for $\varepsilon_{\max}$)

of D is heavily dependent on the variability of the failure strain as shown in Figure 3.14. It can be concluded that second-moment information of ε_{max} is sufficient to accurately predict the moment-curvature and damage accumulation diagrams and their variability.

Comparison of the Figures 3.13 and 3.14 indicates that, when all failure strains $\varepsilon_{i,max}$ are IID distributed, the standard deviation of the damage D decreases with the number of springs n. It can be shown that, similar to the axial loading case, the damage accumulation - and hence, the moment-curvature relationship - becomes deterministic in the limit for $n \to \infty$ when the failure strains $\varepsilon_{i,max}$ are uncorrelated.

3.4.5 Bounds on Variability: Two Limiting Auto-Correlation Functions

The variability of the moment-curvature diagram cannot be described using a continuum model when the failure strains are IID. A random field model, which accounts for the amount of correlation between the failure strains of neighboring springs, is required for ε_{max}.

When a non-negative autocorrelation function, such as (3.12), is assumed for the random field ε_{max}, two limiting cases can be identified: no correlation between the ultimate strains of the individual springs, and perfect correlation. This corresponds to a zero and infinite correlation length ℓ_c, respectively.

If all ultimate strains $\varepsilon_{i,max}$ are perfectly correlated ($\ell_c = \infty$), all springs have the same failure strain and the discrete random process $\varepsilon_{i,max}$ is reduced to one random variable ε_{max}. In this case there is no difference between the micro-mechanical model (3.22) and the continuum model (3.19). If the correlation length $\ell_c = 0$, the discrete random process $\varepsilon_{i,max}$ consists of n independent random variables.

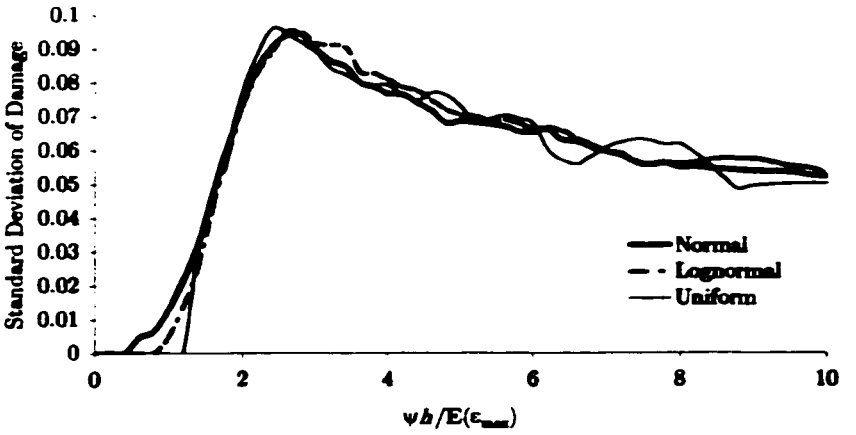

Figure 3.13: Standard deviation of D in spring system subject to bending ($n = 10$ springs, COV(ε_{max}) = 20%)

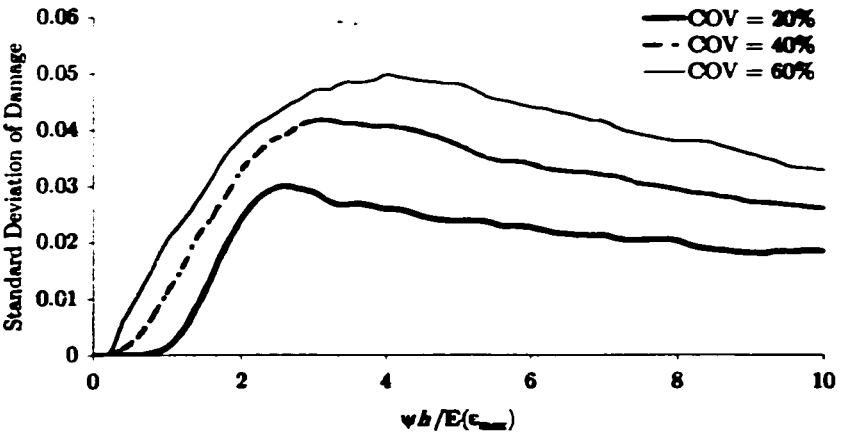

Figure 3.14: Standard deviation of D in spring system subject to bending for different values of the COV of the lognormal distribution for ε_{max} ($n = 100$ springs)

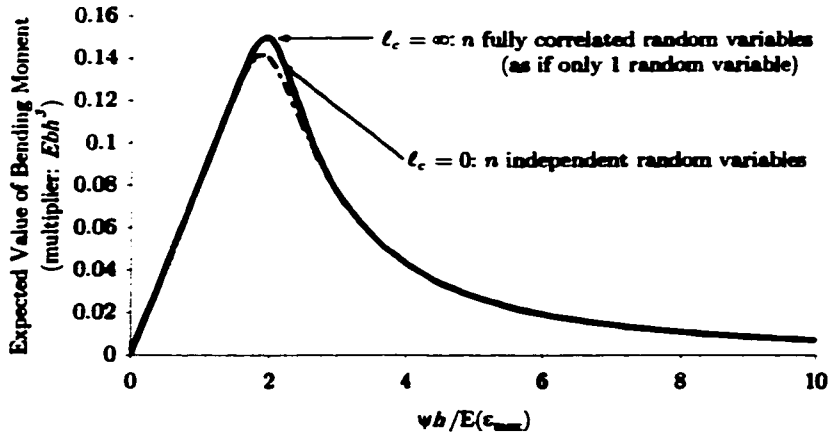

Figure 3.15: Impact of correlation length l_c on average moment-curvature diagram ($n = 100$ springs)

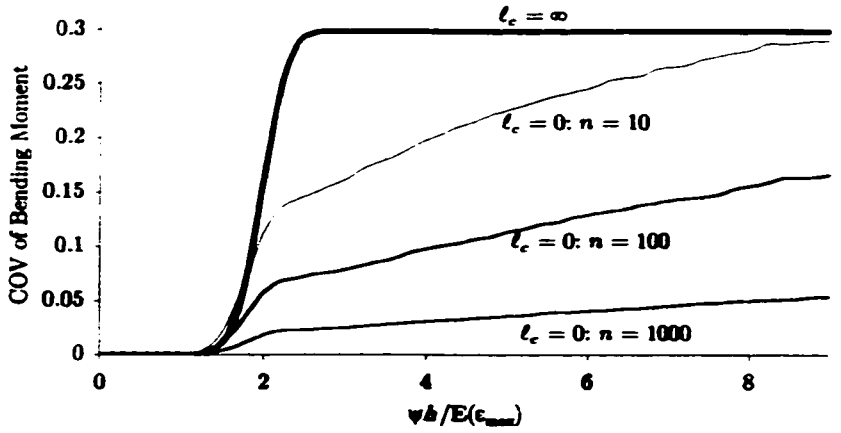

Figure 3.16: Impact of correlation length l_c on COV of moment-curvature diagram

The impact of the correlation length is assessed by means of an example. A Gaussian random field is assumed for $\varepsilon_{i,max}$, characterized by its mean $\mathbf{E}(\varepsilon_{max}) = 1$ and standard deviation $\text{StDev}(\varepsilon_{max}) = 0.1$. The model contains 100 springs and the results are obtained using 1000 Monte Carlo simulations. Figure 3.15 suggests that the average moment-curvature diagram is not much affected by the choice of the correlation model ($\ell_c = 0$ or $\ell_c = \infty$). Figure 3.16, however, clearly demonstrates the effect the correlation length ℓ_c has on the COV in the post-peak region. When the layers are perfectly correlated, COV(M) reaches a stable value of 30%, which is readily derived from $\text{COV}(\varepsilon_{max}) = 0.1$ using equation (3.19), almost immediately after some of the springs fail. When the layers are uncorrelated, this plateau is reached only for much larger values of the curvature for finite n.

When the classical continuum mechanics result of (3.19) is used as the basis of an uncertainty analysis, the failure strain ε_{max} is modeled as a random variable. In this case, COV(M) is equal to 30%, estimated by FOSM. It is interesting to see how this straightforward randomization of the classical continuum mechanics result is identical to the result, obtained when an infinite correlation length is assumed in the micromechanical model. When a reliability analysis is based on the randomization of a deterministic continuum model, it should be kept in mind that the continuum model tacitly assumes perfect correlation of all material characteristics, such as stiffness and strength, throughout the material. Because the micromechanical model does not make this assumption, it gives additional insight into the failure mechanism and a more realistic description of the progressive failure can be obtained.

Figure 3.16 also indicates that the number of springs in the model has an effect on the COV of the bending moment, in agreement with previous discussions.

3.5 Summary

In this chapter the progressive failure of parallel bar systems, which are subject to normal stresses only, is studied. A linear elastic-brittle micro-constitutive law is used. The springs fail in tension only, and all springs have equal deterministic spring stiffness k. The failure strains $\varepsilon_{i,max}$, $i = 1 \ldots n$, are modeled by random variables, and ε_{max} becomes a continuous random field in the limit for $n \rightarrow \infty$. The model indicates that complex macroscopic behavior can be realistically modeled on the basis of a simple micro-constitutive law.

The damage growth in a specimen, subject to axial tension only, is linked to the probability distribution function of the microlevel failure-strain. The model also suggests that the average moment-curvature diagram is not much dependent on type of PDF, selected for ε_{max}.

However, there is no known relationship between the number of springs in the model and the physical micro-structure and size of the specimen. This introduces some severe limitations in the model. It is known that the variability in the structural behavior of actual materials decreases with the specimen size. The parallel bar model cannot simulate this. Also, the link stiffness k depends on the number of springs in the model, which strips it from its physical meaning.

The analyses clearly demonstrate the impact of the auto-correlation of the failure strain ε_{max} on the macroscopic variability of the structural response. However, there is no theoretical basis to select the auto-correlation function of the random field for ε_{max}. As such, a correlation model must be chosen somewhat arbitrarily.

It can be concluded that even though a parallel bar model provides insight in

the mechanics of materials, its practical use is limited. The model parameters must be determined for each configuration and cannot be generalized to, for instance, other specimen sizes. These shortcomings disappear when a micro-mechanical model, which is directly related to physical dimensions of the microstructure in a material, is used. The homogenization of such micro-structural models is the subject of the next chapter.

Chapter 4

Stochastic Homogenization

4.1 Introduction

In this chapter, a framework for the micromechanically-based estimation of the random field characteristics of elastic properties is presented. A homogenization procedure is outlined, which allows computation of the macroscopic elastic material properties of a "homogeneous" continuum on the basis of a micromechanical model. This continuum is said to be equivalent to the assembled microstructure, and an exact definition of this "equivalence" is given in Section 4.3.

Several existing homogenization techniques for microstructures with regular and random geometry are reviewed. A new homogenization technique, which complements existing methods, is presented. The homogenization algorithm requires the specification of boundary conditions. The shortcomings of existing boundary condition models are highlighted and an improved boundary condition model is suggested.

The elastic properties of the equivalent continuum are considered sample local averages of the continuous random field of elastic properties. A Monte Carlo simulation of the microstructure allows the estimation of the stochastic characteristics of the locally averaged random field of elastic properties. The proposed technique allows to derive both the autocorrelation function of the random field and the correlations between the different elastic properties directly from the micromechanical model.

4.2 Overview of Stochastic Homogenization

Stochastic homogenization consists of the following three steps:

1. Selection of an appropriate micromechanical model. An overview of micromechanical models was given in Chapter 2. The model should contain enough detail (Table 1.2) to explain the variability of the macroscopic behavior. Only the main deformation mechanisms need to be included in the micromodel [Bažant et al., 1990].

2. Selection of an appropriate homogenization technique. Various techniques are discussed in Sections 4.3-4.5 and 4.7. The computation of sample equivalent continua is based on a Monte Carlo simulation of the microstructure.

3. Estimation of the stochastic characteristics of the random fields representing the elastic properties of the homogenized material. This is the subject of Section 4.6. Practical applications are considered in Chapter 5.

4.3 Equivalence Between Continua and Discrete Models

The objective of homogenization is to replace a discrete microstructure with an equivalent continuum and to derive the probabilistic material parameters of this "equivalent" continuum from the micro-structural model. Figure 4.1 illustrates the link between the micro-model and the macro-continuum.

- Figure 4.1a represents a series of random samples of a discrete microstructure. There is a sample-to-sample geometric variability, as well as sample-to-sample

variability due to the uncertainty associated with the constitutive parameters in the micro-model.

- Figure 4.1b represents the corresponding idealization: a macroscopically homogeneous continuum.

Since Figure 4.1b must be structurally and statistically equivalent to Figure 4.1a, it is clear that the mechanical properties of the continuum must form a random field themselves. The continuum random field is assumed ergodic [Papoulis, 1991]: the sample-to-sample variability at the heterogeneous micro-structural scale translates into random spatial variations of the mechanical characteristics of the homogenized continuous macro-structure. It is also assumed to be statistically homogeneous which means that the random field properties do not depend on the location. The homogenization technique is applicable to both lattice-type micromodels and discrete particle microstructures.

Consider a sample of the deformed micro-structural model of the material as shown in Figure 4.2. Because the field is assumed to be homogeneous, we can, without loss of generality, consider only a window, which is cut out from the entire microstructure. This window should be large enough to allow for homogenization; it must be of at least the same size as the representative volume element (RVE). Note that the micro-scale model can be either a lattice or a particle model.

Generally speaking, a continuum can be considered equivalent to a micromechanical model if the same deformations occur when both systems are subject to identical load conditions. It was explained in Chapter 1 that all materials are to some extent heterogeneous: they consist of discrete constituents. The effective properties of a

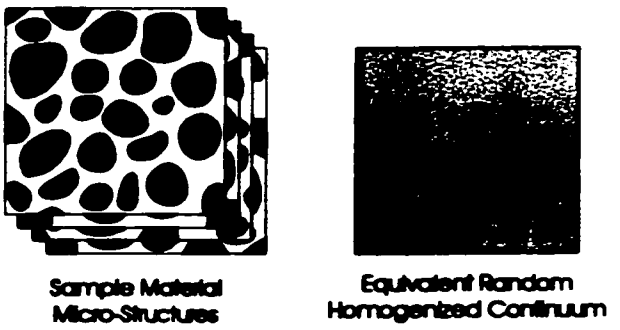

Figure 4.1: **Sample discrete microstructures and equivalent homogenized random continuum**

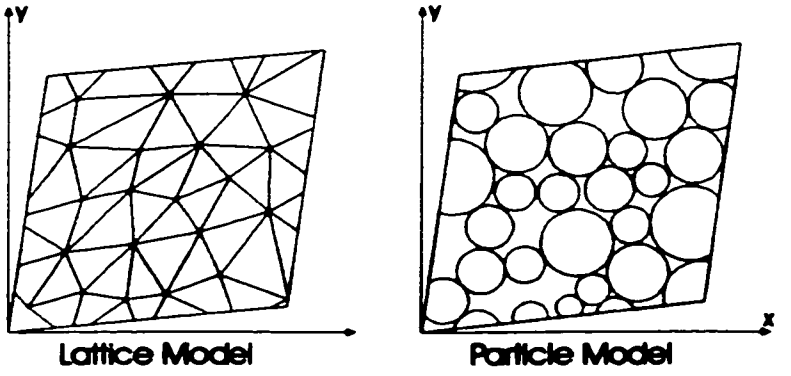

Figure 4.2: Deformed microstructures

heterogenous material define the relations between average stresses and strains if the spatial variation thereof is statistically homogeneous (SH) [Beran, 1968]. When the microscopic variation of the material behavior is of no practical interest, we only need to develop a statistical model for the effective material properties.

To this extent, we first need to produce a SH field in the microstructure by applying appropriate boundary conditions. Two types of boundary conditions can be distinguished for the homogenization window:

- *essential boundary conditions*: the displacements on the boundaries of the microstructure and the continuum are identical.
- *natural boundary conditions*: the stresses on the boundaries of the microstructure and the continuum are identical.

Hashin (1983) refers to these boundary conditions as "homogeneous" because they introduce an SH stress or strain field in the microstructure. Ostoja-Starzewski (1993) calls them "uniform boundary conditions" because they lead to uniform stress or strain fields in the equivalent homogeneous continuum. In this work, we will adopt the term "uniform boundary conditions".

An alternative definition of effective properties can be given in terms of energy expressions. This is based on the theorem of virtual work, and, when applied to linear elastic materials, states that the strain energy in the continuum must be identical to that in the microstructure when both are subject to the same "uniform boundary conditions". The equivalence of the definition using average or effective properties and the one based on strain energy was first pointed out by Hill (1963) and Hashin (1964).

The assumption of uniform boundary conditions on the window boundary has some important consequences:

- Since only the boundary displacements are prescribed and the total strain energy in the homogenization window must be identical for equivalence, no information is available regarding the deformation state inside the homogenization window. This becomes important when non-linear material behavior is considered. Localized phenomena, such as cracks, will be smeared out over the homogenization window.

- No inference can be made regarding other deformation states. In a FE context, this means that this type of homogenization is consistent with the use of constant strain or constant stress elements only. Strictly speaking, when other shape functions are used in the FE analysis, the boundary conditions used for homogenization should be modified accordingly. Hashin (1983) argues that this effect is minimal for most engineering problems.

Higher-order appoximations of the deformation or stress field are only necessary when very high stress and strain gradients are present, such as near crack tips [Beran and McCoy, 1970]. However, a detailed study of localized phenomena requires a discretization at a scale smaller than the RVE. In that case, a mixed continuum-discrete model should be used.

4.4 Microstructures with Regular Geometry

4.4.1 Introduction

Many crystalline materials have regular micro-structures. Most of the variability in their structural material properties can be attributed to random impurities, such as inclusions of other materials or other phases, or to defects in the regular mesh, such as voids. For those materials a model with regular microgeometry may prove useful as a starting point since the actual microstructure can be modeled as a disturbed regular lattice model.

The inclusions or defects can be modeled as either truly random in space or using a randomly periodic micromodel. In the latter model, the pattern of the inclusions is considered to be random within a window but is repeated all throughout the microstructure. The periodicity of this type of micro-structure allows for an efficient homogenization using periodic boundary conditions. Examples of random periodic micromodels are given in Figure 4.3. Because of the geometric periodicity at the window boundaries, the windows in Figure 4.3 connect to the adjoining windows in the microstructure without overlap.

In this section, planar models with both a square and a triangular microstructure are homogenized. The triangular microstructure can be regarded as a limiting case where all distances between the micro-constituents are equal.

4.4.2 Homogenization of Regular Lattice Structures

Analytic expressions can be derived for the elastic properties of the equivalent continua, obtained after homogenization of discrete systems with a regular microgeom-

etry. Consider the square particle model, represented in Figure 4.4a. When only the axial interactions between the particles are considered, the particle model can be replaced with the lattice model in Figure 4.4b. The window considered for homogenization consists of 4 smaller "sub-cells" with alternating directions for the diagonal links, and is indicated by the dashed line in Figure 4.4b. For now, it will also be assumed that all link stiffnesses are deterministic and equal to k_1 for the horizontal and vertical links of length a, and equal to k_2 for the diagonal links of length $a\sqrt{2}$.

For a deterministic linear elastic system with regular geometry, the use of either essential or natural boundary conditions results in identical macro-continuum properties after homogenization. The homogenization procedure is outlined using essential boundary conditions only. A constant strain state $\{\boldsymbol{\varepsilon}\} = \left\{ \begin{array}{ccc} \varepsilon_x & \varepsilon_y & \varepsilon_{xy} \end{array} \right\}^T$ is applied to both the discrete and continuous model and, according to the structural equivalence principle, the elastic strain energy stored in both systems should be equal. For a continuum, the constitutive equation for 2D linear elastic behavior is:

$$\{\boldsymbol{\sigma}\} = [\mathbf{C}]\,\{\boldsymbol{\varepsilon}\} \tag{4.1}$$

or

$$\left\{ \begin{array}{c} \sigma_x \\ \sigma_y \\ \sigma_{xy} \end{array} \right\} = \left[\begin{array}{ccc} C_{11} & C_{12} & C_{13} \\ & C_{22} & C_{23} \\ sym & & C_{33} \end{array} \right] \left\{ \begin{array}{c} \varepsilon_x \\ \varepsilon_y \\ \varepsilon_{xy} \end{array} \right\}$$

where [C] is a symmetric matrix of elastic moduli, $\{\boldsymbol{\sigma}\}$ the vector of plane stress components and $\{\boldsymbol{\varepsilon}\}$ the vector of strain components. The elastic strain energy $U^{(e)}$ of a square element with dimension $A = 2a \times 2a$, subject to constant strain state

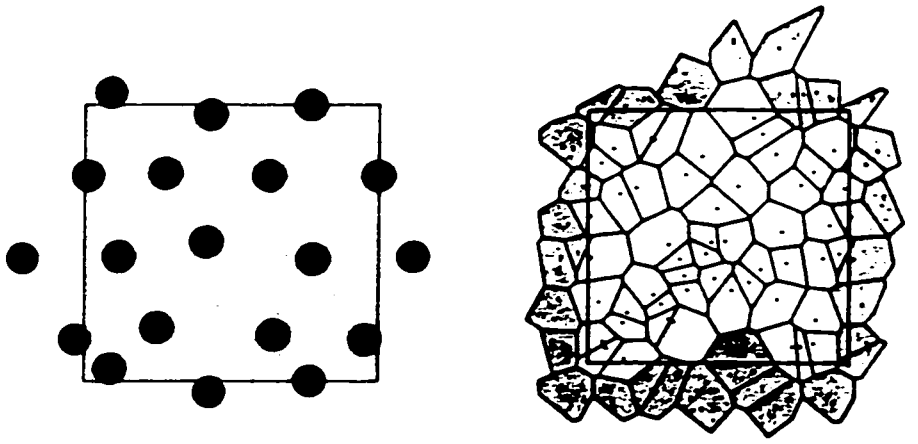

Figure 4.3: Examples of random periodic microstructures: periodic inclusion model [Ostoja-Starzewski et al., 1994] and periodic cell model [Okabe et al., 1992]

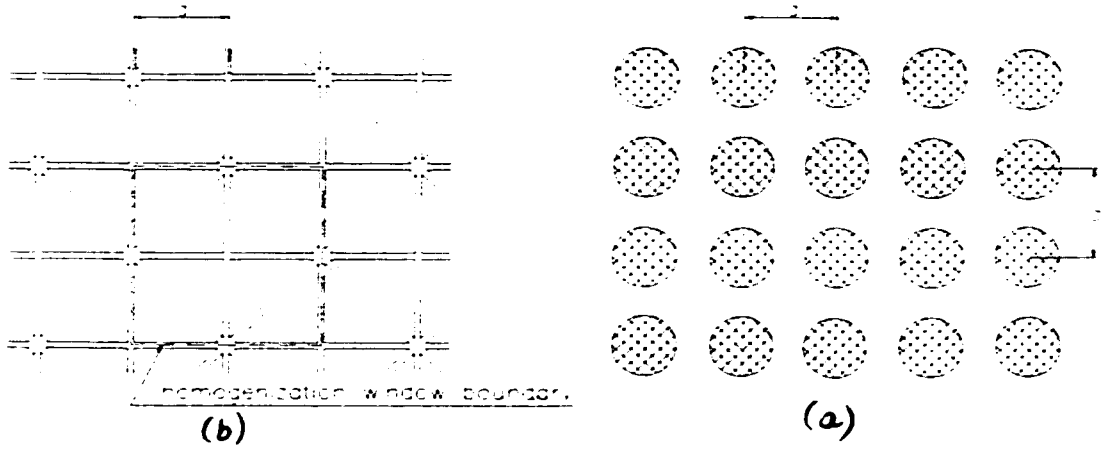

Figure 4.4: Square lattice microstructure and corresponding discrete particle model (circular disks assumed for particle model)

$\{\varepsilon\}$ is equal to:

$$\begin{aligned} U^{(c)} &= \tfrac{1}{2}\int_A \{\sigma\}^{\mathrm{T}}\{\varepsilon\}\,dA \\ &= 2a^2\left[\begin{array}{c} C_{11}\varepsilon_x^2 + C_{22}\varepsilon_y^2 + C_{33}\varepsilon_{xy}^2 + 2C_{12}\varepsilon_x\varepsilon_y + \dots \\ \dots + 2C_{13}\varepsilon_x\varepsilon_{xy} + 2C_{23}\varepsilon_y\varepsilon_{xy} \end{array}\right] \end{aligned} \tag{4.2}$$

Only half the strain energy associated in the 8 links along the window edge is included in the calculation of the strain energy in the discrete system $U^{(d)}$ since those 8 links are shared between 2 homogenization windows. If e_i denotes the elongation of a link i under the strain state $\{\varepsilon\}$, the total strain energy $U^{(d)}$ stored in the discrete system in Figure 4.4b is given by:

$$\begin{aligned} U^{(d)} &= \sum_{i=1}^{4}\tfrac{1}{2}k_1e_i^2 + \sum_{i=1}^{4}\tfrac{1}{2}k_2e_i^2 + \tfrac{1}{2}\sum_{i=1}^{8}\tfrac{1}{2}k_1e_i^2 \\ &= 2a^2\left[\left(k_1+\tfrac{k_2}{2}\right)\left(\varepsilon_x^2+\varepsilon_y^2\right) + \tfrac{k_2}{2}\varepsilon_{xy}^2 + k_2\varepsilon_x\varepsilon_y\right] \end{aligned} \tag{4.3}$$

Comparison of (4.2) and (4.3) leads to the conclusion that the strain energies of the homogeneous continuum and a square lattice micro-mechanical model are identical for an arbitrary strain state $\{\varepsilon\}$, if and only if the following conditions are satisfied:

$$\begin{cases} C_{11} = k_1 + \frac{k_2}{2} \\ C_{12} = \frac{k_2}{2} \\ C_{13} = 0 \\ C_{22} = k_1 + \frac{k_2}{2} \\ C_{23} = 0 \\ C_{33} = \frac{k_2}{2} \end{cases} \tag{4.4}$$

The symmetric elasticity matrix [C] of an isotropic continuum in 2D plane stress

elasticity is:

$$[\mathbf{C}] = \frac{E}{1-\nu^2}\begin{bmatrix} 1 & \nu & 0 \\ & 1 & 0 \\ sym & & \frac{1-\nu}{2} \end{bmatrix} \tag{4.5}$$

From (4.4) and (4.5) it follows that the equivalent homogenized continuum of a square lattice model is an isotropic continuum if the spring stiffnesses k_1 and k_2 satisfy the following conditions:

$$\begin{cases} k_1 + \frac{k_2}{2} = \frac{E}{1-\nu^2} \\ k_2 = \frac{E(1-\nu)}{1-\nu^2} = \frac{E}{1+\nu} \\ k_2 = \frac{2E\nu}{1-\nu^2} \end{cases} \tag{4.6}$$

This can be achieved only if $\nu = \frac{1}{3}$ and $k_1 = k_2 = \frac{3E}{4}$. Note that the lattice model is isotropic only when deformations on the outside boundaries of the homogenization window are considered. True isotropy inside the homogenization window can never be achieved in a discrete microstructure with regular geometry. Directional dependence of the material characteristics must exist to some extent and cannot be avoided in discrete models with regular geometry. This is an illustration of the above mentioned fact that the equivalence principle does not allow inference about the deformation state inside the homogenization window.

Triangular stackings of circular disks are another example of a commonly observed regular dense packing in the plane (Figure 4.5a). A regular equilateral triangular truss system (Figure 4.5b) is the representation of axial interactions between the particles in this model. All links are assumed to have an equal stiffness k. The same homogenization procedure can be applied to the triangular lattice structure. The

elastic energy stored in the isotropic continuum and the lattice model are equal only if $\nu = \frac{1}{3}$ and $k = \sqrt{3}E/2$.

Hrennikoff (1941) analyzed several types of regular lattice models, and found the value $\nu = \frac{1}{3}$ returning for several planar truss systems. When spatial truss models are considered, the value $\nu = \frac{1}{4}$ is obtained.

4.4.3 Modeling of Link Stiffness

Based on the equivalence of 1D continua and parallel bar models, the spring stiffness of the discrete link is given by:

$$k = \frac{EA}{L} \tag{4.7}$$

Based on the requirement $k_1 = k_2$ for a regular square lattice for isotropy obtained from (4.6), Schlangen (1993) concludes that the spring stiffness in the lattice model should not only depend on the link length but also on the "cross-sectional area" A. In a discrete particle model, with polygon-shaped cells, the interface area between neighboring cells is readily available to compute the stiffness k [Zubelewicz and Bažant, 1987].

When a lattice model is used, however, this area is not directly available in the model. Gasparini et al. (1996) use a constant stiffness k, independent of the link length ℓ and cross-section A to simulate the behavior of elastic brittle networks. In this research, the linear elastic link behavior is governed by the following force-displacement relationship:

$$F = K\frac{\Delta x}{\ell} \tag{4.8}$$

where F is the axial force in any truss member, K a stiffness parameter, Δx is the elongation of the link, which is calculated from the displacements at both end nodes,

and ℓ is the link length. The force-displacement law (4.8) is in agreement with the contact law used in studies by Bathurst and Rothenburg (1988), Ting et al. (1988) and Jirásek and Bažant (1995).

4.4.4 Limitations of Regular Geometries

As outlined in Chapter 2, micromechanical models with regular geometry may have limited applicability in simulations of the structural behavior of many materials. Two reasons can be indicated:

1. The regular mesh geometry introduces directional bias of the material properties. This was observed by Jirásek and Bažant (1995) in micro-mechanical simulations of quasi-brittle fracture of ice sheets. They observed that the crack pattern in the simulations heavily depends on the orientation of the links in the lattice model with respect to the direction of the applied force. This directional bias persists even when the strength and stiffness of the links is randomized.

2. Ostoja-Starzewski and Wang (1989) observed that the second-order characteristics of the random fields, which describe the material properties of the homogenized micromechanical models with regular geometry and random link stiffness, are substantially different from the ones found in models with random geometry. On this basis, Ostoja-Starzewski and Wang (1989) conclude that regular networks cannot accurately reflect the variability of the structural behavior of randomly disordered media.

4.5 Homogenization of Random Micro-Structures

4.5.1 Introduction

The homogenization techniques described in this section can be applied to a specific sample of the discrete microstructure (i.e. one "frame" in Figure 4.1a), and the elasticity matrix [C] of the equivalent continuum can be determined for a given microstructure and homogenization window size A.

Repeated application to a large random sample of micro-structures – which is the basic principle of Monte Carlo simulation – enables one to estimate, statistically, the probabilistic characteristics of the macro-structural properties. The most convenient way of describing these continuum properties is by using random fields, which is the subject of the Section 4.6.

It can be shown that, under some conditions, the equivalent continua obtained from the equivalence principle using essential and natural boundary conditions correspond to Voigt (upper) and Reuss (lower) bounds for the actual stiffness of the microstructure respectively [Kröner, 1980]. These bounding techniques are particularly useful if the available information on the microstructure is incomplete [Mirfendereski et al., 1996]. However, Sab (1992) proves that the properties of an elastic medium, computed using either stress or strain boundary conditions, are identical when the exact microstructure is known.

Homogenization using strain boundary conditions is developed in Ostoja-Starzewski and Wang (1989) and Ostoja-Starzewski and Wang (1990). A stress-based technique [Huyse and Maes, 1999a] is described in this dissertation.

4.5.2 Displacement-Based Homogenization Techniques

Structural analysis can be performed using either a displacement or a force method. For many practical applications, the Finite Element Method (FEM) is the preferred analysis method. Since the FEM is a displacement method, it makes sense to homogenize the heterogeneous microstructure using essential boundary conditions.

For the linear elastic case, the structural equivalence principle requires that the same amount of strain energy is accumulated in both the continuum and the discrete model when subject to identical boundary deformations. The derivations are presented for 2D in-plane linear elastic behavior only but can be extended to general 3D elasticity.

Consider the discrete micromodel and homogenization window in Figure 4.6. This window is subjected to a uniform strain field $\{\boldsymbol{\epsilon}\} = \left\{ \begin{array}{ccc} \epsilon_x & \epsilon_y & \epsilon_{xy} \end{array} \right\}^{\mathrm{T}}$. For a continuum the constitutive equation for 2D linear elastic behavior is given in equation (4.1). The average elastic energy density per unit area w_c is then given as $\left([\mathbf{C}] = [\mathbf{C}]^{\mathrm{T}}\right)$:

$$w_c = \tfrac{1}{2} \{\boldsymbol{\sigma}\}^{\mathrm{T}} \{\boldsymbol{\epsilon}\} = \tfrac{1}{2} \{\boldsymbol{\epsilon}\}^{\mathrm{T}} [\mathbf{C}] \{\boldsymbol{\epsilon}\} \tag{4.9}$$

The structural behavior of the discrete model, shown in Figure 4.6, is governed by the following equation [Ghali and Neville, 1989]:

$$[\mathbf{S}] \{\mathbf{u}\} = \{\mathbf{F}\} \tag{4.10}$$

where [S], {u}, and {F} are the stiffness matrix of the microstructure, the deformation, and external force vectors at the nodes of the micro-mechanical model, respectively. The discrete micromechanical model is subject to the same deformation as the continuum. This is achieved by prescribing the displacement at each of the

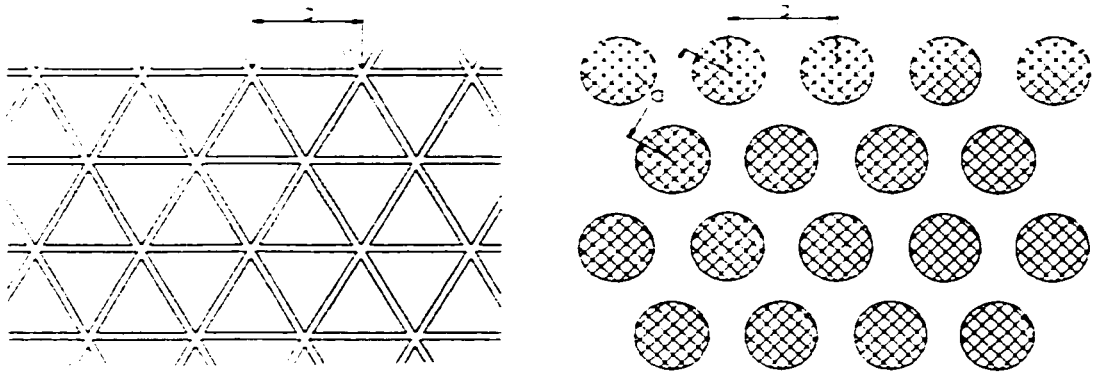

Figure 4.5: Triangular lattice microstructure and corresponding particle model (circular disks assumed for particle model)

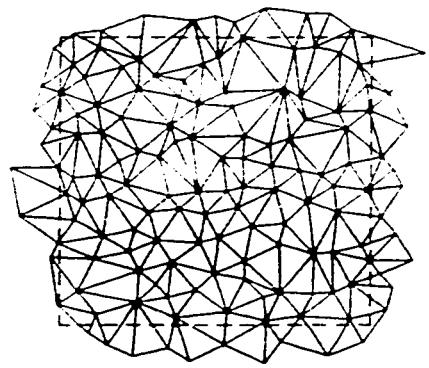

Figure 4.6: Discrete microstructure in homogenization window

nodes on the exterior boundary of the window. Note that the area of the micromodel is typically slightly larger than the homogenization window.

Since all externally applied forces act on the boundary nodes, i.e. the nodes outside the averaging window indicated by the dotted line in Figure 4.6, the system of equations (4.10) can be partitioned as:

$$\begin{bmatrix} \mathbf{S}_{ii} & \mathbf{S}_{ib} \\ \mathbf{S}_{ib}^{\mathrm{T}} & \mathbf{S}_{bb} \end{bmatrix} \begin{Bmatrix} \mathbf{u}_i \\ \mathbf{u}_b \end{Bmatrix} = \begin{Bmatrix} \mathbf{0} \\ \mathbf{F}_b \end{Bmatrix} \tag{4.11}$$

where the index i denotes interior nodes inside the window and boundary nodes are indexed by the letter b. Eliminating $\{\mathbf{u}_i\}$, we obtain:

$$\left[\mathbf{S}_{bb} - \mathbf{S}_{ib}^{\mathrm{T}}\mathbf{S}_{ii}^{-1}\mathbf{S}_{ib}\right]\{\mathbf{u}_b\} = \{\mathbf{F}_b\} \tag{4.12}$$

or

$$[\mathbf{S}^*]\{\mathbf{u}_b\} = \{\mathbf{F}_b\} \tag{4.13}$$

The average energy density w_d for the discrete micro-mechanical model in the homogenization window of size A is equal to:

$$w_d = \tfrac{1}{2A}\{\mathbf{u}_b\}^{\mathrm{T}}[\mathbf{S}^*]\{\mathbf{u}_b\} \tag{4.14}$$

According to the equivalence principle, the energy densities for the homogenized continuum (4.9) and the discrete model (4.14) must be identical:

$$\tfrac{1}{2}\{\boldsymbol{\epsilon}\}^{\mathrm{T}}[\mathbf{C}]\{\boldsymbol{\epsilon}\} \equiv \tfrac{1}{2A}\{\mathbf{u}_b\}^{\mathrm{T}}[\mathbf{S}^*]\{\mathbf{u}_b\} \tag{4.15}$$

However, no solution for the elastic stiffness [C] can be obtained from this equation unless an assumption is made regarding the deformed state of the material.

In continuum mechanics, uniaxial stresses and strains in a point are defined as the force F per unit area A and deformation $\Delta\ell$ per unit length ℓ.

$$\sigma = \lim_{A \to 0} \frac{F}{A}, \; \varepsilon_x = \lim_{\ell \to 0} \frac{\Delta \ell}{\ell} \tag{4.16}$$

The stress distribution over a given area A is assumed to become more and more uniform as the area A decreases. Similarly for the strain so that, in the limit, a constant strain ε is obtained for infinitesimally small ℓ. In a micromechanical approach, the constituents on the microscale have finite dimensions. Consequently, stresses and strains can not be defined in the usual way since limits for infinitesimal areas or lengths are undetermined, which renders (4.16) difficult to apply. However, the assumption of a constant strain within the window still makes sense because it is consistent with constant strain finite elements. In that case, the boundary displacements $\{\mathbf{u}_j\} = \{u_{x,j}, u_{y,j}\}^{\mathrm{T}}$ of node j with coordinates (x_j, y_j) can be written as (the rigid body displacement of the window is irrelevant):

$$\begin{Bmatrix} u_{x,j} \\ u_{y,j} \end{Bmatrix} = \begin{bmatrix} x_j & 0 & y_j/2 \\ 0 & y_j & x_j/2 \end{bmatrix} \begin{Bmatrix} \varepsilon_x \\ \varepsilon_y \\ \varepsilon_{xy} \end{Bmatrix} \tag{4.17}$$

or, in matrix notation for all n_b boundary nodes together:

$$\begin{Bmatrix} u_{x,1} \\ u_{y,1} \\ \vdots \\ u_{x,n_b} \\ u_{y,n_b} \end{Bmatrix} = \begin{bmatrix} x_1 & 0 & y_1/2 \\ 0 & y_1 & x_1/2 \\ & \vdots & \\ x_{n_b} & 0 & y_{n_b}/2 \\ 0 & y_{n_b} & x_{n_b}/2 \end{bmatrix} \begin{Bmatrix} \varepsilon_x \\ \varepsilon_y \\ \varepsilon_{xy} \end{Bmatrix} \tag{4.18}$$

or

$$\{\mathbf{u}\}_{2n_b \times 1} = [\mathbf{B}]_{2n_b \times 3} \{\boldsymbol{\epsilon}\}_{3 \times 1} \tag{4.19}$$

Substitution of (4.18) in (4.14) and comparison with (4.9) allows us to derive the equation for the elastic moduli C_{ij} of the equivalent homogeneous continuum:

$$[\mathbf{C}] = \frac{1}{A} [\mathbf{B}]^{\mathrm{T}} [\mathbf{S}^*] [\mathbf{B}] \tag{4.20}$$

where the strain-displacement matrix [B] is defined in (4.18).

The evaluation of the matrix $[\mathbf{S}^*]$ in (4.20) requires the computation of the inverse matrix $[\mathbf{S}_{ii}]^{-1}$, whose dimension increases with the averaging window size A. Consequently, the evaluation of equivalent continuum properties becomes computationally more expensive as the window size increases; the computer time increases with A^3. For this reason, Ostoja-Starzewski and Wang (1990) introduced the so-called uniform strain approximation, which avoids the inversion of $[\mathbf{S}_{ii}]$. In this approximation the displacement is prescribed at both the internal and the boundary nodes of the discrete model:

$$\begin{Bmatrix} u_{x,1} \\ u_{y,1} \\ \vdots \\ u_{x,n} \\ u_{y,n} \end{Bmatrix} = \begin{bmatrix} x_i & 0 & y_1/2 \\ 0 & y_1 & x_1/2 \\ & \vdots & \\ x_n & 0 & y_n/2 \\ 0 & y_n & x_n/2 \end{bmatrix} \begin{Bmatrix} \varepsilon_x \\ \varepsilon_y \\ \varepsilon_{xy} \end{Bmatrix} \tag{4.21}$$

or

$$\{\mathbf{u}\}_{2n \times 1} = \left[\tilde{\mathbf{B}}\right]_{2n \times 3} \{\boldsymbol{\epsilon}\}_{3 \times 1} \tag{4.22}$$

With this approximation, the elasticity matrix [C] of the equivalent continuum

follows directly from (4.15):

$$[\mathbf{C}] = \frac{1}{A}\left[\tilde{\mathbf{B}}\right]^{\mathrm{T}} . [\mathbf{S}] . \left[\tilde{\mathbf{B}}\right] \tag{4.23}$$

where [S] is the stiffness matrix of the unsupported microstructure.

Because the displacements are now prescribed for every node, it is to be expected that this approximate method will lead to an overestimation of the stiffness properties in the equivalent, homogenized continuum.

4.5.3 Force-Based Homogenization Techniques

The energy density of the 2D equivalent continuum can also be written in terms of stresses:

$$w_c = \frac{1}{2}\{\boldsymbol{\sigma}\}^{\mathrm{T}}\{\boldsymbol{\epsilon}\} = \frac{1}{2}\{\boldsymbol{\sigma}\}^{\mathrm{T}}[\mathbf{C}]^{-1}\{\boldsymbol{\sigma}\} \tag{4.24}$$

The deformation of the discrete microstructure can also obtained using the force method instead of the displacement method. Similarly to (4.11), the structural response of the discrete microstructure is given by [Ghali and Neville, 1989]:

$$\begin{bmatrix} \mathbf{f}_{ii} & \mathbf{f}_{ib} \\ \mathbf{f}_{ib}^{\mathrm{T}} & \mathbf{f}_{bb} \end{bmatrix} \begin{Bmatrix} \mathbf{0} \\ \mathbf{F}_b \end{Bmatrix} = \begin{Bmatrix} \mathbf{u}_i \\ \mathbf{u}_b \end{Bmatrix} \tag{4.25}$$

where [f] stands for the flexibility matrix of the discrete microstructure, and {F} and {u} are the external force and displacement vectors at the nodes of the micro-mechanical model respectively.

From (4.25), it follows that:

$$[\mathbf{f}_{bb}]\{\mathbf{F}_b\} = \{\mathbf{u}_b\} \tag{4.26}$$

where $[\mathbf{f}_{bb}]$ is the flexibility matrix of the discrete microstructure: the flexibility coefficient f_{ij} gives the displacement at boundary node i when a unit force is applied at boundary node j. The elastic energy density for the window A is:

$$w_d = \frac{1}{2A} \{\mathbf{F}_b\}^T [\mathbf{f}_{bb}] \{\mathbf{F}_b\} \tag{4.27}$$

No solution can be obtained for [C] through the equivalence of (4.24) and (4.27), unless an assumption is made regarding the stress distribution on the boundary of the homogenization window.

For reasons, similar to the ones described for the constant strain approximation in the previous section, a constant stress state $\{\sigma\}$ is assumed in the continuum. The forces applied on the boundary nodes can be related to the constant stress vector using a two-step process. In the first step we apply a force at each of the outside nodes whose magnitude is given by the horizontal or vertical distance between the centers of the adjacent links along the window boundary (see Figure 4.7). For the top edge, we have for node j:

$$\begin{cases} F'_{jx} = \tau_{xy} \ell_j \\ F'_{jy} = \sigma_y \ell_j \end{cases} \tag{4.28}$$

This ensures a force distribution which is as close as possible to the uniform stresses required. However, this system of forces is not in equilibrium when the nodes are not evenly distributed along the window edge, which is the case for networks with random geometry. Generally, application of (4.28) on all sides leads to imbalance forces $\Delta F'_x$ and $\Delta F'_y$ and an imbalance moment ΔM.

In the second step, a set of corrector forces F''_j is introduced which will ensure equilibrium is satisfied. To minimize their impact on the original stress distribution,

a least-squares minimization of the relative corrector magnitudes is performed. The deviation from the uniform stress modeling on the boundary is due to the irregular spacing of the nodes in the microstructure. The optimization problem can be formulated as a quadratic programming problem:

$$\begin{aligned} &\min g = \textstyle\sum_{j=1}^{n_b} \left(F''_{jx}/F'_{jx}\right)^2 + \left(F''_{jy}/F'_{jy}\right)^2 \\ &\text{subject to} \begin{cases} \sum_{j=1}^{n_b} F''_{jx} = -\Delta F'_x \\ \sum_{j=1}^{n_b} F''_{jy} = -\Delta F'_y \\ \sum_{j=1}^{n_b} \left(F''_{jx} y - F''_{jy} x\right) = -\Delta M \end{cases} \end{aligned} \tag{4.29}$$

The total force on a boundary node is given by the sum of the forces obtained in (4.28) and (4.29):

$$F_j = F'_j + F''_j \tag{4.30}$$

It should be noted that several alternative formulations to the computation of F'_j (4.28) and F''_j (4.29) are possible. The following alternative version ensures that the total force on each side is equivalent to the assumed constant stress. However, typically a few fairly large corrector forces F''_j are obtained with this reformulated optimization. It should be noted that the larger the maximum difference between the corrector forces along an edge is, the more the force system deviates from the assumed constant stress distribution.

In this alternative formulation, the forces in the first step are given by (consider again the top edge in Figure 4.7):

$$\begin{cases} F'_{jx} = \tau_{xy} \ell_j \frac{a}{\ell_{tot}} \\ F'_{jy} = \sigma_y \ell_j \frac{a}{\ell_{tot}} \end{cases} \tag{4.31}$$

where a is length of the window edge and ℓ_{tot} is the horizontal distance (or vertical

distance when the side edges are considered) along the edge between the two outermost nodes in the network. This set of equations ensures that force equilibrium is exactly satisfied along each edge. $\Delta F'_x = \Delta F'_y = 0$ and only a moment imbalance ΔM exists. In the second step the corrector forces are found from:

$$\begin{aligned} &\min g = \textstyle\sum_{i=1}^{n_b} \left(F''_{jx}/F'_{jx}\right)^2 + \left(F''_{jy}/F'_{jy}\right)^2 \\ &\text{subject to} \begin{cases} \sum_{i=1}^{n_{b_{iside}}} F''_{jx} = 0 \text{ for } iside = 1 \ldots 4 \\ \sum_{i=1}^{n_{b_{iside}}} F''_{jy} = 0 \text{ for } iside = 1 \ldots 4 \\ \sum_{i=1}^{n_b} \left(F''_{jx} y - F''_{jy} x\right) = -\Delta M \end{cases} \end{aligned} \tag{4.32}$$

where $n_{b_{iside}}$ represents the number of boundary nodes along edge *iside*.

The corrector forces $F''_{j\cdot}$ are a linear function of the assumed stresses, σ_x, σ_y or τ_{xy}, used in the first step (4.31). The relationship between the total external forces (4.30) and the assumed uniform stresses can thus be written in matrix form:

$$\{\mathbf{F_b}\}_{2n_b \times 1} = [\mathbf{H}]_{2n_b \times 3} \{\boldsymbol{\sigma}\}_{3 \times 1} \tag{4.33}$$

where the transformation matrix H only depends on the geometry of the microstructure and is computed using the two-step process described above. It should be noted that the value of the goal function $g = \sum_{i=1}^{n_b} \left(F''_{jx}/F'_{jx}\right)^2 + \left(F''_{jy}/F'_{jy}\right)^2$ is an error measure for the deviation from the desired constant stress state. This relative error becomes smaller as the averaging window size A increases.

Substitution of (4.33) in (4.27), together with the equivalence of (4.27) and (4.24) leads to the following result for the elasticity matrix [C]:

$$[\mathbf{C}] = \left(\tfrac{1}{A} [\mathbf{H}]^{\mathrm{T}} [\mathbf{f_{bb}}] [\mathbf{H}]\right)^{-1} \tag{4.34}$$

The matrix $[\mathbf{f_{bb}}]$ still needs to be determined. Formally, $[\mathbf{f_{bb}}]$ can be obtained through an inversion of [S], since the same coordinate system of forces and displace-

ments is used for the formation of the two matrices. However, the matrix [S] is the stiffness matrix of the unsupported microstructure and is thus singular, which means that a straightforward inversion of [S] is not possible [Ghali and Neville, 1989].

Since the microstructure is in equilibrium under the boundary forces $\{\mathbf{F}_b\}$, it is straightforward to introduce a set of boundary conditions, which make the microstructure statically determinate. These boundary conditions only affect the rigid body displacement and rotation, but do not alter the strain energy. With these boundary conditions the matrix [S] becomes non-singular. Note that, depending on which nodal displacements are prescribed, the flexibility matrix $[\mathbf{f}_{bb}]$ will vary according to the particular boundary conditions, which are imposed, but the strain energy (4.27) stored in the microstructure will remain the same.

The computational advantage of this technique over the displacement-based one is that the calculation of $[\mathbf{f}_{bb}]$ requires only $2n_b$ columns of [S] to be inverted. Computation of $[\mathbf{S}^*]$, however, requires inversion of $2n_i$ columns of [S]. Since n_b varies linearly with the window dimensions, while n_i increases quadratically, the force-based technique becomes increasingly more interesting from a computational point of view as the window size A increases. This advantage leads to considerable savings in the context of Monte Carlo simulation. The force-based homogenization is typically faster as soon as the network contains more than 15 to 25 nodes. The bandwidth of $[\mathbf{S}_{bb}]$ can easily be kept very low as well.

4.6 Estimation of the Equivalent Macro-Random Fields

4.6.1 Introduction

Application of any of the homogenization procedures discussed in the previous section results in a Monte Carlo data series for the elastic moduli, C_{ij}, of the equivalent continuum for different homogenization windows A. The objective of this section is to indicate how a continuum random field description can be derived from the statistics of these Monte Carlo data. This continuum random field model for [C] allows the use of a Stochastic Finite Element Method (SFEM) for structural analysis.

In this section a brief overview of the required random field theory is given first. Extensive use is made of the locally averaged random field theory. An excellent reference on random field theory is Vanmarcke (1983). Applications of locally averaged random fields to a structural analysis problem can be found in Vanmarcke and Grigoriu (1983) and Chakraborty and Dey (1996). Fitting experimental data to a random field model is discussed in Vanmarcke (1994) and Fenton (1999b). A digital simulation method, developed specifically for locally averaged random fields, is discussed by Fenton and Vanmarcke (1990) and compared with other existing methods in Fenton (1994).

4.6.2 Locally Averaged Random Fields

Definitions

A two-dimensional random field describes the behavior of a stochastic variable Z – such as Young's modulus or the elastic modulus C_{11} in (4.1) – over a two-dimensional surface with a coordinate system (x, y) or $\mathbf{x}$. Mathematically, a random field $Z(x, y)$

or $Z(\mathbf{x})$ is defined by its marginal and all its higher-order finite-dimensional probability density functions at all locations $\mathbf{x}$ [Lin, 1976]. In civil engineering applications, however, the random field description is usually limited to the specification of the univariate, or marginal, probability density function and the auto-correlation function. The (auto-)correlation function $R(\mathbf{x}_1, \mathbf{x}_2)$ is a measure for the relatedness between the field variable Z at two locations $\mathbf{x}_1$ and $\mathbf{x}_2$. A random field is homogeneous if $R(\mathbf{x}_1, \mathbf{x}_2)$ is invariant with respect to a shift in the origin. In this case, the mean $\mathrm{E}(Z(x))$, where $\mathbf{E}$ is the expected value operator, is location independent, and the auto-correlation function R depends only on the distance $\boldsymbol{\tau} = \mathbf{x}_2 - \mathbf{x}_1$ between the locations $\mathbf{x}_1$ and $\mathbf{x}_2$: $R(\mathbf{x}_1, \mathbf{x}_2) = R(\boldsymbol{\tau})$.

The moving local average field over a rectangular area $A = \ell_x \ell_y$ is defined as the random field $Z_A(x, y)$. The symbols are defined in Figure 4.8:

$$Z_A(x,y) = \frac{1}{A} \int_{x-\ell_x/2}^{x+\ell_x/2} \int_{y-\ell_y/2}^{y+\ell_y/2} Z(\xi,\eta) d\xi d\eta \tag{4.35}$$

This definition can be extended to an area A of arbitrary shape – where (x, y) is the centroid of the area A:

$$Z_A(x,y) = \frac{1}{A} \iint_A Z(\xi,\eta) dA \tag{4.36}$$

Variance Reduction Function

For a homogeneous random field, the mean is not affected by the averaging operation. The averaging process does, however, reduce the variance in general. The variance reduction function (VRF) γ relates the variance of the moving average field $\mathrm{Var}(Z_A)$

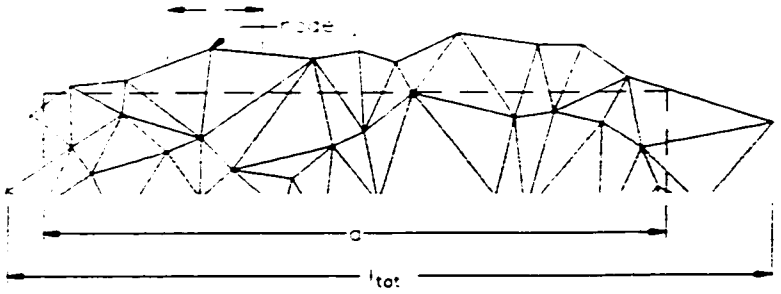

Figure 4.7: Computation of nodal forces, required for a force-based homogenization

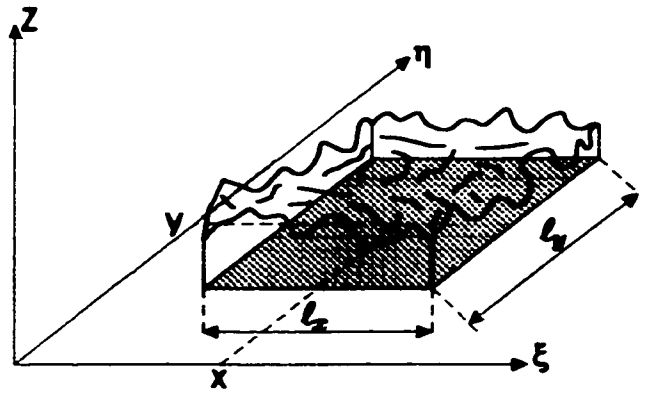

Figure 4.8: Local averaging of random field

to the original point variance $\mathrm{Var}(Z)$:

$$\gamma_A(x,y) = \frac{\mathrm{Var}\left(Z_A(x,y)\right)}{\mathrm{Var}\left(Z(x,y)\right)} \tag{4.37}$$

Since homogeneous random fields are invariant, statistically, to a shift in origin, the VRF depends solely on the averaging area A. The location (x,y) becomes irrelevant and can thus be dropped from the notation. Thus, the parameters describing the averaging area A are the only arguments for the VRF γ of a homogeneous random field Z. For rectangular areas $A = \ell_x \ell_y$, the following notation can then be introduced:

$$\mathrm{Var}\left(Z_{A=\ell_x\ell_y}\right) = \gamma\left(\ell_x,\ell_y\right)\mathrm{Var}\left(Z\right) \tag{4.38}$$

Correlation Function $R(x,y)$ and VRF γ

The VRF plays an important role in the theory of locally averaged random fields [Vanmarcke, 1983]. It allows one to evaluate the covariance of local averages of a homogeneous random field over two rectangular areas A and A' – overlapping or not – with sides parallel to the coordinate axes (see Figure 4.9a for a definition of the symbols):

$$\mathrm{Covar}\left(Z_A, Z_{A'}\right) = \frac{\mathrm{Var}(Z)}{4AA'}\sum_{k=0}^{3}\sum_{l=0}^{3}(-1)^{k+l}\,\Gamma\left(\ell_{1k},\ell_{2l}\right) \tag{4.39}$$

where $\Gamma(\ell_{1k},\ell_{2l}) = (\ell_{1k}\ell_{2l})^2\gamma(\ell_{1k},\ell_{2l})$.

For a homogeneous continuous random field the auto-correlation function R between two points of the random field Z depends only on the distance between those points. Consequently, the auto-correlation function R_A of the locally averaged random field Z_A depends on both the distance between and the size of the averaging areas. By choosing the intervals ℓ_{1k} and ℓ_{2l} as in Figure 4.9b, (4.39) generates an

expression for the auto-correlation function R_A of the two-dimensional field of local averages Z_A:

$$R_A(x,y) = \frac{1}{4(\ell_x \ell_y)^2} \begin{bmatrix} \Gamma(\ell_x + x, \ell_y + y) + \Gamma(\ell_x - x, \ell_y + y) \\ +\Gamma(\ell_x + x, \ell_y - y) + \Gamma(\ell_x - x, \ell_y - y) \\ -2\Gamma(\ell_x, \ell_y + y) - 2\Gamma(\ell_x, \ell_y - y) \\ -2\Gamma(\ell_x + x, \ell_y) - 2\Gamma(\ell_x - x, \ell_y) + 4\Gamma(x,y) \end{bmatrix} \tag{4.40}$$

In the limit for $\ell_x, \ell_y \to 0$, one obtains the relationship between the "generalized" VRF γ – there is no longer an averaging area – and the auto-correlation function $R(x,y)$ of a continuous homogeneous 2-dimensional random field, which depends on the lag (x,y) only. In the limit for $\ell_x, \ell_y \to 0$, the finite difference expression (4.40) for R_A transforms into the following fourth-order partial derivative [Vanmarcke, 1983]:

$$R(x,y) = \tfrac{1}{4} \frac{\partial^4}{\partial x^2 \partial y^2} \left(x^2 y^2 \gamma(x,y) \right) \tag{4.41}$$

Scale of Fluctuation and Auto-Correlation Function

For certain one-dimensional random fields, the VRF tends towards the following asymptotic expression when the averaging domain τ is sufficiently large:

$$\gamma(\tau) = \frac{\theta}{\tau}, \text{ for } |\tau| \to \infty \tag{4.42}$$

where the constant θ is defined as the scale of fluctuation. It can be shown that the scale of fluctuation θ is finite only if the "first moment" of the autocorrelation function is finite [Vanmarcke, 1983], which requires that:

$$\tau R(\tau) = 0, \text{ for } |\tau| \to \infty \tag{4.43}$$

In that case, the scale of fluctuation θ can also be computed from the 1D auto-correlation function $R(\tau)$:

$$\theta = \int_{-\infty}^{\infty} R(\tau)d\tau = 2\int_{0}^{\infty} R(\tau)d\tau \tag{4.44}$$

Similarly as for 1D fields, for 2D locally averaged random fields the characteristic area α is defined as:

$$\gamma(x,y) = \frac{\alpha}{xy}, \text{ for } |x|, |y| \to \infty \tag{4.45}$$

which yields a finite value for α only if the correlation R decays sufficiently rapidly in all directions (4.43). For multidimensional random fields, a scale of fluctuation can be defined in any direction using (4.42) where τ is defined as the averaging domain in this direction.

The correlation structure is said to be separable when the multidimensional VRF can be expressed as a product of one-dimensional VRFs [Vanmarcke, 1983]. For the 2D case:

$$\gamma(x,y) = \gamma_1(x)\gamma_2(y) \tag{4.46}$$

In this case the characteristic area α is defined as the product of the directional scales of fluctuation θ_x and θ_y:

$$\alpha = \theta_x\theta_y \tag{4.47}$$

4.6.3 Application to Micromechanical Model

Using any of the homogenization approaches in Section 4.5, it is clear that if the microgeometry is generated from a Poisson point process, the random fields for the material properties of the equivalent homogeneous continuum will be homogeneous as long as the link stiffnesses are IID.

Repeated application of one of the homogenization techniques (4.20), (4.23) or (4.34) to a large random sample of micro-structures generates the elastic moduli C_{ij} of the equivalent homogeneous continuum approximation in equation (4.1) as a moving locally averaged random field. These values can be considered "structural" averages of the individual stiffness of the discrete constituents in the heterogeneous micro-structure [Ostoja-Starzewski, 1994b].

The one-dimensional probability densities for C_{ij} are obtained from the histograms, obtained using Monte Carlo simulations. When this procedure is now repeated for different averaging area sizes and shapes, the variance reduction function γ can be estimated from the resulting data. The auto-correlation function $R(x, y)$ can then be derived from this VRF by means of equation (4.41). The approach will be illustrated for both a macroscopically isotropic and a orthotropic micro-mechanical model in the next Chapter.

The homogenization procedure defines the equivalent continuous random fields $C_{ij}(x, y)$, $i, j = 1 \ldots 3$, based on the discrete microstructure. The auto-correlation function R, obtained in this manner, must be interpreted carefully. It may seem that R gives the correlation between the values for C_{ij} in any 2 points. This is only apparently so, since the assumptions underlying equation (4.41) are satisfied only when sufficiently large averaging areas, i.e. larger than the RVE, are considered. Otherwise, the discrete system can not be homogenized in a statistical sense and the discrete micro-mechanical model itself should be used in a structural analysis. The result for R in equation (4.41) as an auto-correlation function between 2 points must therefore be interpreted as a limiting case and merely serves as a mathematical tool to compute the covariances and cross-covariances for other than rectangular

averaging areas, as needed for a FE analysis.

This distinction is of theoretical interest only as long as only the macroscopic behavior is of interest, but becomes important when a detailed study of local effects, such as crack propagation, is the goal of the structural analysis. The homogenization procedure blends the discrete and continuum mechanics and allows for a smooth transition between the study of global and local effects. This is the major difference between this "meso-continuum" resulting from a stochastic homogenization procedure and the "classical" continuum. It is a direct result of the discrete nature of the micro-structure, which invalidates the use of limits such as equation (4.16).

The necessity to introduce an assumption about the strain or stress distribution along the window boundaries has implications on the subsequent FE analysis. For the structural analysis of the equivalent homogeneous continuum to be fully consistent with the discrete micro-mechanical model, the assumed strain state and boundary deformations – expressed through [B] in (4.20) for instance – must be compatible with the shape functions of the finite elements [Ostoja-Starzewski, 1993]. Only triangular constant strain elements are consistent with the assumptions made for the derivation of the homogenization equations (4.20), (4.23) or (4.34).

4.7 Modeling Window Boundaries

The boundaries of the selected window A (Figure 4.6) require careful modeling before the micro-structure is homogenized. Three solutions can be distinguished:

1. Periodic boundary conditions. They allow to select a unit cell from a periodic macrostructure. Randomly periodic models are useful in the analysis of matrix-

inclusion composite models or reticulate structures.

2. Those links, which intersect with the window boundary, are cut. The advantage of this method is that it is easy to see how multiple small windows constitute a larger area without overlap. This is particularly convenient when a random field simulation technique based on local average subdivision is used [Fenton and Vanmarcke, 1990].

3. The averaging window is adjusted to a polygon shaped area (see Figure 4.6) in order to prevent the cutting of any links. This method has the advantage that both the stresses and strains can be controlled at the window boundary, which allows us to compare the different homogenization techniques.

When a randomly periodic model is used, the homogenization process connects the material microstructure to an equivalent continuum through periodic boundary conditions, which is shown in Figure 4.3 [Graham and Baxter, 1999]. However, this geometric periodicity is not appropriate for materials with truly random microgeometry such as concrete [Ostoja-Starzewski and Wang, 1990].

When the links are cut at the window boundaries, only displacement-based homogenization techniques can be used. Figure 4.10 compares the average elastic moduli obtained through homogenization using the second and third approach. It can be concluded that both approaches give very similar results for the average elastic properties.

However, cutting the links at the window edges may introduce "stray" links, shown in Figure 4.11. When a link is not connected to any other links, an arbitrary small value for the network stiffness can be obtained in the homogenization process:

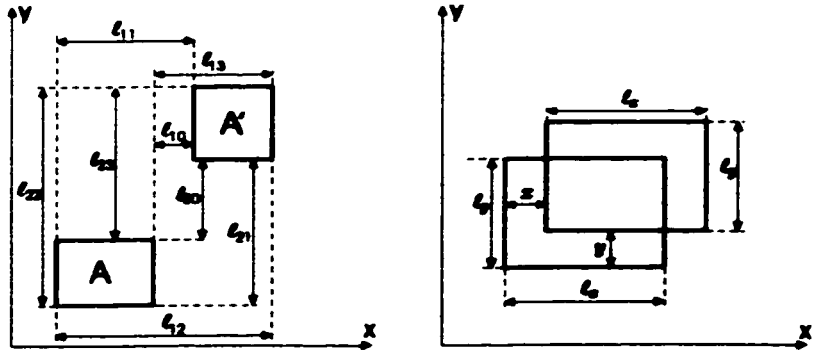

Figure 4.9: Definition of distances needed to evaluate the covariance function

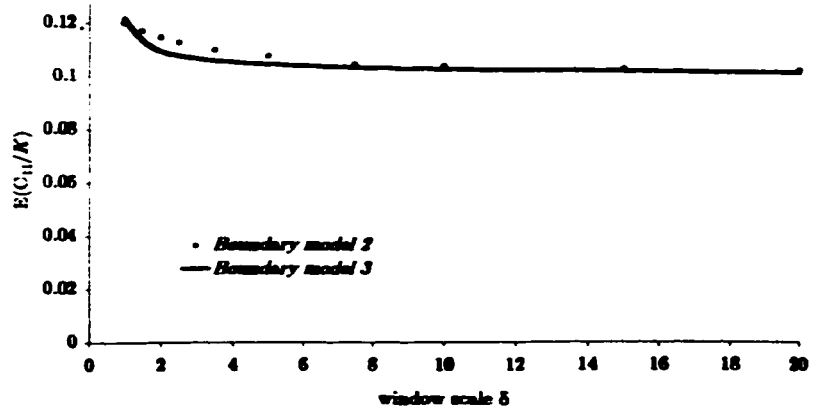

Figure 4.10: Impact of the boundary modeling technique on the average values of the elastic material properties

in the sample network in Figure 4.11, C_{22} is almost equal to zero for homogenization window 1 on the left. Stray links usually occur in the corners of the homogenization window only as in window 2 in Figure 4.11. For small averaging windows, however, they may make up the entire network, an example is window 3 in Figure 4.11, and produce incorrect values for the equivalent stiffness.

The arbitrary stiffness values obtained for such windows increase the variance of the elastic moduli in Monte Carlo simulations of the microstructure. Since this error in the variance is larger for small homogenization windows than for large windows, the variance reduction function will be biased.

This increased variance adversely affects the estimation of the autocorrelation function. Locally averaged random field theory predicts that the product $A\mathrm{Var}\,(C_{ij})$ becomes constant for large A, depending on the auto-correlation structure in the random field. The detailed conditions are given in Vanmarcke (1983) and are discussed in the next section. A comparison of $A\mathrm{Var}\,(C_{11})$ as a function of the window size for boundary model types 2 and 3 is shown in Figure 4.12. The graph clearly indicates the increased variance using boundary model 2 which is obtained for small averaging windows. It then follows from locally averaged random field theory (4.41) that the auto-correlation function for both boundary condition models must be different.

The boundary effect, which is caused by cutting the links, decreases as the window size A increases. Figure 4.12 shows that both boundary models converge for large window areas. It can be concluded that cutting the links at the window boundaries should be avoided for small averaging areas because it significantly alters the correlation structure of the random field [C].

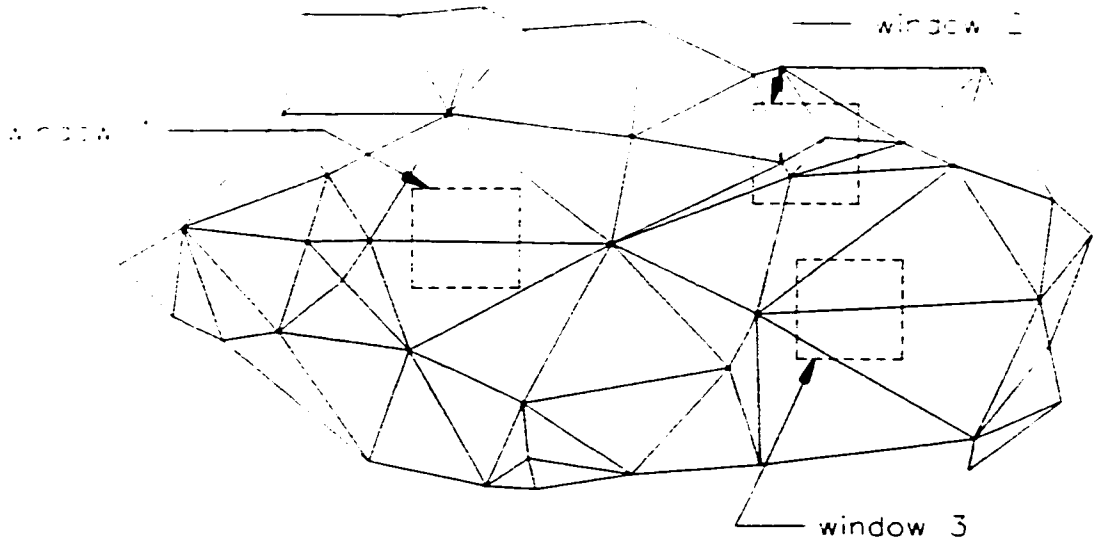

Figure 4.11: Networks with stray links

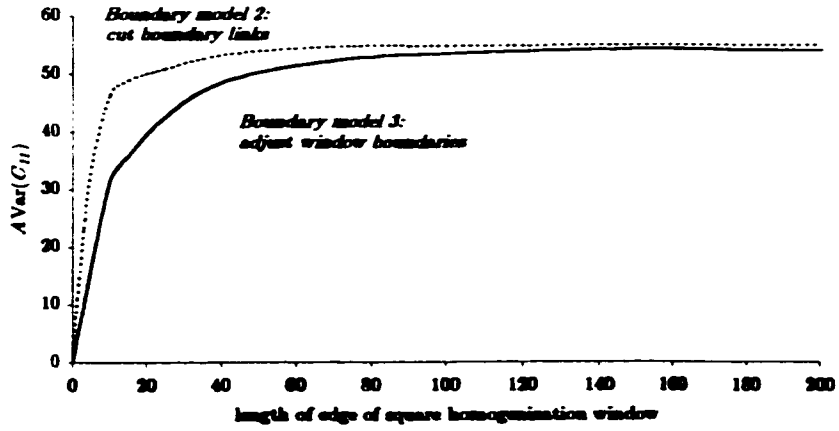

Figure 4.12: Impact of boundary modeling on correlation structure

The third approach is used by Gasparini et al. (1996) to analyze the force-displacement behavior of brittle Voronoi-Delaunay lattices, subject to axial load only. The Delaunay network is obtained as follows [Okabe et al., 1992]. Given a set of n distinct nodes in the plane, the area is subdivided into n cells. Each cell around a node contains all points in the plane, which are closer to this particular node than to any other node. This is illustrated in Figure 4.14 where the center of each of the granulates in the actual microstructure is a generator point for the Voronoi diagram. The lattice model, which connects all nodes with their neighbors is known as the Delaunay triangulation. Efficient algorithms are described in Joe and Simpson (1986) and Field (1991) , FORTRAN routines are given in Joe (1991). Gasparini et al. (1996) analyze Delaunay lattices, where the nodes are given by uniform Poisson point process [Getis and Boots, 1978].

In Gasparini et al.'s (1996) study, only links which are fully inside the area are included in the network. Displacements are prescribed for nodes within boundary strips (see Figure 4.13) at the top and bottom of the square specimens. The width of the boundary strips is equal to the mean spacing of the nodes. When the network is based on a uniform Poisson point process with a point density of λ nodes per unit area, this boundary strip width is thus equal to $1/\sqrt{\lambda}$.

A drawback of this modeling is that the resulting network is not always stable. Our simulations have shown that omitting the links which intersect the window boundary may result in the formation of a network in which one or more triangles are connected to the rest of the network by one node only. This results in a singular stiffness matrix. To avoid this problem, the following improved technique is suggested in this dissertation: the links which are part of triangles intersecting the window

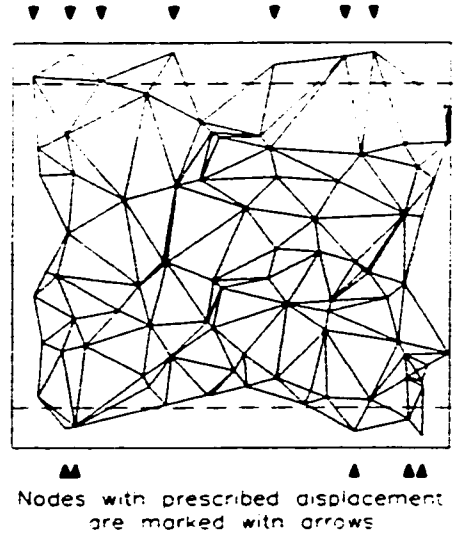

Figure 4.13: **Boundary modeling using boundary strips, as suggested by Gasparini et al. (1996)**

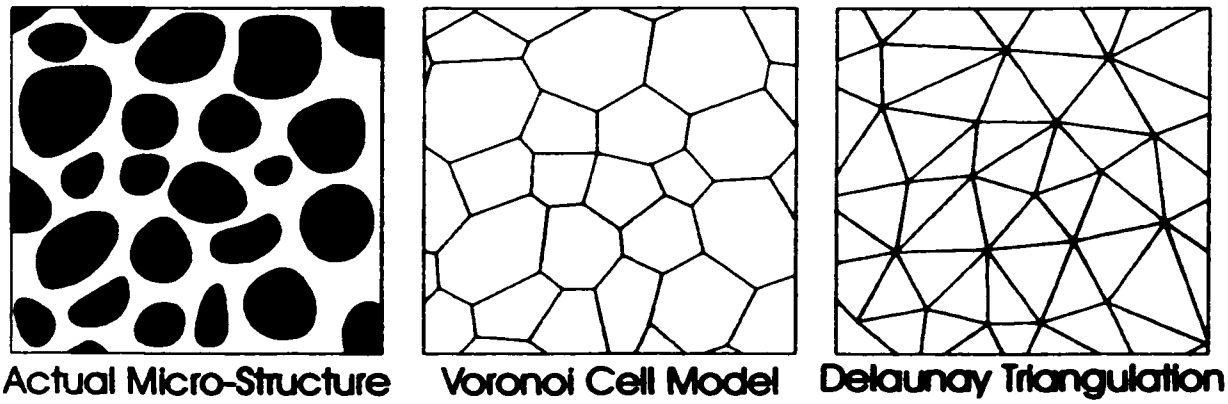

Figure 4.14: **Micromechanical modeling of a material**

boundary are included in the homogenization process and the displacements are prescribed for all nodes outside the window boundary. The final network is now no longer obtained by omitting links, but by adding pairs of links, which form a new triangle. This procedure guarantees that the stiffness matrix of the resulting truss model is always positive definite.

Because of the randomness of the lattice model, the boundary nodes are not evenly distributed along an edge. As a result, depending on the distribution of the boundary nodes along the edge, prescribing the deformation of the nodes in such a boundary strip might be a poor model of a constant displacement along that edge when the boundary modeling technique of Gasparini et al. (1996) is used. This is the case at the bottom of the sample network shown in Figure 4.13. Because the nodes are concentrated near both ends, prescribing a zero displacement at the 5 nodes in the bottom strip is not an accurate modeling of a fixed bottom side of the square panel. Consequently, the boundary modeling, which is used by Gasparini et al. (1996) is not always an accurate reflection of the boundary conditions of the continuum. Because the node spacing has a much lower probability of being large in the newly suggested boundary model, this is no longer a problem when the improved boundary model is used.

The shortcomings of Gasparini et al.'s (1996) boundary model become apparent in simulations of rectangular or square specimens, which are subject to a vertical strain while lateral extension is prevented. A sample network and its deformed state are shown in Figure 4.15. The total horizontal reaction force, F_x, along the vertical side of the network and the total vertical reaction force, F_y, along the bottom of the network are calculated for 4000 Monte Carlo sample networks. Table 4.1 shows that

Specimen size ($w \times h$) (density $\lambda = 0.01$)	Boundary strip model		New boundary model	
	$\rho(n_{strip}, F_x)$	$\rho(n_{strip}, F_y)$	$\rho(n_{strip}, F_x)$	$\rho(n_{strip}, F_y)$
100×100	0.304	0.411	0.133	0.215
100×300	0.284	0.292	0.083	0.096
250×250	0.213	0.312	0.087	0.116
250×750	0.246	0.259	0.079	0.088

Table 4.1: Estimated correlations between the number of nodes in boundary strip and the total reaction force along an edge (standard error less than 0.02)

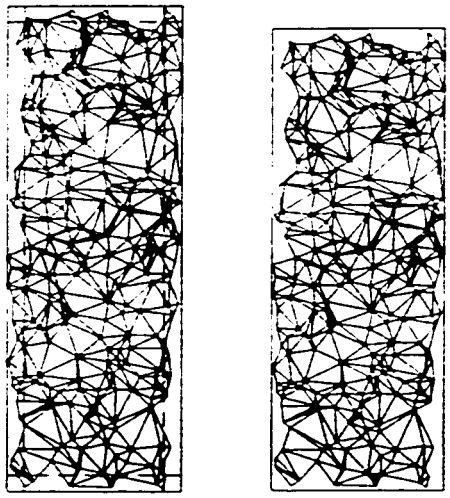

Figure 4.15: Sample compression test used to assess the quality of the boundary modeling

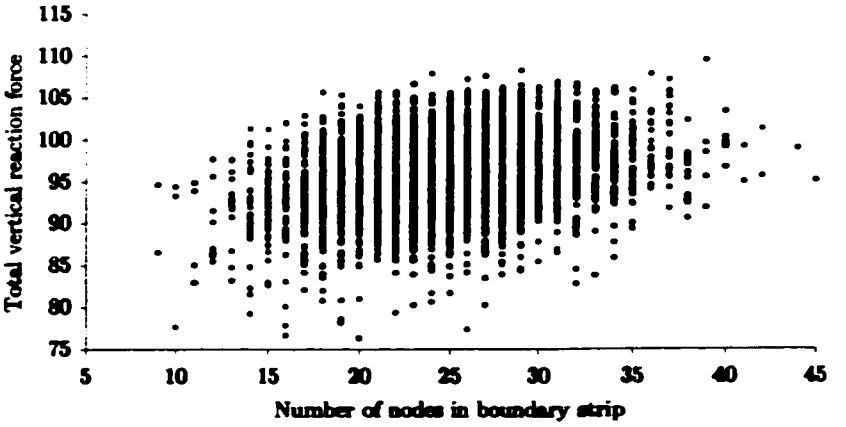

Figure 4.16: **Correlations between n_{strip} and F_y using boundary model by Gasparini et al. (1996) obtained from 4000 Monte Carlo simulations on square specimens** 250×250

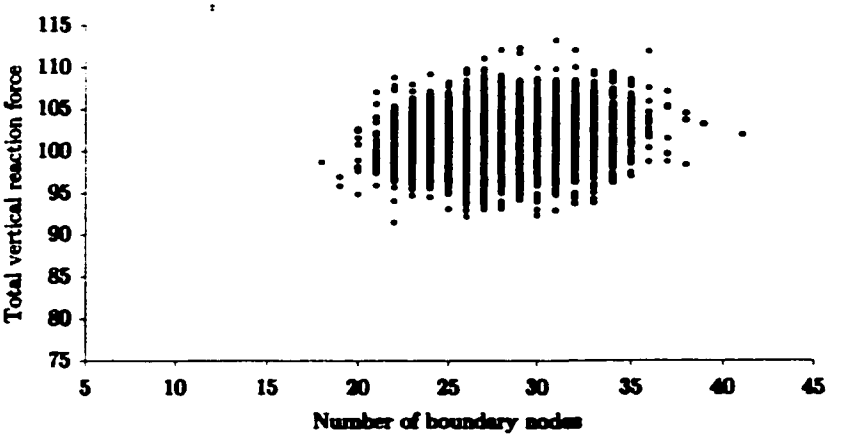

Figure 4.17: **Correlations between n_{strip} and F_y using suggested improved boundary model obtained from 4000 Monte Carlo simulations on square specimens** 250×250

there is a significant correlation between the number of nodes in the boundary strip and the total force along a side. This correlation becomes increasingly important for smaller averaging windows. The smaller reaction forces obtained in the samples which have less boundary strip nodes introduce severe bias in the overall probability distribution of the network stiffness, which becomes negatively skewed (Figure 4.18). The correlation would disappear if the boundary strip width is increased, but this, in turn, affects the overall structural behavior of the network. In that case the stiffness of the network would be overestimated since the displacements would be prescribed for most of the nodes. This would bring us closer to effectively using (4.23) for homogenization instead of the intended use of (4.20).

The previously suggested improved boundary modeling significantly reduces this correlation as shown in Table 4.1. Comparison of Figure 4.16 and Figure 4.17 indicates that this improvement can at least partially be attributed to a reduced variance in the number of boundary nodes. Figure 4.18 shows that the variability of the reaction forces is overestimated in the Gasparini-model because of the long lower tail.

Another advantage of the suggested boundary modeling technique is that the displacements of the internal nodes are in no way affected by the boundary modeling because the new model does not require to prescribe the displacements on any additional nodes. Note that the actual homogenization area is no longer equal to A, but this is easily taken into account by calculating the exact area of the polygon (Figure 4.6).

4.8 Summary

A framework for homogenization of discrete, heterogeneous microstructures into homogeneous continua is presented in this Chapter. The discrete and continuum model are said to be equivalent if the strain energy stored in the material under the same uniform boundary conditions is identical for both models. Expressions for the material properties of isotropic materials with a regular microgeometry are derived.

For a discrete microstructure with random geometry the elastic material properties of the equivalent continuum can be calculated on the basis of either strain or stress-based boundary conditions. Existing strain-based techniques are reviewed and a new, stress-based homogenization procedure is introduced.

The homogenization algorithm requires the specification of boundary conditions, which require careful modeling. Several boundary model types are reviewed. It is shown that cutting the links at the window boundaries increases the variance. The effect is particularly pronounced for small homogenization windows. It is concluded that the auto-correlation function of the random field cannot be estimated accurately when the links are cut at the window boundaries.

The shortcomings of omitting the links which intersect the window boundary are illustrated. The resulting network is not necessarily stable and the boundary conditions may be poorly modeled in networks with high geometric randomness. It is demonstrated how including the links which intersect the window boundary in the network guarantees that the resulting network is stable. This technique also significantly improves the boundary modeling.

The random field characteristics of the material properties of the equivalent con-

tinuum can be estimated using locally averaged random field theory. Some important features of the locally averaged random field theory are reviewed. The mean and standard deviation of the elastic properties for any given window can be estimated by means of a Monte Carlo simulation of the microstructure and subsequent homogenization thereof. The variance reduction function (VRF) can be estimated through a repetition of the Monte Carlo simulation procedure for different window areas and aspect ratios. The locally averaged random field theory gives the relationship between the VRF and the auto-correlation function of the continuous random field.

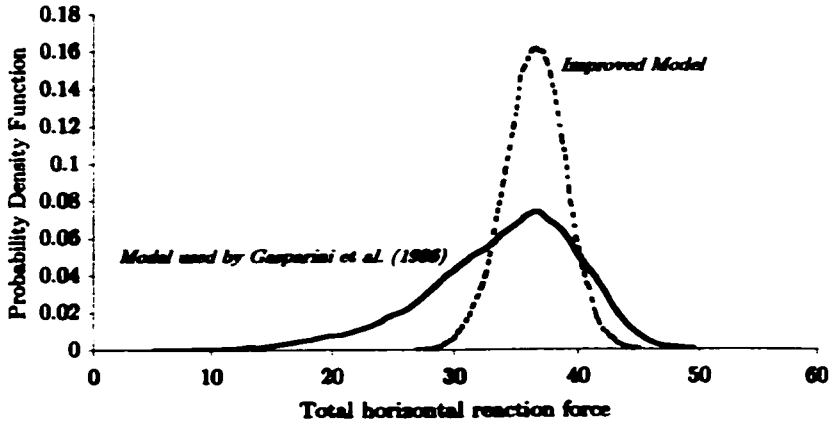

Figure 4.18: PDF of the horizontal reaction force F_x, obtained using 4000 Monte Carlo simulations (specimen size: 100 × 100)

Chapter 5

Consistent Macro Random Fields in Structural Analysis

5.1 Introduction

In this chapter, the framework, which was presented in Chapter 4 to model the random field characteristics of equivalent continuum elastic properties, is applied to different microstructures. Some of the interesting features of the resulting macro random fields are highlighted and the significance for structural reliability applications is demonstrated by means of examples. The response statistics obtained from an SFEM analysis based on micromechanically consistent random fields of the material properties are compared with the results of an SFEM analysis where only Young's modulus is modeled as a random field.

The impact of the uncertainties associated with the stiffness of the linear elastic micromechanical model on the statistics of the homogenized continuum are assessed. The dependence of the random field material properties on the characteristics of the discrete spatial random field, which defines the microgeometry, is illustrated. The accuracy and computational efficiency of the three different homogenization techniques, which were presented in Chapter 4, are compared with each other.

5.2 Features of Consistent Macro Random Fields

5.2.1 Uniform Poisson-Delaunay Microstructure

Several important conclusions can be drawn regarding specific features of the continuous random field describing the macroscopic equivalent continuum. Consider first the results for the expected value and standard deviation of [C]. It follows directly from the micro-mechanical constitutive law (4.8) that $\mathbf{E}([\mathbf{C}])$ varies with $\mathbf{E}(K)/\mathbf{E}(\ell)$ (to first order). Since the mean link length $\mathbf{E}(\ell)$ is $\sqrt{\lambda}$, $\mathbf{E}([\mathbf{C}])$ depends on $\mathbf{E}(K)\sqrt{\lambda}$.

This is easily understood when visualizing the limiting case without any variability and where the λA nodes are evenly distributed in space: the lattice network then becomes a chain of parallel bar systems where all links have stiffness K/ℓ and the total stiffness of such a network is K/ℓ. The standard deviation of [C] increases slower with λ than $\mathbf{E}([\mathbf{C}])$ does, which implies that COV([C]) decreases as a function of λ for constant K. The dependence of $\mathbf{E}(C_{11})$ and StDev(C_{11}) on the density of the nodes λ is shown in Figure 5.1.

Note that, in a practical application, the density λ is determined from the microstructure through image analysis [Russ, 1995] and, consequently, it should not be considered a variable parameter in the analysis. The parameter K is selected such that the stiffness of the network model, obtained using the homogenization procedure, corresponds with the experimental macroscopic stiffness data available.

Analysis of the sample elastic moduli C_{ij}, obtained by homogenization of Monte Carlo simulated microstructures, suggests that a multivariate joint normal distribution fits the 6 elastic moduli C_{ij} quite well. The marginal normal probability plots

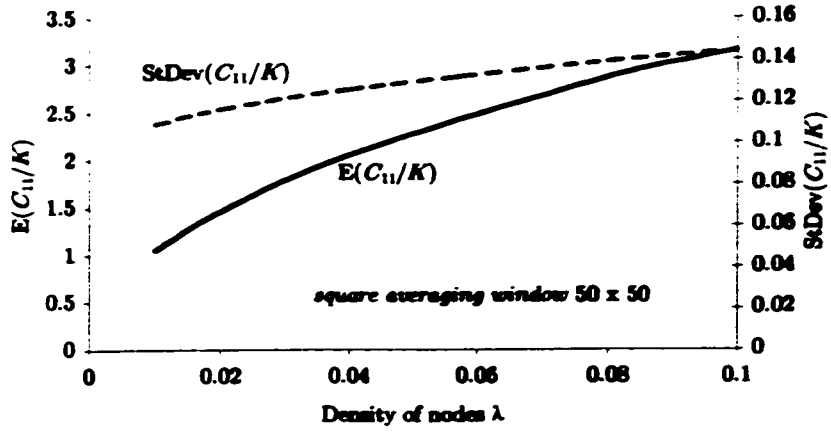

Figure 5.1: Dependence of $\mathbf{E}(C_{11})$ and $\mathrm{StDev}(C_{11})$ on the density of the nodes λ for constant stiffness K and window size 50×50

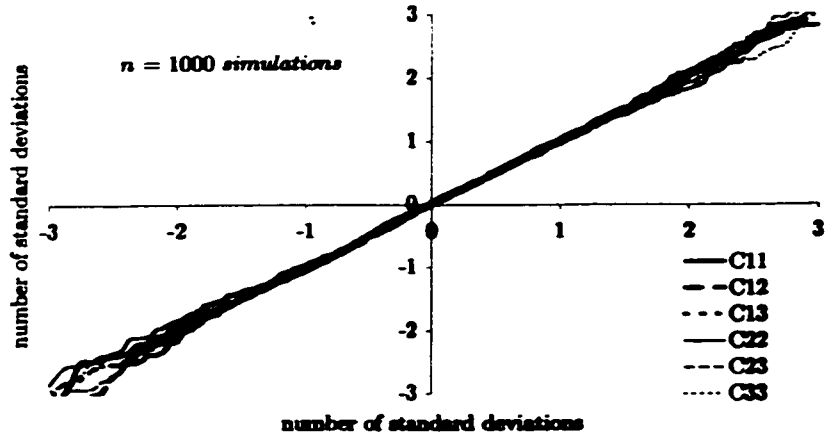

Figure 5.2: Normal probability plots for C_{ij} (window size 100×100, nodal density $\lambda = 0.01$)

for two different averaging window sizes are given in Figure 5.2 and Figure 5.3. It can be concluded that the quality of the Gaussian distribution model deteriorates as the homogenization window becomes smaller. This can be explained as follows. When the size of the homogenization window decreases, the variance of C_{ij} increases. When the variance of C_{ij} increases, negative values become possible when a Gaussian distribution model is used. However, the elastic moduli C_{11}, C_{12}, C_{22} and C_{33} are all non-negative. As a result, the average value for C_{11} increases for small areas A (see Figure 5.4), which indicates that [C] can no longer be considered a homogeneous random field for small A. Note that Figure 5.3 indicates that the quality of the Gaussian model is still quite good for C_{13} and C_{23}.

Appropriate truncation of the Gaussian distribution can, to some extent, solve this problem. In this context, it is important to understand that the small homogenization windows have limited practical use. With the selected nodal density $\lambda = 0.01$, a 10×10 window contains on average only 1 internal node and approximately 10 links. This window is actually smaller than the RVE: insufficient microconstituents are available for this medium to be statistically homogeneous [Hashin, 1983]. The non-normality problem rapidly vanishes as the window size increases. From the simulation results it can be concluded that, for the selected nodal density $\lambda = 0.01$, the size of the RVE is approximately 30×30 for this type of microstructure. Only windows of at least this size are large enough for the microstructure to be statistically homogeneous. Figure 5.4 indicates that the average is practically invariant for window sizes larger than 30×30.

The normal distribution model appears for other microstructures as well. Based on a homogenization using the Generalized Methods of Cells, Graham and Baxter

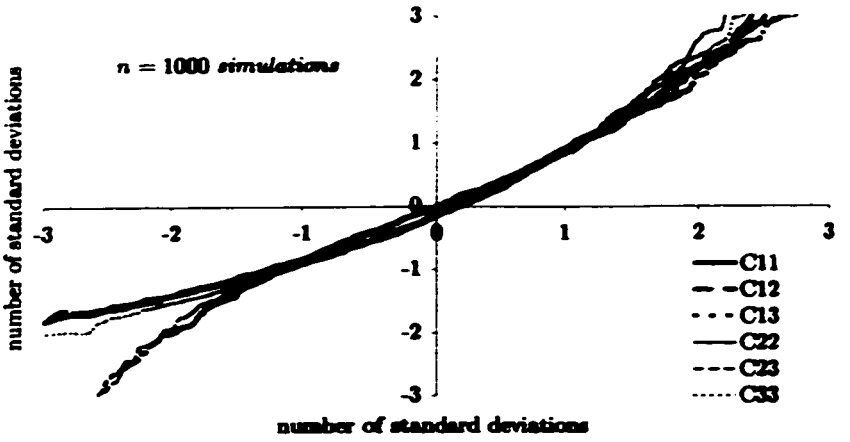

Figure 5.3: Normal probability plots for C_{ij} (window size 10×10, nodal density $\lambda = 0.01$)

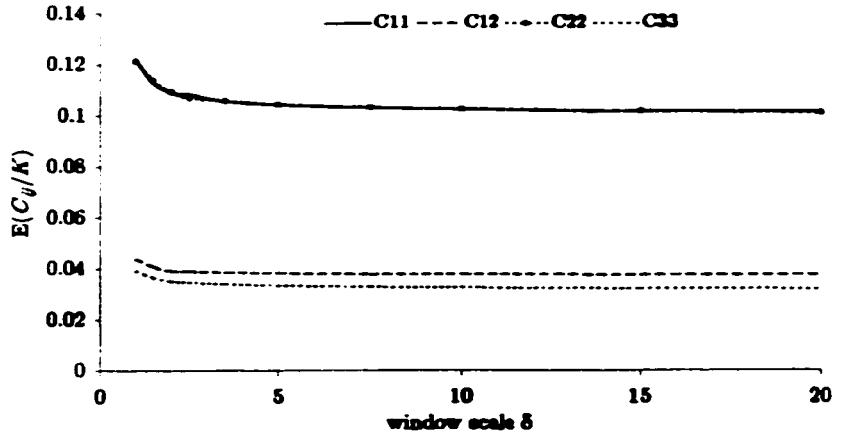

Figure 5.4: Expected value of the elastic moduli C_{ij} as a function of the homogenization window size.

(1999) observe that a Gaussian distribution models the Young's modulus of fiber-reinforced composite materials very well, as long as the homogenization area is not too small.

In structural reliability applications, not only the variability around the mean value but also the tail behavior is very important [Maes and Huyse, 1995]. The Gumbel plot in Figure 5.5 of the Monte Carlo data for C_{ij} and the fitted Gaussian model illustrates that a good fit of the lower tail of the elastic modulus C_{11} is obtained. This ensures an adequate prediction of extreme responses, such as maximum deformations, in structural analysis [Huyse and Maes, 1999b].

For a density $\lambda = 0.01$, Figure 5.4 shows that $\mathbf{E}([\mathbf{C}])$ rapidly becomes independent of the size of the averaging window A. The results, obtained for a square window $A = 100 \times 100$ (scale $\delta = \sqrt{\lambda A} = 10$) with $K = 10$ using 6,000 Monte Carlo samples, are given below:

$$\mathbf{E}([\mathbf{C}]) = \begin{bmatrix} 1.033 & 0.385 & 0.000 \\ & 1.035 & 0.000 \\ sym & & 0.324 \end{bmatrix} \tag{5.1}$$

$$\mathbf{StDev}([\mathbf{C}]) = \begin{bmatrix} 0.075 & 0.025 & 0.028 \\ & 0.075 & 0.028 \\ sym & & 0.020 \end{bmatrix} \tag{5.2}$$

The standard error on these estimates is less than 0.001 for $\mathbf{E}([\mathbf{C}])$ and 0.0001 for StDev([C]). The lattice-type microstructure in this example is expected to be isotropic since the density of the node-generating Poisson point process is uniform. For isotropic materials, the plane stress constitutive equation (4.1) in classical con-

tinuum mechanics is a function of just two properties: Young's modulus E and Poisson's ratio ν and the resulting elasticity matrix [C] is given in (4.5). Comparison of (4.5) with the numerical result obtained in (5.1) indicates that the classical result for the elasticity matrix [C] is a good approximation of the average behavior.

However, the results obtained in (5.2) indicate that a straightforward randomization of (4.5) would not be consistent with the micromechanical model. Indeed, even if E and ν are both considered random fields, C_{13} and C_{23} will still be zero (deterministically). This does not correspond to the second-moment information of C_{13} and C_{23} given in (5.2), which indicates zero mean but a non-zero standard deviation. Another interesting result is that the coefficients of variation for the shear (C_{12} and C_{33}) and axial (C_{11} and C_{22}) stiffness are practically the same: approximately 7% in this example.

For square averaging windows, the correlation between two elastic moduli C_{ij} and C_{kl} is practically independent of the scale δ, for a window larger than the RVE: $\delta \geq 3$ or window size larger than 30×30. These constant correlation coefficients, as obtained from 6,000 Monte Carlo simulations for a square homogenization window with scale $\delta = 10$, are:

$\rho_{C_{ij}C_{kl}}$	C_{11}	C_{12}	C_{13}	C_{22}	C_{23}	C_{33}
C_{11}	1	0.470	0.001	-.002	-.002	0.463
C_{12}		1	-.002	0.472	-.005	0.765
C_{13}			1	-.009	0.661	-.010
C_{22}				1	0.002	0.428
C_{23}			*sym*		1	-.015
C_{33}						1

(5.3)

The standard error on these estimates is obtained using bootstrap resampling ($B = 1000$ bootstrap samples are used) [Efron and Tibshirani, 1993] and is less than 0.017 for all correlation coefficients. Interestingly, these correlations are also quite different from those obtained using a straightforward randomization of equation (4.5). More specifically:

1. The correlation between C_{11} and C_{22} is practically zero in the micromechanical model (5.3), whereas randomization of E and ν in equation (4.5) would result in perfect correlation between C_{11} and C_{22}. It can be concluded that a lattice with this type of random microstructure is isotropic in the mean only. For finite averaging areas, the material is stochastically anisotropic. According to (5.3), there is no correlation between the stiffnesses in different directions: $\rho_{C_{11}C_{22}} \approx 0$. This automatically follows from the uniform density of the nodes over the window.

2. According to the micromechanically based homogenization technique, the correlation between either C_{12} or C_{33} and either C_{11} or C_{22} should be in the range

0.4-0.5, whereas use of (4.5) leads again to a perfect correlation coefficient of 1 if only E is assumed to be a random field.

3. Only the correlations between C_{13} or C_{23} and any of the other elastic moduli C_{ij} are basically zero for both approaches. A large correlation coefficient is obtained between C_{13} and C_{23}. Both of these moduli are deterministically zero when (4.5) is randomized.

4. A high correlation is observed between the shear moduli C_{12} and C_{33} in the micromechanical model. Use of (4.5) implies a perfect correlation if only E is modeled as a random field.

The VRF γ expresses how the variance of the moving average field reduces with respect to the original point variance as a function of the averaging window size. The correlation function R is related to the VRF γ through equation (4.41). Using Monte Carlo simulations, the variances and covariances of the elastic moduli C_{ij} can be estimated for different rectangular areas $A = \ell_x \ell_y$ and different aspect ratios ℓ_x/ℓ_y. A VRF can be estimated for each of the variances and covariances of the elastic moduli C_{ij}.

In general, a very good agreement between the Monte Carlo data and the following separable VRF-model is obtained:

$$\gamma(\ell_x, \ell_y) = \left[1 + \left(\frac{\ell_x}{\theta_x}\right)^m\right]^{-1/m} \left[1 + \left(\frac{\ell_y}{\theta_y}\right)^n\right]^{-1/n} \tag{5.4}$$

where θ_x, θ_y are the scales of fluctuation in x and y-direction and m, n are constant model parameters. When m, n are larger the product $A\gamma$ approaches its asymptote, i.e. the characteristic area $\theta_x \theta_y$, faster for smaller values of ℓ_x and ℓ_y than when m

and n are small. The quality of the fit of the VRF model to the Monte Carlo data for the variance of C_{11} and the covariance between C_{11} and C_{12} is given in Figure 5.6.

The VRFs for C_{11} and C_{22} are direction dependent: $\theta_x \neq \theta_y, m \neq n$. Because the geometry is statistically homogeneous and thus orientation-independent, the VRF parameters are interchangeable between the equations: $\theta_{x,C_{11}} = \theta_{y,C_{22}}, \theta_{y,C_{11}} = \theta_{x,C_{22}}, m_{C_{11}} = n_{C_{22}}$, and $n_{C_{11}} = m_{C_{22}}$. Figure 5.8 shows that $\mathrm{Var}(C_{11})$ decreases faster in y-direction than in x-direction, and vice versa for $\mathrm{Var}(C_{22})$. This can also be derived from the contour plots of the autocorrelation function R in Figure 5.7.

The microstructure in this lattice model is based on a point process with uniform density and the stiffness parameter K in (4.8) is constant. Consequently, the random field is a so-called finite scale model [Fenton, 1999a], i.e. no significant correlation exists over large distances. The scale of fluctuation θ is of the same order of magnitude as the average link length ℓ_{avg} in the micromodel. This is illustrated in Figure 5.7: no significant correlation exists in the locally averaged field beyond neighboring elements.

The auto-correlation and cross-correlation functions of the elastic moduli C_{ij} are computed from the fitted VRFs using (4.41). Figure 5.7 shows that the auto-correlation structure of the axial moduli C_{11} and C_{22} are quite direction-dependent. The auto-correlations of the shear modes C_{12} and C_{33} are almost direction-independent.

5.2.2 Orthotropic Poisson-Delaunay Microstructure

In this section, the features of the macro random fields are obtained for an orthotropic material. Orthotropy is achieved by selecting the density of the nodes twice as

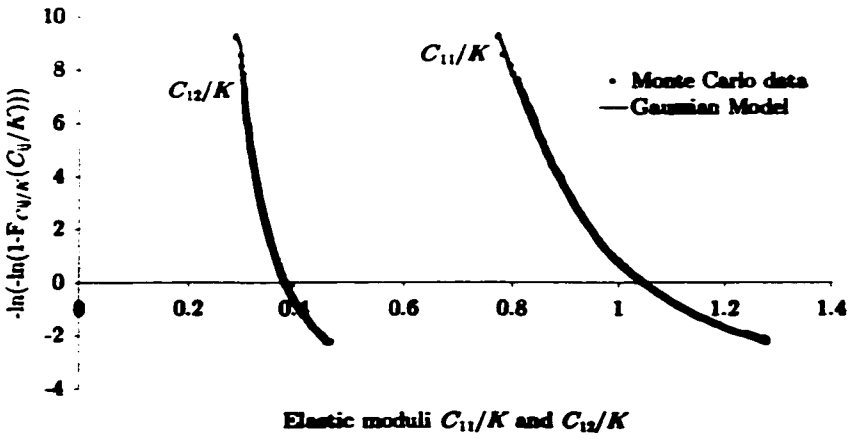

Figure 5.5: Gumbel plot for C_{11}/K and C_{12}/K (10,000 simulations, density $\lambda = 0.01$)

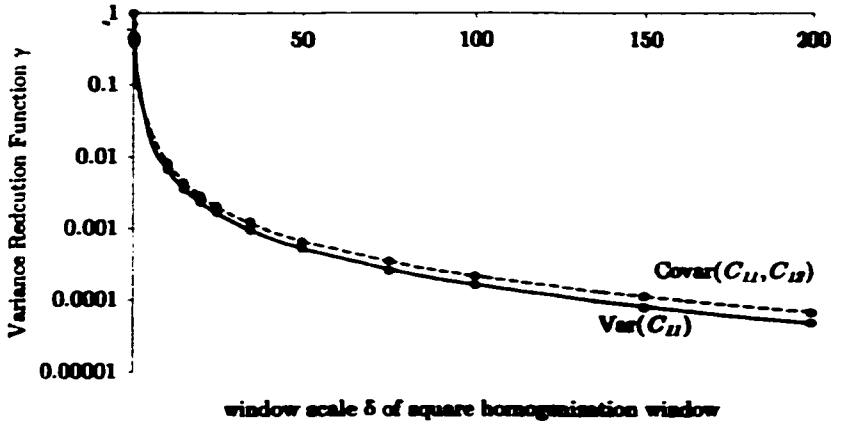

Figure 5.6: VRF of $\mathrm{Var}(C_{11})$ and $\mathrm{Covar}(C_{11}, C_{12})$ for square homogenization windows (dots indicate simulation results)

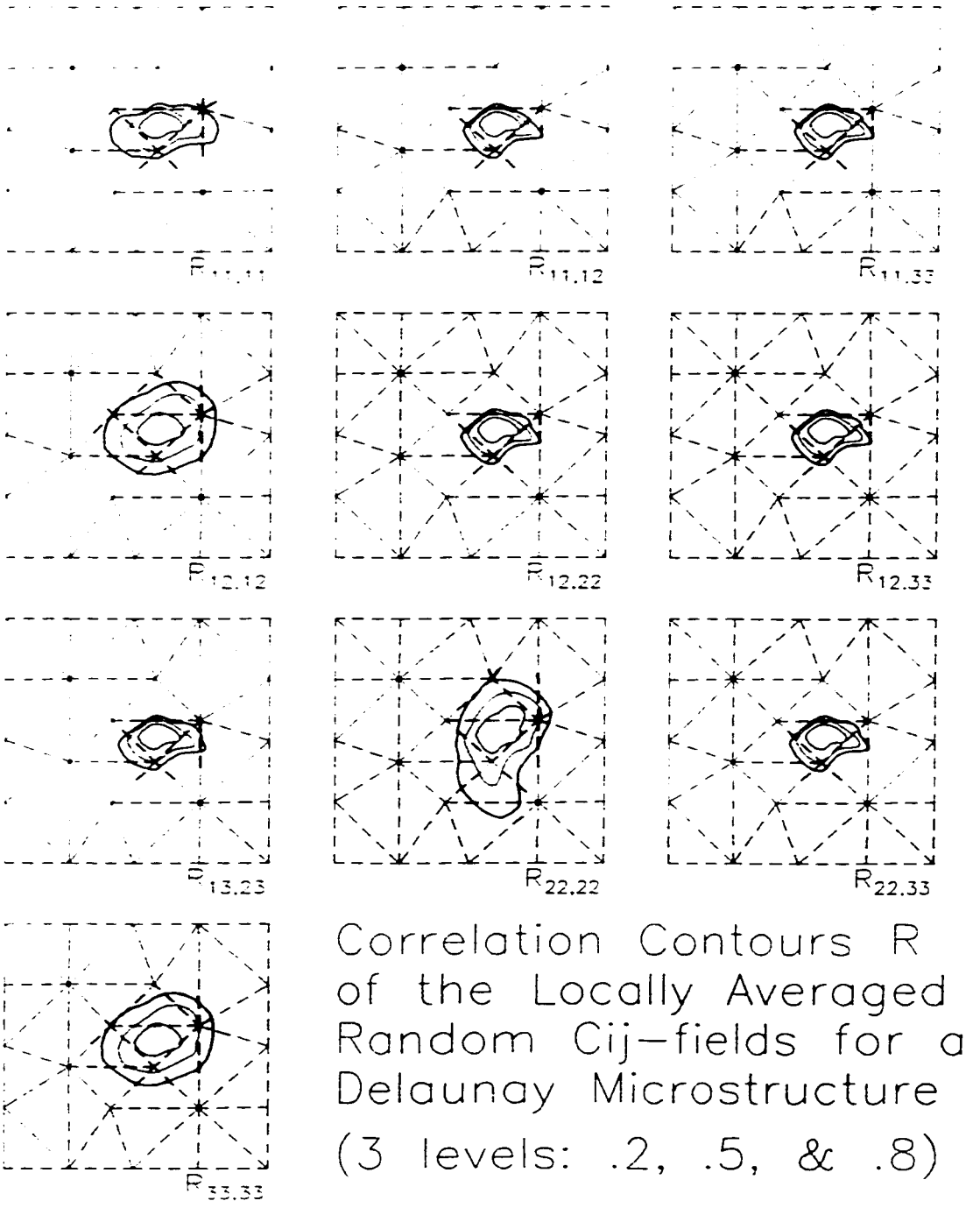

Figure 5.7: Iso-correlation contours for locally averaged random fields

high in the x-direction as in the y-direction. Figure 5.9 compares a sample of the orthotropic microstructure with an isotropic one. The summary statistics for the mean, standard deviation and correlation, as obtained from 1000 simulations on square homogenization windows 100×100, are given below:

$$\mathbf{E}([\mathbf{C}]) = \begin{bmatrix} 0.373 & 0.319 & 0.000 \\ & 2.035 & 0.001 \\ sym & & 0.263 \end{bmatrix} \tag{5.5}$$

$$\text{StDev}([\mathbf{C}]) = \begin{bmatrix} 0.033 & 0.021 & 0.017 \\ & 0.116 & 0.032 \\ sym & & 0.017 \end{bmatrix} \tag{5.6}$$

$\rho_{C_{ij}C_{kl}}$	C_{11}	C_{12}	C_{13}	C_{22}	C_{23}	C_{33}
C_{11}	1	0.382	-.038	-.049	-.018	0.393
C_{12}		1	-.069	0.508	-.005	0.634
C_{13}			1	-.013	0.545	-.020
C_{22}				1	0.018	0.231
C_{23}			*sym*		1	0.013
C_{33}						1

(5.7)

The standard error on these estimates is less than 0.004 for $\mathbf{E}([\mathbf{C}])$, 0.0006 for StDev([C]) and 0.033 for $\rho_{C_{ij}C_{kl}}$. The following conclusions can be drawn from this simulation:

1. Because the density of the nodes is higher in x-direction than in y-direction, the links are primarily oriented along the y-axis. As a result, the stiffness in y-

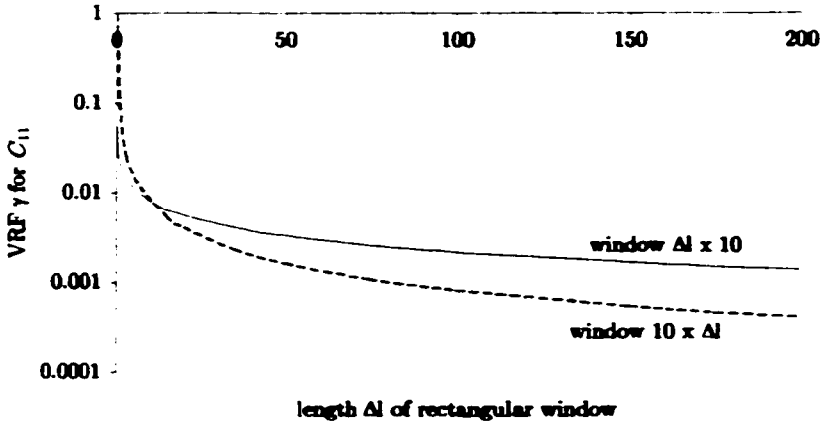

Figure 5.8: Directional dependence of VRF γ for C_{11}

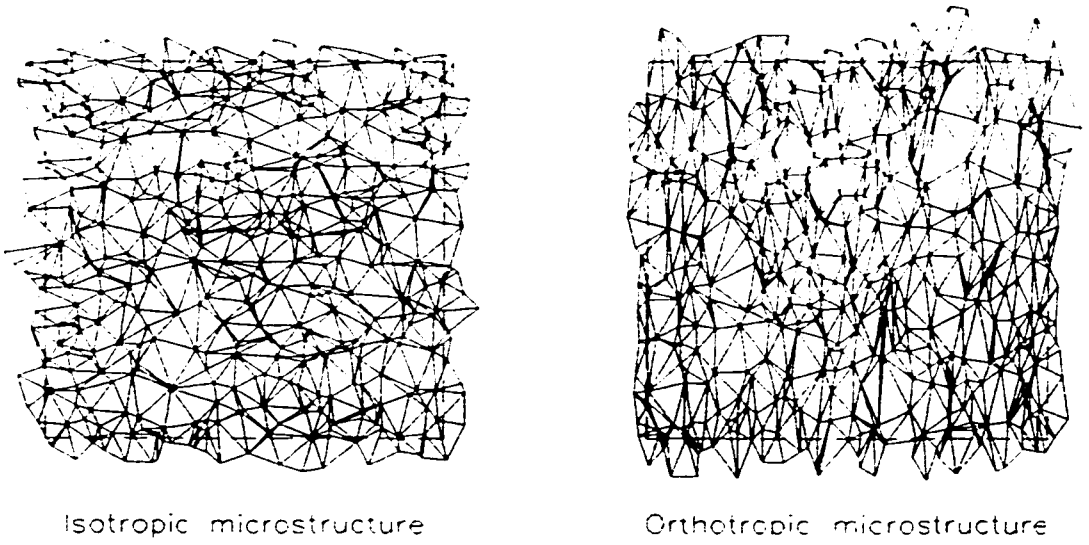

Figure 5.9: Comparison of isotropic and orthotropic microstructure (approximately 400 nodes in each network)

direction is higher than in x-direction. On average, the material is orthotropic: $\mathbf{E}(C_{12}) = \mathbf{E}(C_{13}) = 0$.

2. The results for the standard deviation in (5.6) indicate that the material is stochastically non-orthotropic: the standard deviation of C_{13} and C_{23} is of the same magnitude as for C_{11}, C_{12} and C_{33}.

3. Similar to the isotropic microstructure, the axial stiffnesses C_{11} and C_{22} are practically uncorrelated.

4. The microtexture affects the correlations as well. Because of the clear orientation of the network, the correlations between the shear and the axial stiffness, $\rho_{C_{11}C_{12}}$ and $\rho_{C_{12}C_{22}}$, are no longer identical. However, there are no drastic changes in correlation between (5.7) and (5.3).

5.3 Significance for Structural Analysis

5.3.1 Objective and Definitions

The goal of this section is to demonstrate the importance of an accurate estimation of the correlation between the individual elements of the elasticity matrix [C]. First, the impact of the correlations $\rho_{C_{ij}C_{kl}}$ on the structural response of continuum models is assessed. Two continuum models and one discrete model are defined:

- **Model 1: A micromechanically based continuum. The random field characteristics are obtained using stochastic homogenization of the microstructure. The second-moment information of C_{ij} is given in (5.1) and (5.2). The correlations between C_{ij} and C_{kl} are given in (5.3).**

- **Model 2:** A "classical" random continuum, as given by (4.5) where only E is modeled as a random field. Since all elastic moduli C_{ij} in Model 1 have the same COV, the random field characteristics of E can be chosen such that the marginal densities of the non-zero elements in (4.5) are identical in both models:

$$\mathrm{Var}(C_{11}) = \mathrm{Var}(C_{22}) = \mathrm{Var}\left(E/\left(1-\nu^2\right)\right) \tag{5.8}$$

$$\mathrm{Var}(C_{12}) = \mathrm{Var}\left(E\nu/\left(1-\nu^2\right)\right) \tag{5.9}$$

$$\mathrm{Var}(C_{33}) = \mathrm{Var}\left(E/2\left(1+\nu\right)\right) \tag{5.10}$$

- **Model 3:** A discrete micromechanical model. This is the basis for the homogenized continuum of Model 1. The model geometry is obtained as the Delaunay triangulation of a uniform Poisson point process with density $\lambda = 0.01$ and stiffness parameter $K = 10$.

In a second application, the structural response, obtained using the full discrete micromechanical Model 3 is compared with both continuum models.

5.3.2 Element Subject To Constant Strain

The differences between the stochastic properties of the elasticity matrix [C] in Model 1 and Model 2 have important consequences for structural analysis. Consider a rectangular element subject to a constant strain state $\boldsymbol{\epsilon} = \{0, \varepsilon_y, 0\}^{\mathbf{T}}$. The resulting stresses in the element are:

$$\begin{Bmatrix} \sigma_x \\ \sigma_y \\ \sigma_{xy} \end{Bmatrix} = \begin{Bmatrix} C_{12} \\ C_{22} \\ C_{23} \end{Bmatrix} \varepsilon_y \tag{5.11}$$

for Model 1, and

$$\begin{Bmatrix} \sigma_x \\ \sigma_y \\ \sigma_{xy} \end{Bmatrix} = \begin{Bmatrix} \nu \\ 1 \\ 0 \end{Bmatrix} \frac{E\varepsilon_y}{1-\nu^2} \tag{5.12}$$

for Model 2. Because the COV of the marginal densities is practically the same for all C_{ij}, both models will result in the same marginal densities for the stresses, except for the shear stress σ_{xy}, which is always zero in Model 2.

The impact of the correlation $\rho_{C_{ij}C_{kl}}$ between C_{ij} and C_{kl} is clear when the maximum shear stress $\sigma_{xy,max}$ is calculated:

$$\sigma_{xy,max} = \sqrt{\left(\frac{\sigma_x - \sigma_y}{2}\right)^2 + \sigma_{xy}^2} \tag{5.13}$$

A SFE analysis indicates that the contribution of the shear stresses σ_{xy} in the horizontal and vertical direction to the maximum shear stress $\sigma_{xy,max,1}$ is minimal in this application. If their contribution is ignored, an analytic expression for the variance for the maximum shear stress $\sigma_{xy,max,1}$ can be obtained by FOSM analysis:

$$\begin{aligned} \mathrm{Var}\left(\sigma_{xy,max,1}\right) &= \frac{\varepsilon_y^2}{4}\left[\mathrm{Var}\left(C_{12}\right) + \mathrm{Var}\left(C_{22}\right) - 2\mathrm{Covar}\left(C_{12}, C_{22}\right)\right] \\ &= \frac{\varepsilon_y^2}{4}\left[\mathrm{Var}\left(C_{12}\right) + \mathrm{Var}\left(C_{22}\right) - 2\rho_{C_{12},C_{22}}\sqrt{\mathrm{Var}\left(C_{12}\right)\mathrm{Var}\left(C_{22}\right)}\right] \end{aligned} \tag{5.14}$$

for Model 1, and equal to

$$\mathrm{Var}\left(\sigma_{xy,max,2}\right) = \frac{\varepsilon_y^2}{4}\left(1-\nu\right)^2 \mathrm{Var}\left(C_{22}\right) \tag{5.15}$$

for Model 2.

For the microstructure, based on a uniform Poisson point process, the ratio of the variances of $\sigma_{xy,max}$ predicted by Model 1 and 2 is equal to 3.82. When only E

is modeled as a random field, which implies a perfect correlation between all C_{ij}, the uncertainty of the structural response of the material is underestimated. This finding is also confirmed by the following example.

5.3.3 SFEM Analysis of Square Disk With Hole

In this application, a square disk (1000×1000) with a hole in the center ($\emptyset = 600$) is subject to a uniform horizontal displacement at the right edge (Figure 5.10). Even though the model is, strictly speaking, not symmetric, identical statistics will be obtained for all four quarters and thus only the upper-right quarter is modeled. A three-way comparison is made for the horizontal reaction force F_x and the vertical displacement u_y at the inside top of the plate.

The discrete micro-mechanical model, which consists of approximately 2000 nodes, is compared with the continuum Models 1 and 2. To ensure maximum consistency with the assumptions used for homogenization, only constant strain triangular elements are used in the Monte Carlo-based SFEM. The random fields for C_{ij} or E are discretized through local averaging over the finite elements [Vanmarcke and Grigoriu, 1983]. A covariance decomposition method, which ensures that the second-moment information of the random fields and the correlations between the elements is represented exactly in each sample field, is used to generate sample fields for C_{ij} or E [Yamazaki and Shinozuka, 1990].

The variances and covariances of the random fields, locally averaged over the triangular elements, are evaluated through approximation of the triangular area as a sum of smaller rectangles (see Figure 5.11). The variance over each rectangle is readily obtained from the VRF (5.4). The cross-covariance of the locally averaged

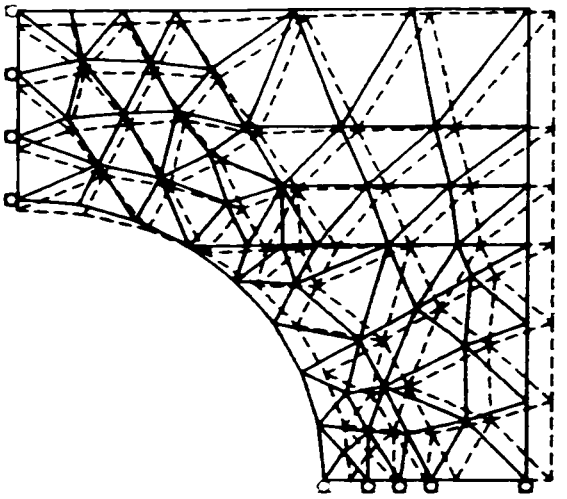

Figure 5.10: FE mesh and deformed state of square disk with hole, subject to uniform displacement at right edge

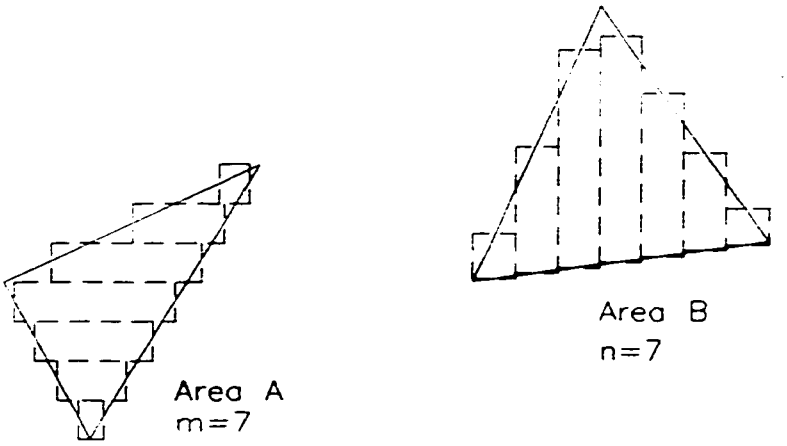

Figure 5.11: Evaluation of the covariance of a locally averaged random field over triangular finite elements

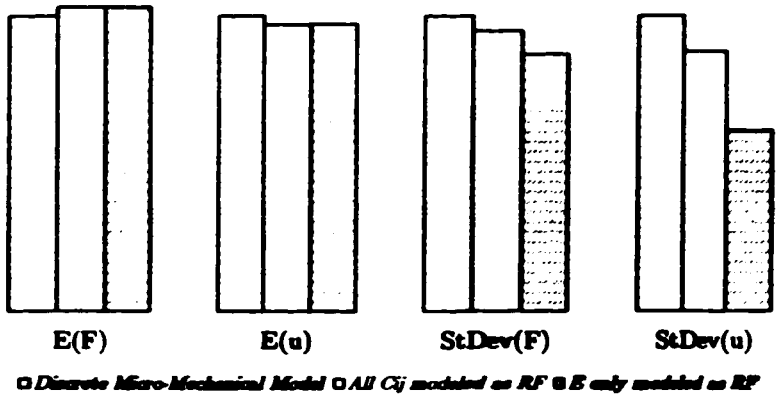

Figure 5.12: Three-way comparison of response statistics of square disk

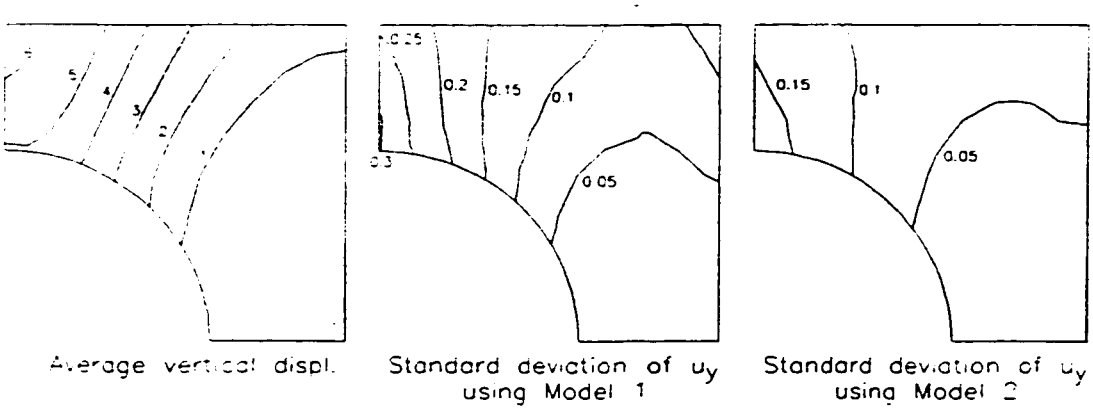

Figure 5.13: Contour plots for the average vertical displacement u_y and the standard deviation of u_y, obtained using Model 1 and 2.

random fields X_A and Y_B is then:

$$\text{Covar}(X_A, Y_B) = \frac{\text{Covar}(X,Y)}{4A_A A_B} \sum_{i=1}^{m}\sum_{j=1}^{n}\sum_{k=0}^{3}\sum_{l=0}^{3}(-1)^{k+l}\Gamma(\ell_{1k}, \ell_{2l}) \qquad (5.16)$$

where A_A and A_B denote the area of each element, $\Gamma(\ell_{1k}, \ell_{2l}) = (\ell_{1k}\ell_{2l})^2\gamma(\ell_{1k}, \ell_{2l})$, and the lengths $\ell_{\alpha\beta}$ are defined in Figure 4.9a. The number of rectangles m and n required for each element is determined such that the use of either horizontal or vertical rectangular strips (see Figure 5.11) results in the same variance or covariance.

Figure 5.12 shows that the expected values of both the horizontal reaction force F_x and the vertical displacement u_y at the inside top of the plate are practically identical in all three models. A contour plot of the expected value of the vertical displacement u_y is given in Figure 5.13. The standard deviation of u_y, obtained using Models 1 and 2 is also shown in Figure 5.13. It can be seen that Model 2 grossly underestimates the variance. The standard deviation of u_y, obtained from Model 2, is only 48% of the standard deviation, found with Model 1.

The variance obtained by Model 1 is still somewhat smaller than for the micro-mechanical model. This must be attributed to the use of a locally averaged discretization technique in the Monte Carlo SFEM, as explained by Der Kiureghian and Ke (1988). Other discretization techniques are discussed in Li and Der Kiureghian (1993), Fenton (1994), and Zhang and Ellingwood (1994).

5.4 Selection of Micro-Mechanical Model Parameters

5.4.1 Introduction

In trying to develop a continuum model that is stochastically consistent with an assumed micromechanical model and assessing the sensitivity of macro-random field

to the micromodel assumptions, it is necessary to examine the effects of some basic choices, such as:

1. The type and degree of uncertainty associated with the elastic micro-mechanical model links, see equation (4.8)

2. The characteristics of the discrete spatial random field which generates the micro-geometry

5.4.2 Micro-Link Stiffness

All evidence [Zubelewicz and Bažant, 1987; Ostoja-Starzewski, 1994b] indicates that the first choice mentioned in Section 5.4.1. is not as critical as the second one since any randomness associated with the link stiffness K tends to average out over the random lattice of links. This is confirmed by our simulations where the stiffness parameter K in (4.8) is modeled as a random variable.

In these simulations, a uniform, lognormal and Weibull distribution are assumed for the stiffness parameter K. All these distributions have the same mean value K, and simulations are repeated for COVs of 30% and 60%. Figure 5.14 compares the mean value of C_{11} and C_{12} obtained for the lognormal assumption for K with the result obtained for deterministic K. For a COV of 30%, a drop of the macroscopic stiffness C_{ij} of less than 5% is observed. When the COV is increased to 60%, the stiffness drops about 15%. Similar results are obtained when a Weibull or a uniform distribution is used for K.

The variance of C_{ij} remains virtually unaffected by the uncertainty associated with the microstiffness K. For a lognormally distributed K with COV of 60%,

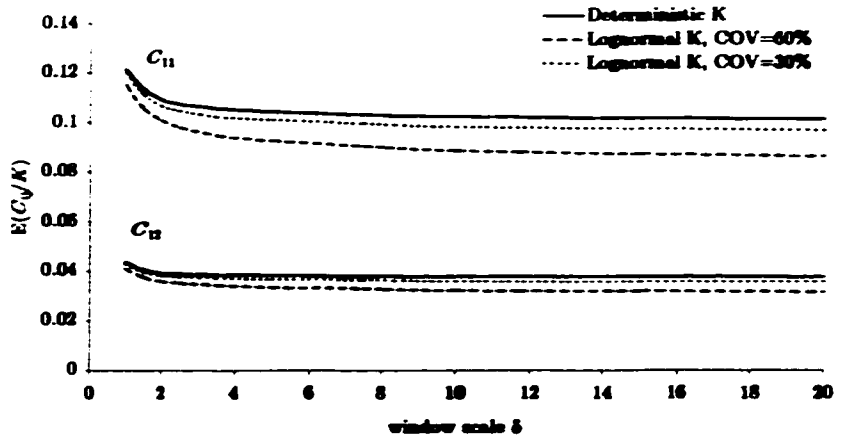

Figure 5.14: **Effect of uncertainty associated with K on the average elastic modulus C_{11}**

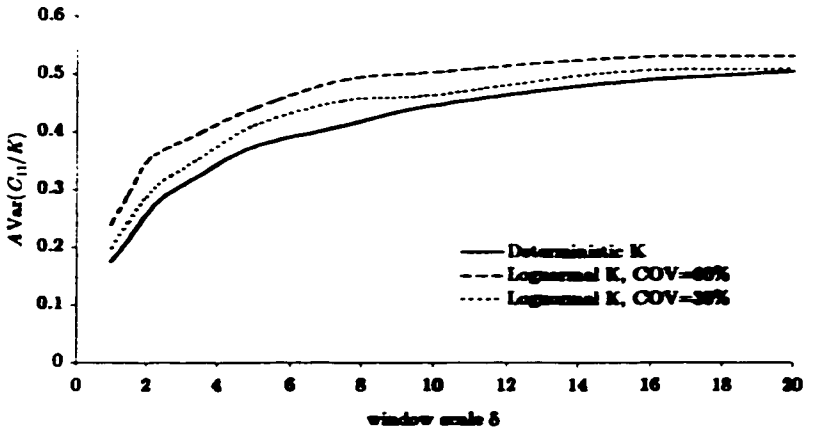

Figure 5.15: **Effect of uncertainty associated with K on $A\mathrm{Var}(C_{11})$ of the elastic modulus C_{11}**

$\mathrm{Var}(C_{11})$ increases by just 5%, compared with $\mathrm{Var}(C_{11})$, obtained on the basis of a deterministic stiffness parameter K. It can be concluded that the uncertainty associated with the microlevel stiffness parameter K has only a negligible effect on the variability of the elasticity matrix [C]. Because the variances are virtually unchanged for all window sizes, it follows from (4.41) that the correlation functions $R_{C_{ij}C_{kl}}(x, y)$ also remain unaffected by the type and degree of micro-link uncertainty.

5.4.3 Microgeometry

In all but one of the above models, the Delaunay lattice is based on a set of nodes which is generated from a Poisson point process with a uniform density λ per unit area. Only the orthotropic micromodel in Section 5.2.2 is based on a non-uniform Poisson point process. Loosely speaking, the nodes in the triangulation represent the centers of the discrete constituents on the microscale. When a uniform Poisson process is used to generate these nodes, it is possible for nodes to be extremely close to each other, which is not a realistic modeling of the physical microstructure. The impact of two alternatives to the uniform Poisson point process, which are suggested in Chapter 2, on the random field characteristics of the elastic properties will be assessed. The node-generating processes considered are:

1. randomly disturbed lattice process

2. censored Poisson process

Sample realizations of these geometries are contrasted with a uniform Poisson process-based lattice in Figure 5.16. The disturbed lattice is based on a regular grid of evenly spaced points, which is altered by moving each node randomly over a

certain distance or within a certain area (see Figure 2.18). In this dissertation, the discussion is restricted to disturbed lattices based on a regular square grid pattern, where each vertex is moved randomly as explained in Schlangen and Van Mier (1992): the rectangular homogenization window A is divided into n equal squares each of size a^2, which each contain exactly one vertex. The randomness is controlled by a single parameter $0 \leq \alpha \leq 1$, where α is the ratio of the length of the square in which the vertex must lay to the length a of one grid square.

The link lengths resulting from the three different spatial random processes have distinct density functions (Figure 5.17), which indicates that the micro-geometric model must be selected carefully, typically based on image analysis. It should be noted that when a square grid is used as the basis for a disturbed lattice model, the link length distribution becomes bimodal as the variability parameter α decreases. A discrete distribution is obtained when $\alpha = 0$: $\text{Prob}(\ell = a) = \frac{2}{3}$, $\text{Prob}(\ell = a\sqrt{2}) = \frac{1}{3}$.

For $\alpha = 1$, each node is located randomly within its grid square of size a^2. The variance of the link length is less than half of the variance of the link length in the lattice, based on a uniform Poisson point process. This reduced link length variance results in a considerable reduction of the variance of the elasticity matrix [C] of the equivalent continuum as indicated in Table 5.1, obtained using the displacement-based homogenization (4.20).

The disturbed lattice model is less random than the lattice based on a uniform Poisson point process. As a result the expected value of [C] is increased for the disturbed lattice model. For $\alpha = 0$, no randomness is associated with the disturbed lattice model and the deterministic result for [C] is obtained from equation (4.4): $C_{11} = C_{22} = 1.3536$, $C_{12} = C_{33} = 0.3536$, and $C_{13} = C_{23} = 0$.

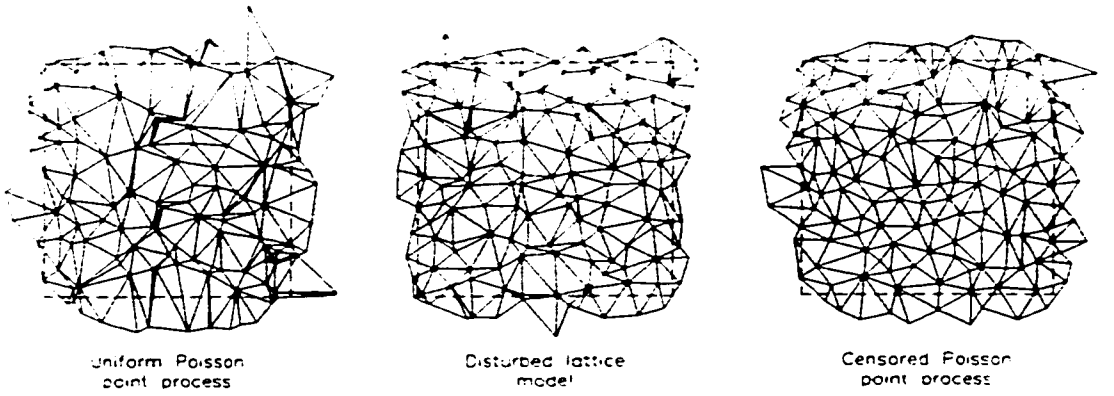

Figure 5.16: **Sample microstructures obtained as Delaunay triangulations of three different node-generating point processes**

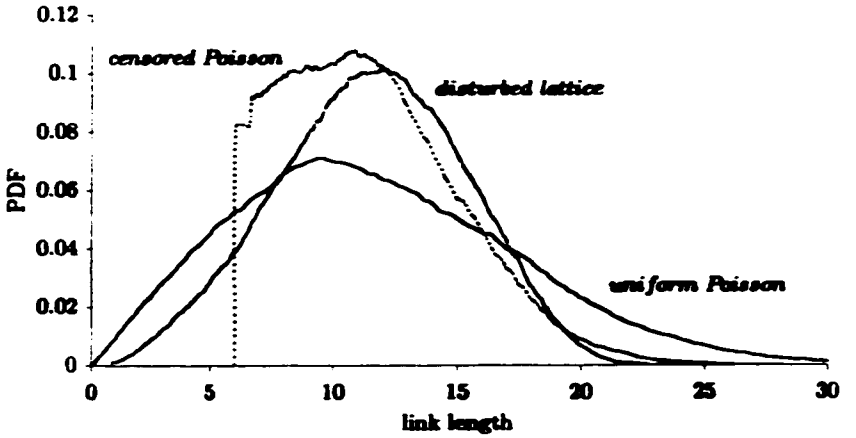

Figure 5.17: **Comparison of the PDF of the link lengths resulting from the use of three different spatial random processes (density $\lambda = 0.01$)**

The correlations $\rho_{C_{ij}C_{kl}}$ between C_{ij} and C_{kl} obtained with the disturbed lattice model are given below and can be compared with the ones for a uniform Poisson process model, given in equation (5.3). The standard error for these estimated correlations is less than 0.025.

$\rho_{C_{ij}C_{kl}}$	C_{11}	C_{12}	C_{13}	C_{22}	C_{23}	C_{33}
C_{11}	1	-0.020	0.003	-.683	-.033	-.090
C_{12}		1	-.013	0.042	-.041	0.616
C_{13}			1	0.006	0.705	0.021
C_{22}				1	0.028	0.001
C_{23}			*sym*		1	0.001
C_{33}						1

(5.17)

It can be seen that, unlike the correlations resulting from a homogenized uniform Poisson lattice, there is:

- A strong negative correlation between the axial moduli C_{11} and C_{22}
- An absence of correlation between the axial (C_{11} or C_{22}) and the shear moduli (C_{12} or C_{33})

The strong negative correlation between C_{11} and C_{22} can be explained as follows. Since the total number of nodes in the disturbed lattice model is fixed, a higher than average C_{11} value can only be obtained if the spatial distribution of the nodes is such that the links which connect the nodes are more aligned in x-direction. Since each grid cell of size a^2 contains exactly one node, it automatically follows that the

links must be less aligned along the y-axis, which results in a lower than average C_{22}-value.

The results of using a disturbed lattice process are also compared with those from a censored Poisson process. Censoring is achieved by imposing a minimum distance between nodes, which can be interpreted as the minimum physical size of the constituents in the micro-mechanical model. The censoring is chosen such that the variance for the link length in the lattice is equal to the variance of the disturbed lattice model with $\alpha = 1$. The resulting link distributions are shown in Figure 5.17. For some C_{ij}, the variance is quite sensitive to the choice of the point process (Table 5.1). The correlations $\rho_{C_{ij}C_{kl}}$, obtained using the censored Poisson process (5.18), are very similar to the ones for the lattices based on a uniform Poisson point process, given in (5.3). Because of the increased order in the microstructure (see Figure 5.16), those correlations which are already significantly different from zero in (5.3) are now even more pronounced: particularly $\rho_{C_{12}C_{33}}$ has increased.

$\rho_{C_{ij}C_{kl}}$	C_{11}	C_{12}	C_{13}	C_{22}	C_{23}	C_{33}
C_{11}	1	0.462	-.080	0.059	-.069	0.548
C_{12}		1	-.023	0.504	0.006	0.819
C_{13}			1	0.020	0.754	-.013
C_{22}				1	0.057	0.557
C_{23}			*sym*		1	0.012
C_{33}						1

(5.18)

It is also interesting to assess the impact on the autocorrelation of the random fields. Figure 5.18 shows how fast the product $A\text{Var}(C_{11})$ approaches its asymptotic

Elastic Moduli	Uniform Poisson		Disturbed Lattice		Censored Poisson	
	Mean	St. Dev.	Mean	St. Dev.	Mean	St. Dev.
C_{11}	1.033	0.075	1.116	0.043	1.088	0.057
C_{12}	0.385	0.025	0.386	0.014	0.374	0.017
C_{13}	0.000	0.028	-.001	0.024	0.001	0.024
C_{22}	1.035	0.075	1.112	0.042	1.088	0.059
C_{23}	0.000	0.028	-.001	0.023	0.000	0.024
C_{33}	0.324	0.020	0.356	0.011	0.358	0.016

Table 5.1: Comparison of summary statistics of elastic moduli ($\lambda = 0.01, K = 10, A = 100 \times 100$)

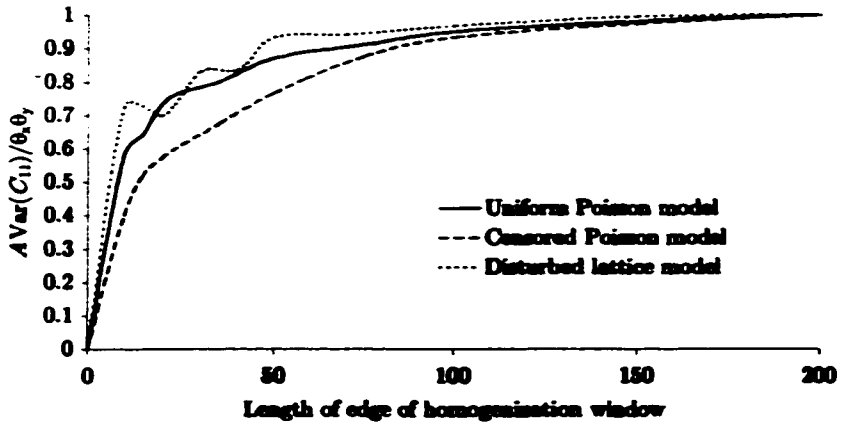

Figure 5.18: Comparison of the correlation length of C_{11} resulting from the use of three different spatial random processes (nodal density $\lambda = 0.01$)

value $\theta_x\theta_y$. The faster the characteristic area $\theta_x\theta_y$ is approached, the shorter the correlation length is. When a censored Poisson process is used, the location of a node is dependent on the location of the neighboring nodes in the network. Consequently, correlations must exist in the random field of the homogeneous continuum over longer distances than when the network is based on a uniform Poisson process. This is confirmed in Figure 5.18.

5.5 Comparison of Homogenization Techniques

It is also useful to examine the effect of selecting any of the different homogenization techniques: (4.20), (4.23) and (4.34). All results are obtained for lattice geometries, based on a uniform Poisson point process with nodal density $\lambda = 0.01$. Figure 5.19 shows that the uniform strain approximation in (4.23) leads to an overestimation of the expected values of C_{ij}, as was previously reported by Ostoja-Starzewski and Wang (1990). This is not surprising since prescribing a displacement at every node of the lattice model overestimates the total stiffness. This overestimation depends on the size of the lattice but it levels off for large window sizes: in this case the overestimation stabilizes around 25% for C_{11} and 12% for C_{12}. It is also interesting to note that when homogenization is performed based on (4.23) the elastic shear moduli C_{12} and C_{33} are identical.

The force-based homogenization technique (4.34) results in an expected value of [C] very close to the one obtained using (4.20). The estimated correlations $\rho_{C_{ij}C_{kl}}$ obtained using both homogenization techniques are also very similar.

However, the force-based method should not be used for small averaging windows

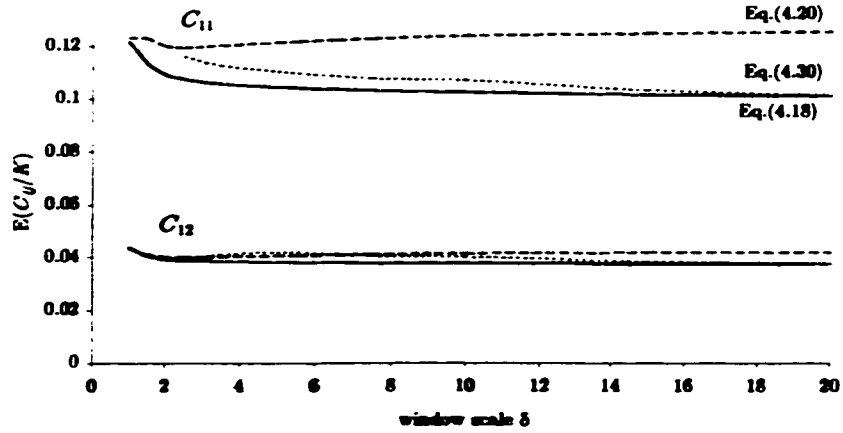

Figure 5.19: Comparison of mean value of C_{11}, obtained using different homogenization techniques

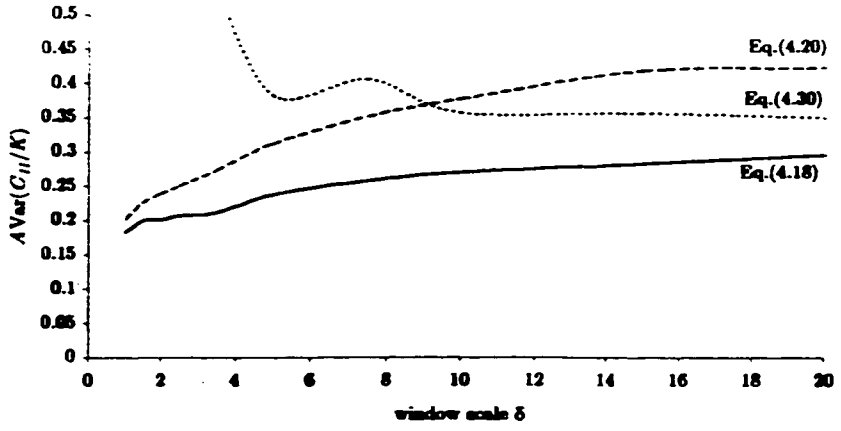

Figure 5.20: Comparison of $AVar(C_{11}/K)$, obtained using different homogenization techniques

(say $\delta \leq 5$) because the application of boundary forces at just a few nodes, randomly located along this boundary, is a poor approximation of a uniform boundary stress. As the averaging window size decreases, the number of boundary nodes goes down as well and the corrector forces F'' become relatively more important. The corrector forces F'' in (4.29), required in the force-based homogenization, introduce spurious variance, which distort the VRF. By virtue of (4.41), this, in turn, leads to incorrect estimates of the auto-correlation functions. For illustration purposes, the product $A\text{Var}(C_{11}/K)$ is plotted in Figure 5.20. It is clear that the variance becomes unstable for small averaging areas A.

It can be concluded that the newly developed force-based technique (4.34) provides an efficient and accurate alternative to (4.20) for the estimation of the average stiffness, particularly for large averaging window sizes. The simulations show that its use results in the same VRF as obtained using the displacement-based homogenization (4.20). Because of the previously mentioned computational savings - see Chapter 4 - associated with (4.23) and (4.34), the combined use of (4.34) and (4.23) provides a computationally efficient alternative to (4.20).

5.6 Summary

In this chapter, the random field characteristics of the elastic properties, which are consistent with the microstructure, are determined using the framework developed in Chapter 4. The technique is applied to a variety of microstructures: both isotropic and orthotropic microstructures are homogenized.

The stochastic characteristics of the resulting consistent random fields are quite

different from the characteristics of a random field which is based on a straightforward randomization of the deterministic elastic constitutive equations. It is shown how a model where only E or where both E and ν are considered random fields cannot be consistent with the assumed micromechanical model. The micromechanically based homogenization technique is able to model how isotropy is achieved in the mean only and all materials are stochastically anisotropic.

It is shown that when only Young's modulus E is modeled as a random field the variability of the macroscopic behavior is underestimated because in that case a perfect correlation is assumed between all elastic moduli C_{ij}. This is illustrated by means of examples, which indicate the importance of a correct estimation of the correlations between the material properties. When the suggested stochastic homogenization procedure is followed, the correlations automatically follow from the homogenization of the microstructure.

The effects of uncertainties associated with the micromechanical model are assessed. Based on simulations for various micromechanical models, it can be concluded that uncertainty associated with the microlevel stiffness is of relatively minor importance for COV-levels up to 60%. The microgeometry needs to be modeled carefully. This can be achieved through comparison of the statistics of a mathematical microgeometric model with the results of an image analysis of the actual microstructure of the material. The simulations show that the estimation of the correlations between the elastic properties is fairly robust as long as the overall variability in the microgeometry is modeled correctly.

Chapter 6

Conclusions and Recommendations

6.1 Summary

In this dissertation the random field modeling of elastic material properties is addressed. The main conjecture of this research is that the variability of the structural behavior of materials on the macroscale is chiefly caused by randomness in their microstructure. Using micromechanical models, the macroscopic structural behavior automatically follows from the interaction between, and the deformation of, the discrete constituents at the microscale, subject to a given loading. A homogenization of the micro-structure provides a theoretical basis for a continuum model. By including the microlevel variabilities in the homogenization procedure, the uncertainties associated with the macroscopic material parameters can be estimated directly from the micromechanical model.

An overview of existing micro-mechanical models is given in Chapter 2. Both systems with regular and random geometry are discussed. The microscale should be selected carefully and depends on the application. The level of detail required for the micro-mechanical model is given by the minimum scale below which the behavior of the material holds no practical interest. Guidelines for the selection of a discrete model are given. The identification of the appropriate microgeometric model is usually performed on the basis of image analysis and is beyond the scope of this research. The characteristics of simulated microstructures are compared with

the statistics of actual microstructures, which allows us to estimate the parameters of the discrete random spatial process.

The exploratory analysis in Chapter 3, based on a one-dimensional parallel bar model, indicates the importance of incorporating the physical microstructure of a material in a probabilistic model of structural material behavior. The bending example demonstrates that, depending on the correlation structure of the random field of the material properties, the variability of the macroscopic behavior, which is predicted by a straightforward randomization of a continuum model, can be very different from the variability predicted by a micro-mechanical model.

Two approaches can be followed to estimate the correlation structure. In the first one, a correlation model is assumed and the parameters of the auto- and cross-correlation functions are estimated from experimental data. This option does require a relatively large amount of test data in order to be accurate. The second approach, which is taken in this dissertation, is to estimate the auto- and cross-correlations directly from the microstructure. This approach can only be used if the selected micromechanical model accurately reflects the microstructure.

In this case, the random field model of the material properties is obtained on the basis of a stochastic homogenization of the microstructure. To this extent, a general-purpose stochastic homogenization theory is presented in Chapter 4. The theory can, in principle, be applied to both lattice and discrete particle micromechanical models. A continuum is said to be equivalent with the discrete micromodel if its strain energy is identical to that of the microstructure when they are both subject to the same boundary conditions.

Existing homogenization techniques, which are based on essential boundary con-

ditions, are complemented with a new, computationally more efficient, though approximate, force-based homogenization technique. The material properties, obtained after homogenization of the microstructure over an area, are considered sample realizations of the local averages of the random material properties of the material. The random field description of the material properties has a theoretical foundation in local average random field theory. Monte Carlo simulation of sample microstructures, followed by homogenization and subsequent estimation of the variance reduction function, allows one to estimate the auto- and cross-correlations of the random fields of the material properties directly from the microstructure.

The selection of boundary conditions for homogenization requires careful analysis. Different boundary modeling techniques are discussed and their impact on the estimation of the auto-correlation of the material properties is assessed. The shortcomings, associated with existing boundary modeling techniques of discrete microstructures are identified and an improved modeling is introduced. The superiority of the new boundary modeling is demonstrated.

The main advantage of determining the material parameter random fields through homogenization is that a more consistent random field modeling is obtained. There is no longer a need to make assumptions regarding the auto-correlation function of the material parameters. The possible correlations between different material parameters automatically follow from the procedure as well.

The significance of the new random field modeling for structural analysis is demonstrated in Chapter 5. The method is applied to both isotropic and anisotropic materials. Stochastic homogenization of a lattice-type microgeometry, based on a uniform Poisson point process, shows that isotropy of materials is achieved in a

mean sense only. The assumption of a perfect correlation between C_{11} and C_{22} in traditional continuum models seems unjustified. Practical applications illustrate the significance of a correct estimation of the correlations between the material properties.

The superior performance of the homogenization-based random field modeling technique is demonstrated in a structural application. The micro-mechanical analysis is compared with two Monte Carlo SFEM, using two different random field models of the material parameters. One random field model is based on a straightforward randomization of deterministic constitutive models and treats only Young's modulus E as a random field. The other random field model is obtained through micromechanically-based stochastic homogenization. A direct three-way comparison of the statistics of structural responses obtained from all three models, demonstrates the superior performance of the new random field modeling technique. A structural analysis where only E is considered a random field will underestimate the variability of the response.

The sensitivity of the random field properties to uncertainties associated with the micro-structure is assessed as well. The analysis indicates that the characteristics of the microgeometric model dictate the stochastic characteristics of the material properties. Randomness associated with the micro-level stiffness has only minor impact on the variability of the macroscopic behavior. This means that a limited number of macroscopic tests suffices to estimate the microlevel stiffness.

The main accomplishments of this research are:

1. A new homogenization procedure, which is based on equivalence of strain en-

ergy under an assumed stress distribution along the boundary of homogenization window in the continuum and the discrete micro-mechanical model, is formulated. The method complements existing techniques for homogenization, which are based on assumed strain states in the material.

2. Shortcomings of existing boundary condition models currently used in the analysis of discrete micro-mechanical systems are identified and an improved boundary modeling technique is introduced. Theoretical considerations, as well as numerical examples, illustrate the superior performance of this modeling.

3. A new random field modeling of linear elastic materials is proposed. The model is consistent with the microstructure in the material and allows to estimate the auto- and cross-correlations of the elastic properties, directly from the microstructure.

4. The relevance of this improved random field model for reliability-based design is clearly demonstrated. It is shown how a straightforward randomization of deterministic material models underestimates the variability of the structural responses.

6.2 Recommendations for Future Research

The applications presented in this dissertation clearly show the superiority of determining the random field characteristics of material properties on the basis of a stochastic homogenization of the discrete microstructure. Since the usefulness of the technique is now established, extensions of this technique to different fields of

application are desirable. Also, more robust and efficient algorithms need to be developed.

Extension to other stress and strain states

Even though the homogenization theory is applicable to all types of stress or strain states, all applications are developed for plane stress situations only. Especially for FE applications, an extension to out-of-plane behavior, such as plate bending elements, would be useful. Particularly an extension to 3D stress and strain states is desirable as it is anticipated that the variability resulting from a 3D model will be larger than for a 2D model.

Extension to discrete particle models

As outlined in Chapter 2, lattice models are very attractive from a computational point of view, but they have some limitations. In a spring model, the microlevel constitutive law can only account for axial interaction, which results in a fixed Poisson's ratio. This limitation is overcome when a discrete particle model is used and the friction between the microlevel constituents can be taken into account. This leads to a much more accurate model description. These applications are now within reach because of the increased computer power. Randomly distributed defects or inclusions of other phases, such as in composite materials, could be added to the micromodel as well.

Extension to "non-uniform" micromechanical models

In all applications considered, the discrete spatial process which defines the microgeometry is homogeneous and almost uniform over every domain larger than the RVE.

As a result no long-range correlations exist in the random fields of the elastic properties and a finite-scale model is appropriate to estimate the characteristics of the RF. Depending on the characteristics of the manufacturing or the natural formation process of the material considered, the statistics of the spatial process may no longer be independent of the location. The stochastic homogenization approach should be extended to include these effects.

Extension to non-Gaussian random field modeling

Gaussian random fields need to be truncated if only non-negative values are possible. This problem becomes increasingly important when large COV is associated with the random fields. In our simulations it was observed that the elements of the compliance matrix $[C]^{-1}$ are very accurately modeled by the non-negative Gamma-distribution, even for small averaging windows. Unfortunately, local averaging techniques are not directly applicable to Gamma fields since the Gamma distribution is not closed under averaging. A Nataf-type transformation, which preserves the correlation, to Gaussian random fields might allow the use of local averages. The physical meaning of the transformed compliances would be lost though. Further research is required in this field.

Robust modeling techniques

The covariance-decomposition method used in the Monte Carlo SFEM application leads to numerical difficulties for large meshes. Estimation errors are associated with the covariances of the elements and propagate into the eigenvalues of the covariance matrix. As the number of elements increases, the covariance matrix becomes nearly singular. It is observed that the correlations between C_{ij} and C_{kl} are almost constant

as long as the averaging area A is not too small and the aspect ratio of A not too much different from 1. In this case, it might be possible to transform the correlated C_{ij}-fields into six independent random fields. This would substantially reduce the size of the covariance matrix, but the physical meaning of the correlation length in the new random fields would be lost. This warrants further research.

Extension to non-linear behavior

The examples in Chapter 3 illustrate how complex macroscopically non-linear material behavior can realistically be modeled using micromechanics. Non-linearities, such as failure or yielding of the links in a lattice model, are introduced at the microlevel and the macroscopic structural behavior is obtained from the interaction between the microconstituents. The homogenization procedure can be extended to include non-linear behavior. Since, at least for lattice-type microstructures, materials are stochastically anisotropic, this may lead to interesting developments in stochastic crack growth models. As the computer power keeps increasing, this application will become computationally feasible in the future.

Bibliography

Adler, R. J. (1981). *The Geometry of Random Fields*, John Wiley & Sons, New York, NY.

Anandarajah, A. (1995). Discrete-Element Method for Simulating Behavior of Cohesive Soil, *ASCE Journal of Geotechnical Engineering* **120**: 1593–1613.

Anandarajah, A. and Lu, N. (1991). Structural Analysis by Distinct Element Method, *ASCE Journal of the Engineering Mechanics Division* **117**: 2156–2165.

Bascoul, A. (1996). State of the Art Report - Part 2: Mechanical Micro-Cracking of Concrete, *Matériaux et Constructions/Materials and Structures* **29**: 67–78.

Bathurst, R. J. and Rothenburg, L. (1988). Micromechanical Aspects of Isotropic Granular Assemblies With Linear Contact Interactions, *ASNE Journal of Applied Mechanics* **55**: 17–23.

Bažant, Z. and Cedolin, L. (1991). *Stability of Structures. Elastic, Inelastic, Fracture, and Damage Theories*, Oxford University Press.

Bažant, Z. P., Tabbara, M. R., Kazemi, M. T. and Pijaudier-Cabot, G. (1990). Random Particle Model for Fracture of Aggregate or Fiber Composites, *ASCE Journal of Engineering Mechanics* **116**: 1686–1705.

Beran, M. J. (1968). *Statistical Continuum Theories*, Interscience Publishers, New York, NY.

Beran, M. J. and McCoy, J. J. (1970). Mean Field Variations in a Statistical Sample of Heterogeneous Linearly Elastic Solids, *International Journal of Structures and Solids* **6**: 1035–1054.

Bizup, D. F. and Singpurwalla, N. D. (1996). Probabilistic Aspects of Material Failure, *in* D. M. Frangopol and M. D. Grigoriu (eds), *Probabilistic Mechanics & Structural Reliability. Proceedings of the Seventh Specialty Conference, ASCE*, pp. 474–477.

Bogdanoff, J. and Kozin, F. (1985). *Probabilistic Models of Cumulative Damage*, John Wiley & Sons.

Breysse, D. (1990). Un Modèle Probabiliste d'Endommagement Résultant d'une Approche Micro-Macro, *Matériaux et Constructions/Materials and Structures* **23**: 161–171.

Breysse, D., Fokwa, D. and Drahly, F. (1994). Spatial Variability in Concrete: Nature, Structure, and Consequences, *Applied Mechanics Reviews* **47**: S184–S196.

Burt, N. and Dougill, J. (1977). Progressive Failure in a Model Heterogeneous Medium, *ASCE Journal of the Engineering Mechanics Division* **103**: 365–376.

Chakraborty, S. and Dey, S. S. (1996). Stochastic Finite Element Simulation of Random Structure on Uncertain Foundation Under Random Loading, *International Journal of Mechanical Sciences* **38**: 1209–1218.

Christensen, R. M. (1994). Heterogeneous Material Mechanics at Various Scales, *Applied Mechanics Reviews* **47**: S20–S33.

Cundall, P. A. and Hart, R. G. (1992). Numerical Modelling of Discontinua, *Engineering Computations* **9**: 101–113.

Cundall, P. A. and Strack, O. D. L. (1979). A Discrete Numerical Model for Granular Assemblies, *Géotechnique* **29**: 47–65.

Daniels, H. E. (1945). The Statistical Theory of the Strength of Bundles of Threads. I., *Proceedings of the Royal Society of London. Series A* **183**: 405–435.

De Schutter, G. and Taerwe, L. (1993). Random Particle Model for Concrete Based on Delaunay Triangulation, *Matériaux et Constructions/Materials and Structures* **26**: 67–73.

Deodatis, G. (1990). Bounds on Response Variability of Stochastic Finite Element Systems: Effect of Statistical Dependence, *Probabilistic Engineering Mechanics* **5**(2): 88–98.

Deodatis, G. and Graham, L. L. (1998). Variability Response Functions for Structures with Multiple Uncertain Material and/or Geometric Properties, *in* N. Shiraishi, M. Shinozuka and Y. K. Wen (eds), *Structural Safety and Reliability*, ICOSSAR '97, Balkema, Rotterdam, pp. 883–890.

Deodatis, G. and Shinozuka, M. (1989). Bounds on response variability of stochastic systems, *ASCE Journal of Engineering Mechanics* **115**: 2543–2563.

Der Kiureghian, A. and Ke, J.-B. (1988). The Stochastic Finite Element Method in Structural Reliability, *Probabilistic Engineering Mechanics* **3**(2): 83–91.

Ditlevsen, O. and Tarp-Johansen, N. J. (1996). Choice of Input Fields in Stochastic Finite Elements, *in* D. M. Frangopol and M. D. Grigoriu (eds), *Probabilistic Mechanics & Structural Reliability. Proceedings of the Seventh Specialty Conference, ASCE*, pp. 820–837.

Dobry, R. and Ng, T.-T. (1992). Discrete Modelling of Stress-Strain Behaviour of Granular Media at Small and Large Strains, *Engineering Computations* **9**: 129–143.

Efron, B. and Tibshirani, R. J. (1993). *An Introduction to the Bootstrap*, Chapman and Hall, New York, NY, USA.

Elishakoff, I., Ren, Y. J. and Shinozuka, M. (1994). Conditional Simulation of Non-Gaussian Random Fields, *Engineering Structures* **16**: 558–563.

Eranti, E. and Lee, G. C. (1986). *Cold Region Structural Engineering*, McGraw-Hill, New York, NY.

Fanella, D. and Krajcinovic, D. (1985). Continuum Damage Mechanics of Fiber Reinforced Concrete, *ASCE Journal of Engineering Mechanics* **111**: 995–1009.

Fenton, G. A. (1994). Error Evaluation of Three Random-Field Generators, *ASCE Journal of Engineering Mechanics* **120**: 2478–2497.

Fenton, G. A. (1999a). Estimation of Stochastic Soil Models, *ASCE Journal of Geotechnical and Geoenvironmental Engineering* **125**: 470–485.

Fenton, G. A. (1999b). Random Field Modeling of CPT Data, *ASCE Journal of Geotechnical and Geoenvironmental Engineering* **125**: 486–498.

Fenton, G. A. and Vanmarcke, E. H. (1990). Simulation of random fields via local average subdivision, *ASCE Journal of Engineering Mechanics* **116**: 1733–1749.

Field, D. A. (1991). A Generalic Delaunay Triangulation Algorithm for Finite Element Meshes, *Advances in Engineering Software and Workstations* **13**: 263–272.

Frost, H. J. and Thompson, C. V. (1987). The Effect of Nucleation Conditions on the Topology and Geometry of Two-Dimensional Grain Structures, *Acta Metallurgica* **35**: 529–540.

Gasparini, D. A., Bonacuse, P., Powers, L. and Romeo, A. (1996). Stochastic Parallel-Brittle Networks for Modeling Materials, *ASCE Journal of Engineering Mechanics* **122**: 130–137.

Gasparini, D. A., Romeo, A., Powers, L. and Bonacuse, P. (1995). On Stochastic Parallel-Brittle Networks for Modeling Materials, *in* M. Lemaire, J.-L. Favre and A. Mébarki (eds), *Applications of Statistics and Probability, ICASP-7*, Balkema, pp. 169–175.

Getis, A. and Boots, B. (1978). *Models of Spatial Processes*, Cambridge University Press, London, UK.

Ghali, A. and Favre, R. (1994). *Concrete Structures: Stresses and Deformations*, second edn, E & FN Spon.

Ghali, A. and Neville, A. (1989). *Structural Analysis: A Unified Classical and Matrix Approach*, Chapman and Hall, London, UK.

Ghanem, R. (1999). Stochastic finite elements with multiple random non-gaussian properties, *ASCE Journal of Engineering Mechanics* **125**: 26–40.

Gibson, L. J. and Ashby, M. F. (1988). *Cellular Solids: Structure & Properties*, Pergamon Press, Oxford, England.

Graham, L. L. and Baxter, S. C. (1999). Stochastic Field Representation of the Mechanical Properties of Composite Materials, *in* N. Jones and R. Ghanem (eds), *13th ASCE Engineering Mechanics Conference*, The Johns Hopkins University, Baltimore, MD, USA. CD-ROM.

Graham, L. L. and Deodatis, G. (1996). Variability response functions for plane elasticity problems with multiple stochastic material/geometric properties, *in* D. M. Frangopol and M. D. Grigoriu (eds), *Probabilistic Mechanics & Structural Reliability*, Worchester, MA, USA, pp. 174–177.

Graham, L. L. and Deodatis, G. (1998). Variability Response Functions for Stochastic Plate Bending Problems, *Structural Safety* **20**: 167–188.

Haritos, G. K., Hager, J. W., Amos, A. K., Salkind, M. J. and Wang, A. S. D. (1988). Mesomechanics: The Microstructure-Mechanics Connection, *International Journal of Solids and Structures* **24**: 1081–1096.

Hashin, Z. (1964). Theory of Mechanical Behavior of Heterogeneous Media, *Applied Mechanics Reviews* **17**: 1–9.

Hashin, Z. (1983). Analysis of Composite Materials, *ASME Journal of Applied Mechanics* **50**: 481–505.

Herrmann, H. and Roux, S. (eds) (1990). *Statistical Models for the Fracture of Disordered Media*, Elsevier, Amsterdam.

Hill, R. (1963). Elastic Properties of Reinforced Solids: Some Theoretical Principles, *Journal of the Mechanics of Physics and Solids* **11**: 357–372.

Hohenbichler, M. and Rackwitz, R. (1983). Reliability of Parallel Systems under Imposed Uniform Strain, *ASCE Journal of Engineering Mechanics* **109**: 896–907.

Hrennikoff, A. (1941). Solution of Problems of Elasticity by the Framework Method, *ASME Journal of Applied Mechanics* **8**: A169–A175.

Huyse, L. and Maes, M. A. (1999a). Random Field Modeling of Elastic Properties Using Homogenization, *ASCE Journal of Engineering Mechanics* . submitted for publication.

Huyse, L. and Maes, M. A. (1999b). Stochastic Finite Element Analysis Using Micro-Mechanically Based Stochastic Homogenization, *in* N. Jones and R. Ghanem (eds), *13th ASCE Engineering Mechanics Conference*, The Johns Hopkins University, Baltimore, MD, USA. CD-ROM.

Iwan, W. (1967). On a Class of Models for the Yielding Behaviour of Continuous and Composite Systems, *ASME Journal of Applied Mechanics* **34**: 612–617.

Jirásek, M. and Bažant, Z. P. (1994). Macroscopic Fracture Characteristics of Random Particle Systems, *International Journal of Fracture* **69**: 201–228.

Jirásek, M. and Bažant, Z. P. (1995). Particle Model for Quasibrittle Fracture and Application to Sea Ice, *ASCE Journal of Engineering Mechanics* **121**: 1016–1025.

Joe, B. (1991). GEOMPACK - A Software Package for the Generation of Meshes Using Geometric Algorithms, *Advances in Engineering Software and Workstations* **13**: 325–331.

Joe, B. and Simpson, R. B. (1986). Triangular Meshes for Regions of Complicated Shape, *International Journal for Numerical Methods in Engineering* **23**: 751–778.

Johnson, W. A. and Mehl, R. F. (1939). Reaction Kinetics in Processes of Nucleation and Growth, *Transactions of the American Institute of Mining, Metallurgical and Petroleum Engineers* **135**: 410–458.

Kandarpa, S., Kirkner, D. and Spencer, B. (1996). Stochastic Damage Model for Brittle Materials Subjected to Monotonic Loading, *ASCE Journal of Engineering Mechanics* **122**: 788–795.

Krajcinovic, D. (1979). Distributed Damage Theory of Beams in Pure Bending, *ASME Journal of Applied Mechanics* **46**: 592–596.

Krajcinovic, D. and Fanella, D. (1986). A Micromechanical Damage Model for Concrete, *Engineering Fracture Mechanics* **25**: 585–596.

Krajcinovic, D. and Mastilovic, S. (1995). Some Fundamental Issues of Damage Mechanics, *Mechanics of Materials* **21**: 217–230.

Krajcinovic, D. and Silva, M. (1982). Statistical Aspects of the Continuous Damage Theory, *International Journal of Solids and Structures* **18**: 551–562.

Kröner, E. (1980). Graded and Perfect Disorder in Random Media Elasticity, *ASCE Journal of the Engineering Mechanics Division* **106**(5): 889–914.

Lemaitre, J. and Chaboche, J.-L. (1985). *Mechanics of Solid Materials*, Cambridge University Press.

Li, C.-C. and Der Kiureghian, A. (1993). Optimal Discretization of Random Fields, *ASCE Journal of Engineering Mechanics* **119**(6): 1136–1154.

Liao, C. L. and Chang, C. S. (1992). A Microstructural Finite Element Model for Granular Solids, *Engineering Computations* **9**: 267–276.

Lin, S., Lutes, L. D. and Sarkani, S. (1997). Efficient simulation of multidimensional random fields, *ASCE Journal of Engineering Mechanics* **123**: 1082–1089.

Lin, Y.-K. (1976). *Probabilistic Theory of Structural Dynamics*, McGraw-Hill, New York, NY.

Liu, P.-L. and Der Kiureghian, A. (1991). Finite Element Reliability of Geometrically Nonlinear Uncertain Structures, *ASCE Journal of Engineering Mechanics* **117**(8): 1806–1825.

Loset, S. (1994a). Discrete Element Modelling of a Broken Ice Field - Part 1: Model Development, *Cold Regions Science and Technology* **22**: 339–347.

Loset, S. (1994b). Discrete Element Modelling of a Broken Ice Field - Part 2: Simulation of Ice Loads on a Boom, *Cold Regions Science and Technology* **22**: 349–360.

Maes, M. A. and Huyse, L. (1995). Tail Effects of Uncertainty Modeling in QRA, *Third International Symposium on Uncertainty Modeling and Analysis*, College Park, MD, USA, pp. 133–138.

Mahesh, S., Beyerlein, I. J. and Phoenix, S. L. (1999). Size Effects in the Fracture of 3D Fibrous Composites: Asymptotic Models Versus Simulations, *in* N. Jones and R. Ghanem (eds), *13th ASCE Engineering Mechanics Conference*, The Johns Hopkins University, Baltimore, MD, USA. CD-ROM.

Mahin, K., Hanson, K. and J.W. Morris, J. (1980). Comparative Analysis of the Cellular and Johnson-Mehl Microstructures Through Computer Simulation, *Acta Metallurgica* **28**: 443–453.

Martz, H. F. and Waller, R. A. (1982). *Bayesian Reliability Analysis*, John Wiley and Sons, New York, NY.

Mazars, J. (1986). A Description of Micro and Macro Damage of Concrete Structures, *Engineering Fracture Mechanics* **25**: 729–737.

Mirfendereski, D. and Der Kiureghian, A. (1994). Probabilistic Analysis of Micro-Fabricated Multicrystalline Beams, *in* G. I. Schuëller, M. Shinozuka and J. T. P. Yao (eds), *Proceedings of ICOSSAR '93 - The Sixth International Conference on Structural Safety and Reliability*, Balkema, Rotterdam, pp. 361–367.

Mirfendereski, D., Der Kiureghian, A., Ferrari, M. and Johnson, G. (1996). Probabilistic Characterization and Response Prediction of Micro-Electro-Mechanical Systems, *Technical report*, Department of Civil and Environmental Engineering. University of California at Berkeley.

Moukarzel, C. and Herrmann, H. J. (1992). A Vectorizable Random Lattice, *Preprint HLZR 1/92, HLZR-KFA*, Jülich, Germany.

Murakami, S. (1988). Mechanical Modeling of Material Damage, *ASME Journal of Applied Mechanics* **55**: 280–286.

Nemat-Nasser, S. and Hori, M. (1993). *Micromechanics: Overall Properties of Heterogeneous Materials*, North-Holland.

Okabe, A., Boots, B. and Sugihara, K. (1992). *Spatial Tesselations - Concepts and Applications of Voronoi Diagrams*, John Wiley & Sons.

Orisamolu, I. R. (1998). Stochastic Finite Element Method for the Probabilistic Residual Strength Assessment of Corroded Structures, *in* N. Shiraishi, M. Shinozuka and Y. K. Wen (eds), *Structural Safety and Reliability*, ICOSSAR '97, Balkema, Rotterdam, pp. 875–882.

Ostoja-Starzewski, M. (1989). Damage in Random Microstructure: Size Effects, Fractals, and Entropy Maximization, *Applied Mechanics Reviews* **42**: S202–S212.

Ostoja-Starzewski, M. (1993). Micromechanics as a Basis of Stochastic Finite Elements and Differences: An Overview, *Applied Mechanics Reviews* **46**: S136–

S147.

Ostoja-Starzewski, M. (1994a). Micromechanically Based Random Fields, *in* G. I. Schuëller, M. Shinozuka and J. T. P. Yao (eds), *Proceedings of ICOSSAR '93 - The Sixth International Conference on Structural Safety and Reliability*, Balkema, Rotterdam, pp. 629–635.

Ostoja-Starzewski, M. (1994b). Micromechanics as a Basis of Continuum Random Fields, *Applied Mechanics Reviews* **47**: S221–S230.

Ostoja-Starzewski, M. and Lee, J.-D. (1996). Damage Maps of Disordered Composites: A Spring Network Approach, *International Journal of Fracture* **75**: R51–R57.

Ostoja-Starzewski, M., Sheng, P. Y. and Jasiuk, I. (1994). Influence of Random Geometry on Effective Properties and Damage Formation in Composite Materials, *ASME Journal of Engineering Materials and Technology* **116**: 384–391.

Ostoja-Starzewski, M. and Wang, C. (1989). Linear Elasticity of Planar Delaunay Networks: Random Field Characterization of Effective Moduli, *Acta Mechanica* **80**: 61–80.

Ostoja-Starzewski, M. and Wang, C. (1990). Linear Elasticity of Planar Delaunay Networks. Part 2: Voigt and Reuss Bounds, and Modification for Centroids, *Acta Mechanica* **84**: 47–61.

Papoulis, A. (1991). *Probability, Random Variables, and Stochastic Processes*, McGraw-Hill Series in Electrical Engineering, third edn, McGraw-Hill, New

York, NY.

Petrenko, V. F. (1993). Structure of Ordinary Ice I_h. Part 1: Ideal Structure of Ice, *Technical report*, Cold Regions Research & Engineering Laboratory.

Petrenko, V. F. and Whitworth, R. W. (1994a). Structure of Ordinary Ice I_h. Part 2: Defects in Ice. Volume 1: Point Defects, *Technical report*, Cold Regions Research & Engineering Laboratory.

Petrenko, V. F. and Whitworth, R. W. (1994b). Structure of Ordinary Ice I_h. Part 2: Defects in Ice. Volume 2: Dislocations and Plane Defects, *Technical report*, Cold Regions Research & Engineering Laboratory.

Phoenix, S. and Smith, R. (1983). A Comparison of Probabilistic Techniques for the Strength of Fibrous Materials Under Local Load-Sharing Among Fibers, *International Journal of Solids and Structures* **19**: 479–496.

Pijaudier-Cabot, G. and Bažant, Z. P. (1987). Nonlocal Damage Theory, *ASME Journal of Applied Mechanics* **113**: 1512–1513.

Rossi, P. and Richer, S. (1987). Numerical Modelling of Concrete Cracking Based on a Stochastic Approach, *Matériaux et Constructions/Materials and Structures* **20**: 334–337.

Rossi, P., Ulm, F.-J. and Hachi, F. (1996). Compressive Behavior of Concrete: Physical Mechanisms and Modeling, *ASCE Journal of Engineering Mechanics* **122**: 1038–1043.

Rothenburg, L. and Bathurst, R. J. (1992). Micromechanical Features of Granular Assemblies with Planar Elliptical Particles, *Géotechnique* **42**: 79–95.

Russ, J. C. (1995). *The image processing handbook*, CRC Press, Boca Raton, FL, USA.

Sab, K. (1992). On the Homogenization and the Simulation of Random Materials, *European Journal of Mechanics: A - Solids* **11**: 585–607.

Schlangen, E. (1993). Experimental and Numerical Analysis of Fracture Processes in Concrete, *Heron* **38**(2).

Schlangen, E. and Van Mier, J. (1992). Simple Lattice Model for Numerical Simulation of Fracture of Concrete Materials and Structures, *Matériaux et Constructions/Materials and Structures* **25**: 534–542.

Schuëller, G. I. (1997). A State-of-the-Art Report on Computational Stochastic Mechanics, *Probabilistic Engineering Mechanics* pp. 197–321.

Shinozuka, M. and Deodatis, G. (1991). Simulation of Stochastic Processes by Spectral Representation, *Applied Mechanics Revieus* **44**: 191–203.

Shinozuka, M. and Deodatis, G. (1996). Simulation of Multi-Dimensional Gaussian Stochastic Fields by Spectral Representation, *Applied Mechanics Revieus* **49**: 29–53.

Shinozuka, M. and Jan, C.-M. (1972). Digital Simulation of Random Processes and Its Applications, *Journal of Sound and Vibration* **25**: 111–128.

Shinozuka, M. and Yamazaki, F. (1988). Stochastic finite element analysis: an introduction, *in* S. T. Ariaratnam, G. I. Schuëller and I. Elishakoff (eds), *Stochastic Structural Dynamics. Progress in Theory and Applications*, Elsevier, London, UK, pp. 241–291.

Sinha, N. K. (1991). Microstructure and Mechanical Behaviour of Ice, *in* D. S. Sodhi (ed.), *Cold Regions Engineering. Proceedings of the Sixth International Specialty Conference*, pp. 519–530.

Smalley, I. J. (1966). Contraction Crack Networks in Basalt Flows, *Geological Magazine* **103**: 110–114.

Smith, R. L. and Phoenix, S. L. (1981). Asymptotic Distributions for the Failure of Fibrous Materials Under Series-Parallel Structure and Equal Load Sharing, *ASME Journal of Applied Mechanics* **48**.

Ting, J. M., Corkum, B. T., Kauffman, C. L. and Greco, C. (1988). Discrete Numerical Model for Soil Mechanics, *ASCE Journal of Geotechnical Engineering* **115**: 379–398.

van Baars, S. (1996). Discrete Element Modelling of Granular Materials, *Heron* **41**: 139–157.

Van Mier, J. G. M., Schlangen, E. and Vervuurt, A. (1996). Tensile Cracking in Concrete and Sandstone: Part 2 - Effect of Boundary Rotations, *Matériaux et Constructions/Materials and Structures* **29**: 87–96.

Vanmarcke, E. (1983). *Random Fields: Analysis and Synthesis*, The MIT Press, Cambridge, MA.

Vanmarcke, E. (1994). Stochastic Finite Elements and Experimental Measurements, *Probabilistic Engineering Mechanics* **9**: 103–114.

Vanmarcke, E. and Grigoriu, M. (1983). Stochastic Finite Element Analysis of Simple Beams, *ASCE Journal of Engineering Mechanics* **109**: 1203–1214.

Vervuurt, A., Schlangen, E. and Van Mier, J. G. M. (1996). Tensile Cracking in Concrete and Sandstone: Part 1 - Basic Instruments, *Matériaux et Constructions/Materials and Structures* **29**: 9–18.

Wall, F. J. and Deodatis, G. (1994). Variability Response Functions of Stochastic Plane Stress/Strain Problems, *ASCE Journal of Engineering Mechanics* **120**: 1963–1982.

Walraven, J. C. (1980). *Aggregate Interlock: A Theoretical And Experimental Analysis*, Delft University Press.

Yamazaki, F. and Shinozuka, M. (1988). Digital generation of non-Gaussian stochastic fields, *ASCE Journal of Engineering Mechanics* **114**(7): 1183–1197.

Yamazaki, F. and Shinozuka, M. (1990). Simulation of Stochastic Fields by Statistical Preconditioning, *ASCE Journal of Engineering Mechanics* **116**(2): 268–287.

Yip, W.-K. (1996). New Damage Variable in Failure Analysis of Concrete, *ASCE Journal of Materials in Civil Engineering* **8**: 184–188.

Zhang, J. and Ellingwood, B. (1994). Orthogonal Series Expansion of Random Fields in Reliability Analysis, *ASCE Journal of Engineering Mechanics* **120**(12): 2660–2676.

Zhang, J. and Ellingwood, B. (1995). Effects of Uncertain Material Properties on Structural Stability, *ASCE Journal of Structural Engineering* **121**(4): 705–716.

Zhang, J. and Ellingwood, B. (1996). SFEM for Reliability of Structures with Material Nonlinearities, *ASCE Journal of Structural Engineering* **122**: 701–704.

Zhang, Y. (1994). *Finite Element Reliability Methods for Inelastic Structures*, PhD thesis, University of California at Berkeley.

Zubelewicz, A. and Bažant, Z. P. (1987). Interface Element Modeling of Fracture in Aggregate Composites, *ASCE Journal of Engineering Mechanics* **113**: 1619–1630.